Coating and Surface Treatment for Novel Biomedical Implants and their Corrosion Resistance

Doctoral Thesis

(Dissertation)

To be awarded the degree

Doctor of Engineering (Dr.-Ing.)

Submitted by

Aymen Abduljabbar Ahmed

From Iraq/ Nineveh

Approved by the Faculty of Natural and Materials Science

Clausthal University of Technology

Date of oral examination

31. March 2017

Dean

Prof. Dr. rer. nat. Winfried Daum

Chairperson of the Board of Examiners

Prof. Dr. rer. nat. Albrecht Wolter

Chief Reviewer

Prof. Dr.-Ing. habil. Lothar Wagner

Reviewer

Prof. Dr.-Ing. Claudia Fleck

Acknowledgement

First of All, praises to allah who has given blessing, strength and knowledge in finishing this thesis.

I am deeply grateful to Prof. Lothar Wagner for his supervision, continuous support and valuable discussions. I am greatly indebted to him for giving me the opportunity to perform my Ph.D. under his supervision in his group. I am so thankful to the examiner Prof. Claudia Fleck for her contribution in given suggestions and advices during the work.

The gratitude is also addressed to all the members in our research group. Especially I would like to thank Dr. Manfred Wollmann and Dr. Mansour Mhaede for thier kind support and guidance during the work. I would like also to thank all the technical staffs at IWW for their selfless support and warmhearted help during performance of the practical work, particularly, Mr. Jörg Schumann who is in charge of the metallography laboratory, Mr. Gerd Neuse for his patient guidance on the operation of testing equipments and Mr. Peter König for performing SEM.

I am grateful to MoHESR (Ministry of Higher Education and Scientific Research - Iraq) for sponsoring me to achieve a PhD. degree at IWW, TU Clausthal.

Finally, I would like to express my deepest gratitude and appreciation to my parents, although they are no more alive, but their living spirits usually provide me the strength, support and love so I hope that they are satisfied and proud of me where they are and I ask Allah to bless them and shower them with mercy.

Abstract

Metallic biomaterials continue to be used extensively for the fabrication of surgical implants due to their excellent mechanical, physical and biological properties. This work aims to improve the performance of the materials that used as biomedical implants. Enhancement the mechanical properties, corrosion resistance, and biocompatibility, are the main factors that help to success the implant materials in the aggressive environment for a long time. Two types of stainless steel (AISI 316L and AISI 316Ti) and Ti-6AL-4V alloys were used as biomaterials in this study. The surface modification and bulk plastic deformation are the main techniques to maintain a relatively good mechanical properties and biocompatibility within this study. Bulk deformation was processed through rotary swaging (RS) and cold rolling while surface deformation was induced through shot peening (SP) at different parameters. Different heat treatments were done on the swaged bar Ti-6Al-4V to get on duplex and globular microstructure. The correlation between these microstructures and corrosion behavior was studied.

SP was carried out using three sizes of ceramic shots (125– 250, 450 and 850 μm), two Almen intensities (0.22 and 0.28 mmA) and two coverage degrees (100 and 200%). Moreover, hydroxyapatite coating (HA) was applied on the deformed material to improve their corrosion resistance. HA coating was sintering at 500, 600 and 700^{o}C to improvement the adhesive properties.

The properties of HA coating were studied by X-ray diffraction (XRD), energy-dispersive X-ray spectroscopy (EDX), scanning electron microscopy (SEM) and standard tensile adhesion test. The phase transformation of the stainless steel due to bulk and surface plastic deformation were recorded by X-ray diffraction spectra. The effect of these treatments namely, cold rolling, rotary swaging and shot peening on the surface roughness, microhardness, induced residual stresses, wettability, corrosion and corrosion fatigue were investigated. The corrosion behavior was studied using potentiodynamic polarization and electrochemical impedance spectroscopy. Ringer`s solution was used as an electrolyte for the corrosion and corrosion fatigue tests at 37°C.

The bulk plastic deformation regarding cold rolling and rotary swaging enhanced the mechanical properties. The results showed marked improvement of the fatigue life, of rotary swaged 316L AISI materials, tested in air and Ringer solution. However, the electrochemical behavior after these treatments are not the same for the deformed materials (AISI 316Ti, AISI 316L, and Ti-6Al-4V). Appearing the martensitic phase after cold rolling led to a lower corrosion resistance of AISI 316Ti while the electrochemical tests showed slightly increase the corrosion resistance of the AISI 316L and Ti-6Al-4V after rotary swaging compared with the as received materials.

On the shot peening, the results showed an increased surface microhardness and induced compressive stresses by increasing the coverage degree and the Almen intensity. The rougher surface after SP improved the wettability in terms of reduced contact angle. Increasing the shot size led to a lower surface roughness and an improved corrosion resistance. However, SP reduces the corrosion resistance compared with the untreated materials. The applied HA coating on the shot-peened surfaces led to a further improvement of the wettability. Applying of HA coating led not only to marked corrosion resistance but also to further improvement of the corrosion fatigue life. The sintering of HA coating refers to a good enhancement of the crystallization of the HA coating sintered at 700^{o}C. The adhesive strength of as-coated (AC) material increased from 8.3 MPa to 12.2, 16.8 and 19.8 MPa after sintering at 500, 600 and 700^{o}C, respectively. The corrosion rate of the as-coated material reduced sharply from 0.405 to 0.094 µA.cm^{-2} after sintering at 700^{o}C.

The potentiodynamic polarization and electro-impedance spectroscopy techniques showed that the microstructure has significantly affected the corrosion behavior of Ti-6AL-4V alloy. The results proved that the globular microstructure shows high corrosion rate compared to duplex and nanostructured materials.

Zusammenfassung

Die metallische Biomaterialien werden weiterhin aufgrund ihrer hervorragenden mechanischen, physikalischen und biologischen Eigenschaften hauptsächlich für die Herstellung von chirurgischen Implantaten verwendet. Diese Arbeit zielt auf die Verbesserung der Leistung der Materialien, die als biomedizinische Implantate verwendet werden. Verbesserung der mechanischen Eigenschaften, Korrosionsbeständigkeit und Biokompatibilität sind die Hauptfaktoren, die zum Erfolg der Implantatmaterialien im aggressiven Umfeld für eine lange Zeit beitragen. Diese Studie befasst sich mit zwei Arten von rostfreiem Stahl (AISI 316L und AISI 316ti) und Ti-6AL-4V-Legierungen als Biomaterialien. Die Oberflächenmodifikation und die plastische Verformung sind die Haupttechniken in dieser Studie, um relativ gute mechanische Eigenschaften und Biokompatibilität beizubehalten. Die Bulk-Verformung wurde durch Rundknettechnik (RS) und Kaltwalzen verarbeitet, während die Oberflächenverformung durch Kugelstrahlen (SP) bei verschiedenen Parametern induziert wurde. Verschiedene Wärmebehandlungen wurden auf dem verpressten Stab Ti-6Al-4V durchgeführt, um auf Duplex- und kugelförmige Mikrostruktur zu erhalten. Die Korrelation zwischen diesen Mikrostrukturen und dem Korrosionsverhalten wurde untersucht. Das Kugelstrahlen wurde unter Verwendung von drei Größen von Keramiksch (125- 250, 450 und 850 μm), zwei Almen-Intensitäten (0,22 und 0,28 mmA) und zwei Bedeckungsgraden (100 und 200 %) durchgeführt. Darüber hinaus wurde eine Hydroxylapatitbeschichtung (HA) auf das verformte Material aufgebracht, um ihre Korrosionsbeständigkeit zu verbessern. Die HA- Beschichtung sinterte bei 500, 600 und 700 ºC, um die hafteigenschaften zu verbessern. Die Eigenschaften der HA-Beschichtung wurden durch Röntgendiffraktion (XRD), energiedispersive Röntgenspektroskopie (EDX), Rasterelektronenmikroskopie (SEM) und Standardzugfestigkeitstest untersucht. Die Phasentransformation des rostfreien Stahls aufgrund der Volumen- und plastische oberflächenverformung wurde durch Röntgenbeugungsspektren aufgezeichnet. Die Wirkung dieser Behandlungen, nämlich Kaltwalzen, Rotationsverpressen und Kugelstrahlen auf die Oberflächenrauhigkeit, Mikrohärte, induzierte Restspannungen, Benetzbarkeit, Korrosion und Korrosionsermüdung wurden untersucht. Das Korrosionsverhalten wurde mittels potentiodynamischer Polarisation und elektrochemischer Impedanzspektroskopie untersucht. Die Ringer-Lösung wurde als Elektrolyt für die Korrosions- und Korrosionsermüdungstests bei 37 °C verwendet. Die Bulk plastische Verformung hinsichtlich Kaltwalzen und Rundknettechnik verbesserte die mechanischen Eigenschaften. Die Ergebnisse zeigten eine deutliche Verbesserung der Ermüdungslebensdauer von rotationsgesenkten 316L-AISI-Materialien, die in Luft und Ringer-Lösungen getestet wurden. Jedoch ist das elektrochemische Verhalten nach diesen Behandlungen für die deformierten Materialien (AISI 316Ti, AISI 316L und Ti-6Al-4V) nicht dasselbe. Das Auftreten der martensitischen Phase nach dem Kaltwalzen führte zu einer niedrigeren Korrosionsbeständigkeit von AISI 316Ti, während die elektrochemischen Tests die Korrosionsbeständigkeit der AISI 316L und Ti-6Al-4V nach dem Rundkneten im Vergleich zu den erhaltenen Materialien leicht erhöhten. Bei der Kugelstrahlung zeigten die Ergebnisse eine erhöhte Oberflächen-Mikrohärte und induzierte Druckspannungen, indem der Bedeckungsgraden und die Almen-Intensität erhöht wurden. Die rauhe Oberfläche nach SP verbesserte die Benetzbarkeit im Hinblick auf einen verringerten Kontaktwinkel. Die Erhöhung der Schrotgröße führte zu einer geringeren Oberflächenrauhigkeit und einer verbesserten Korrosionsbeständigkeit. SP reduziert jedoch die Korrosionsbeständigkeit gegenüber den unbehandelten Materialien. Die aufgebrachte HA-Beschichtung auf den kugelgestrahlten Oberflächen führte zu einer weiteren Verbesserung der Benetzbarkeit. Das Aufbringen von HA- Beschichtung führte nicht nur zur Verbesserung der Korrosionsbeständigkeit, sondern auch zur weiteren Verbesserung der Korrosionsermüdungslebensdauer. Die Korrosionsrate des beschichteten Materials reduzierte sich nach dem Sintern bei 700 ºC deutlich von 0,405 auf 0,094 $\mu A.cm^{-2}$. Die potentiodynamischen Polarisations- und Elektroimpedanzspektroskopietechniken zeigten, dass die Mikrostruktur das Korrosionsverhalten der Ti-6AL-4V-Legierung signifikant beeinflusst hat. Die Ergebnisse zeigten, dass die kugelförmige Mikrostruktur im Vergleich zu Duplex- und Nanostrukturen eine hohe Korrosionsrate aufweist.

Table of Contents

1. Introduction 1

1.1 Overview 1

1.2 Select materials for implants 1

1.3 Detrimental factors affecting the performance of implant materials ………….. 3

2. Theoretical background ………………………………………………………. 7

2.1. Metallic Biomaterials 7

2.2. 316Ti and 316L stainless steel alloys …………………………….…………... 7

2.3. Ti-6Al-4V alloys 13

2.4. Surface treatment and modification 18

2.4.1. Shot peening 18

2.4.2. Hydroxyapatite coating 21

2.5. Sever plastic deformation (SPD) 22

2.6. Wettability Characteristics 24

2.7. Motivation 24

2.8. Aims of study 24

3. Experimental Work 27

3.1 Materials and processing 27

3.2 Shot peening ………………………………………………….....………… 29

3.3 Hydroxyapatite coating ……………………………………………..……… 30

3.3.1 The mechanism of coating formation …………………………………… 31

3.3.2 Coating sintering and adhesive test ……………………………………… 32

3.3.3 Coating analysis …………………………………………………………… 32

3.4 Surface layer properties ……………………………………………………….. 33

3.4.1 Microhardness …..……………………………………………………… 33

3.4.2 Residual stress …………………………………………………………… 33

3.4.3 Roughness ……………………………………………………………….. 34

3.4.4 Wettability of surface …………………………………………………… 34

3.5 Microstructure analysis ……………………………………………………….. 35

3.5.1 Optical microscopy ……………………………………………………… 35

3.5.2 Scanning electron microscopy (SEM) …………………………………... 35

3.5.3 Phases analysis …………………………………………………………... 36

3.6 Mechanical properties examination …………………………………………... 36

3.6.1 Tensile test ………………………………………………………...….. 36
3.6.2 Fatigue testing ……………………………………………...……. 37
3.6.3 Corrosion fatigue testing ……………………………………...……. 38
3.7 Electrochemical tests ……………………………………………..……... 39
4. Chapter four: 316Ti and 316L Stainless Steel ………………………………….. 42
4.1 Materials characterization 316Ti SS …………………………………………….. 42
4.2 Materials characterization 316L SS …………………..………………………… 43
4.3 Shot peening …………………………………………………………….………….. 47
4.3.1 Mechanical properties ………………………………………………………… 47
4.3.2 Surface structures and roughness ……..…………………………………… 49
4.4 Coating characterization ………………………………………………………… 52
4.4.1 Coating/substrate adhesion strength ……………………..………………… 59
4.4.2 Corrosion behavior ……………………………………………………………… 60
4.5 Wettability …………………………………………………………………………….. 62
4.6 Corrosion behavior of deformed 316Ti SS ……………………..……...…….. 64
4.7 Corrosion behavior of 316L SS …………………………………...……….. 68
4.7.1 Rotary swaging samples ………..…………………………………….. 68
4.7.2 Shot peened samples ………………...…………………………….….. 70
4.8 Corrosion fatigue of SS 316L …………………………………………………… 75
5. Chapter five: Ti-6Al-4V……………..…………………………………….…….. 79
5.1 Metallographic features ….…………..………………………………….……… 79
5.2 Mechanical properties ………………..……………………………….……… 79
5.3 Surface topography and roughness ……………………………….…….. 83
5.4 Corrosion behavior ……………………………………………….……….... 86
6. Chapter 6: Conclusions …………….……………………………………………… 91
6.1 Stainless steel 316Ti ………………………………………………………… 91
6.2 Stainless steel 316L ……………………………..…………………….... 91
6.2.1 Rotary swaging and shot peening ……………..……………………… 91
6.2.2 Sintering of HA- coating ………………..……………………………….. 92
6.3 Ti-6Al-4V ……………………………………………………………………… 93
References 95
CV and publications ……..……………………...…………………….…… 115

Chapter one

Introduction

1.1 Overview

Biomaterials are materials used for making devices that can interact with biological systems to coexist for longer service with minimal failure. Williams [1] defined biomaterials as "nonviable materials used in medical devices, intended to interact with the biological systems". Biomaterials are widely used in repair, replacement, or augmentation of diseased or damaged parts of the musculoskeletal system such as bones, joints and teeth. The fundamental requirement of a biomaterial is that the material and the tissue environment of the body should coexist without having any undesirable or inappropriate effect on each other. Biocompatibility, an essential requirement for any biomaterial, implies the ability of the material to perform effectively with an appropriate host response for the desired application. Common medical devices made of biomaterials include hip replacements, prosthetic heart valves and the less common neurological prostheses and implanted drug delivery systems. These devices when placed inside the body are termed implants when they are intended to remain there for a substantial period of time, and as prosthesis when they are permanently fixed in the body for long-term application till the end of lifetime [2].

Orthopedic implant devices are generally mounted on to the skeletal system of the human body for aiding healing, correcting deformities and restoring the lost functions of the original part. These are supporting bone plates, screws, total hip joints, knee joints, elbow joints, shoulder joints and reattachments for tendons or ligaments. The implants are exposed to the biochemical and dynamic environment of the human body and their design is dictated by anatomy and restricted by physiological conditions. In the past few decades, increase in the utilization of self-operating machines, participation of many persons in sports, defense activities, increased interest in motorcycles and bicycles, and day-to-day increasing traffic, has resulted in enormous increase in the number of accidents. This has necessarily led people to opt for orthopedic implants for early and speedy recovery and resumption of their routine activities.

1.2 Select materials for implants

Metallic materials are widely used in medical applications as implants to restore lost functions or replace organ functioning below acceptable levels [3]. Implantation applications have been markedly increased; every year over 270,000 hip replacements are performed in the United States [4]. Moreover, by 2030, the demand for primary total hip arthroplasties is estimated to grow by 174% to 572,000. The demand for hip revision procedures is projected to marked growth in the next decades [4,5]. Surgical implants such as hip and knee joint implants usually fail within a period of about 10–15 years of use, which leads to revision surgery in order to recover the functionality of the system [6]. The reasons for their failure include degradation, design and surgical issues [7]. The commonly applied metallic biomaterials for orthopedic applications in clinical practice are stainless steels, cobalt–chromium and titanium-based alloys [8,9]. These materials are more suitable for loadbearing applications compared with ceramics or polymeric materials, mainly due to their combined high mechanical strength and fracture toughness [10]. The necessity of cost reduction in public health services makes stainless steel as the most economical option of metals used in orthopedic surgery [11,12]. It is widely applied for temporary implantation, although it is also used as permanent implants in developing countries [13]. Stainless steel is used both in artificial knee and hip joints, bone plate or screw [14, 15].

However, the stainless steel has high Young modulus, which makes it using in some components of implants is limited. The hip prosthesis is complex and consists of a femoral head and stem. The Young’s modulus of the prosthesis material is a critical design variable because, for a given stem geometry design, it largely determines how the load is transferred, via the cement, to the bone. The femoral stem component replaces a large portion of bone in the femur, and this is therefore the load-bearing part of the implant. To bear this load, it must have a Young’s modulus comparable to that of cortical bone. If the implant is not as stiff as bone, then the remaining bone surrounding the implant will be put under increased stress. If it is stiffer than bone, then a phenomenon known as stress shielding will occur [16]. Stainless steel has a Young’s modulus much higher than that of bone, meaning that stress shielding is a serious issue. Stainless steel was used for the femoral component in the earliest hip replacements, and is still used in some implants today [17, 18]. Titanium’s modulus is only half that of stainless steel, so the remaining bone will suffer less from stress shielding. It has an excellent strength to weight ratio and an impressive resistance to corrosion. Ti-6AI-4V alloy has high strength and resistance to wear and fatigue, and these advantages over stainless steel make it a very good choice of material for the femoral stem component [19]. The most commonly used titanium alloy is the two-phase (α + β) Ti-6Al-4V, due to the α/β transformation in the alloy. A variety of microstructures and property combinations can be achieved through thermo-mechanical processing, which develops new stronger materials and permits the adaptation of properties to specific applications [20].

1.3 Detrimental factors affecting the performance of implant materials

Numerous studies have reported on the problems of fatigue fracture and wear of the femoral head surface [24-26], mechanical strength [23-27] and the stability of the stem of a hip prosthesis [28]. Figure 1.1 illustrates some examples of the fatigue fracture of implant devices such as hip prosthesis and mechanical heart valve.

The surface sub-structure of biomaterials is a key factor to understand the mechanisms of fatigue failure [26]. Figure 1.2 shows a schematic cross-section of a deformed metallic biomaterial surrounded by a physiological environment. Teoh [26] documented that the sub-structure is composed of three distinct layers: molecular absorbed layer, passive oxide film and deformed layer. Cyclic loading leads to the generation of wear debris (contact body).

Fig. 1.1, some examples of fatigue failure of medical devices [26]: (a) hip prosthesis; and (b) explanted disc mechanical heart valve.

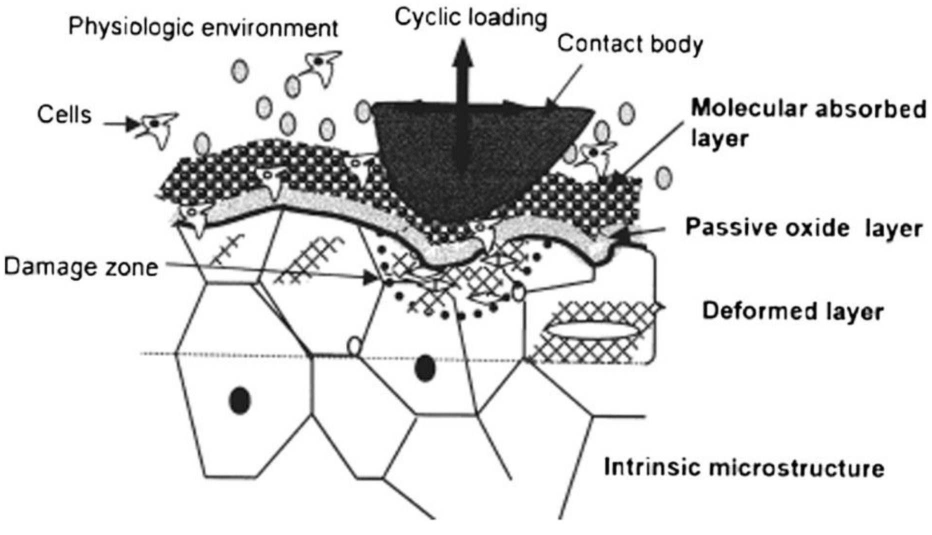

Figure 1.2, schematic representation of the substructure of a metallic biomaterial [26].

The molecular absorbed layer consists of growing tissue (cells) in contact with the physiological environment and the passive layer on the surface of the metallic implant. The combined influence of corrosion and cyclic loading is known to affect the mechanical properties of metallic alloys. The cracks frequently initiate from corrosion-induced surface defects. Crack initiation mechanisms include competition between pit growth and short crack growth, preferential dissolution of plastically deformed material [21], local rupture of the passive film by persistent slip bands (PSB) [22] and hydrogen embrittlement in the cathodic domain and deformation/corrosion synergy effects [29–31]. Crack initiation accelerates the failure of the implant by fatigue. Among the various types of fractures, fatigue fracture is identified as a crucial problem associated with implant loosening. Fatigue characteristics are closely related with the microstructures. The microstructures in metallic structural biomaterials change according to the employed processing method. Generally, mechanical strength is related to the ability of metals to deform plastically. Plastic deformation processes belong to the top down approach and are capable of leading to substantial grain refinement so that the grains can be reduced to the sub-micrometer or even the nanometer range. Ultra-fine grains metals and alloys are expected to have high strength as a result of structural refinement, according to the Hall–Petch relationship, where the yield stress varies with the reciprocal of the square root of the grain size. On the other hand, ultrafine grain materials have limited ductility due to susceptibility to deformation localization. The grain refinement can produce through equal channel angular pressing (ECAP) [32] or rotary swaging (RS) which is a hammer forging process for the reduction of cross-section of solids, tubes and wires. Some of the advantages of rotary swaging include short cycle times, good surface finishes and tight size tolerances [33]. This grain refinement can lead to drastic increases in yield stress, tensile strength and high cycle fatigue (HCF) strength.

In addition to the strength, the stem of a hip prosthesis must be stable after being implanted. The stem must integrate with the surrounding host tissue without loosening to support its load bearing function [28]. Shot peening (SP) is widely applied as a surface treatment to improve the integration quality of biomaterials with the host tissue [34–38]. In principle, the treatment is implemented to generate a rough surface to which specific proteins can adhere well and subsequently initiate bone tissue development on the implant surface [39, 40]. It was reported that the surface topography and roughness influence the initial cell response at the cell-material interface, ultimately affecting the rate and quality of new tissue formation [40]. Moreover, it is well known that shot peening (SP) is able to increase the fatigue strength and endurance of metallic components [41]. The positive effect of shot peening on the fatigue properties is generally related to its ability to introduce a compressive residual stress in the surface layer of the material and to the surface work hardening caused by the not uniform plastic deformation caused by the multiple impacts of the shot flow [42].

However, shot SP produces a rough surface resulting from the high energy of colliding shots that cause an indentation on the surface. It creates a roughness profile that is linearly proportional to the velocity/intensity of the shot. The rougher SP-surface induces a bigger interaction area and subsequently leads to increase of the corrosion rate [43-45]. This interaction can lead to; (a) the failure of the implant to function as it was intended, or (b) have an adverse effect on the patient resulting in the rejection of the implant by the surrounding tissue, or both [46]. The biomaterials like stainless steel 316 L are self-protected by the spontaneous formation of a thin oxide film. The passive layer formed on surgical stainless steel and Co-based alloys are strongly enriched in Cr_2O_3 oxide [47-51]. Although the thickness of these passive films is typically only a few nanometers, but they act as a highly protective barrier between the metal surface and the aggressive biological environment. Consequently, the passive film kinetically retards the rate of dissolution significantly. The protectiveness of the passive film is determined by the rate of ion transfer of the film. The transport of ion through the film is affected by the film's chemical composition, structure, thickness and presence of defects. Localized corrosion typically starts at sites characterized as inhomogeneity either in the material or in the surrounding environment. Pitting corrosion usually follows the general attack of corrosion on the surfaces and sometimes evolves into exfoliation corrosion. It is well known that pitting corrosion has a strong effect on fatigue life of alloys. Fatigue cracks usually initiate from the corrosion pit sites [52, 53]. Under the interaction of cyclic load and the corrosive environment, corrosion pits act as geometrical discontinuities, leading to crack initiation and cyclic loading facilitates the crack propagation that leads to the final failure [54]. The rough surface induced by SP becomes more susceptible to the pitting corrosion [44], which subsequently result in the destruction of a passive region of the sample surface [45]. The best combination of both a high strength and a minimum corrosion rates should be through the optimization of SP parameters like size of media, surface coverage and Almen intensity. The controlled SP parameters help in enhancing the surface and mechanical properties of the material. T. Dorr et al. **[**55] and M. Obata et al. **[**56**]** discussed the increase in surface hardness and surface roughness with increase shot size and the peening intensity respectively. According to the guidelines given by Champaine [57], the exposure time is an important factor to achieve desired peening coverage for the material. Sharma and Mubeen [58] examined the effect of shot size on peening intensity. They guided the selection of the correct size of shot to obtain desired intensity of SP. In another study, Suyitno et al. [59] found that the surface blasting treatment by using big steel ball-diameter led to a reduction in the current density as well as increasing the surface microhardness.

Many studies refer that the blasting and SP increase the wettability of the materials surface [60-62]. The high surface roughness induced by SP or blasting decreases the droplet contact angle of water with the surface. A contact angle less than 90° (low contact angle) usually indicates that wetting of the surface is very favorable, and the fluid will spread over a large area of the surface. Contact angles greater than 90° (high contact angle) generally means that wetting of the surface is unfavorable, so the fluid will minimize contact with the surface and form a compact liquid droplet [63]. Wettability of the substrate is known to influence protein adsorption. It is usually reported that biomaterial surface with moderate hydrophilicity improved cell growth and higher biocompatibility [64].

Coating the surface with HA is an effective technique that be used to enhance the surface wettability of materials [65]. Wetting properties are affected by surface characteristics, such as surface topography and chemistry [66]. It has been reported that surface wettability was significantly higher in the HA-coated titanium samples compared to the non-coated titanium samples; this contrast is directly related to the difference in the surface chemistry of non-coated and HA-coated samples [67]. HA coatings are also widely employed to enhance the osseointegration of orthopedic and dental implants [68], and used to improve corrosion resistance by forming a barrier against the penetration of metal ions from the substrate [69, 70].

Chapter two

Theoretical background

2.1. Metallic Biomaterials

Orthopedic implants have improved the quality of life for millions of people over the last quarter of a century. The engineering objective is to provide minimal physiological stress to the remaining bone system so that the integrity and functionality of the bone and prosthetic materials are maintained over a long service life. Thus, materials suitable for implantation are those that are well-tolerated by the body and can withstand cyclic loading in the aggressive environment of the body. Metallic implants all share these properties making them the most used material type for joint replacements [71]. Metals also provide high X-ray imaging visibility which is crucial during inspection. Tribological properties like wear and corrosion resistance also play a crucial part in joint replacement. The major drawback in metallic implants is that electrochemical reactions take place on metallic surfaces in the human body. Metals are known to corrode in contact with body fluid environments. Most cells cannot metabolize the corroded particles therefore giving rise to harmful infection to the body. Improved tribological properties reduce toxic ions from being released in vivo. Contamination of ions released from joint replacements is still a major issue that needs to be resolved for metallic biomaterials.

The most important groups of alloys that have been used for femoral components are austenitic stainless steels, cobalt-chrome alloys and titanium alloys [71]. Co based alloys were not studied in this work. One problem that has occurred with Co based alloys is their release of toxic ions which recently instigated a recall of the hip replacements [72].

2.2. 316Ti and 316L stainless steel alloys

AISI 316Ti stainless is a titanium-stabilized version of Type 316 molybdenum-bearing austenitic stainless steel. The Type 316 alloys offer excellent resistance to general corrosion and pitting/crevice corrosion, which is better than the conventional chromium-nickel austenitic stainless steels such as Type 304. They also offer higher creep, stress-rupture and tensile strength at elevated temperature. Type 316 stainless steel can be susceptible to sensitization – the formation of grain boundary chromium carbides at temperatures between approximately 900 and 1500 °F (425 to 815 °C) – which can result in rapid corrosion. Resistance to sensitization is achieved in Type 316Ti with titanium additions to stabilize the structure against chromium carbide precipitation, which is the source of sensitization. This stabilization is achieved by an intermediate-temperature heat treatment, during which the titanium reacts with carbon to form titanium carbides. This significantly reduces susceptibility to sensitization in service by limiting the formation of chromium carbides. Thus, the alloy can be used for extended periods at elevated temperatures without compromising its corrosion resistance.

Stainless steel 316 was further improved by reducing the carbon content to a maximum of 0.03 % from 0.08 % to reduce the risk of intergranular corrosion attacks [71]. This became known as 316L stainless steel, where the "L" stands for low carbon content. Additional molybdenum also enhances corrosion pitting in vivo. 316L stainless steel has become the most popular stainless steel used for biomedical implants due to its improved corrosion resistance properties. Nickel content in 316L is set at maximum of 17 to 20%. This composition is suitable for stabilizing the austenitic phase at room temperature and also enhance the corrosion resistance. However, large ratios of Ni: Cr concentrations were also found to impose allergic infections to the host body [73]. The minimum amount required for maintaining the austenitic phase is 10% Ni. Small amounts of silicon are present in the steel composition. Silicon increases the hardness of ferrite, oxidation resistance and is an effective deoxidizer. Even with the detailed compositions, it should be noted that 316L steel may corrode under certain circumstances in a highly stressed and oxygen depleted region. It is therefore crucial to modify the surface of the metal to improve the wear resistance, corrosion resistance and fatigue strength of 316L steel [71].

Phase diagram: The mechanical properties of 316 stainless steel depend on its microstructures and thermal history. Phase diagrams are significant in understanding the melting and crystallization of the alloy. Phases in an alloy can be expressed as homogeneous portions that have uniform physical and chemical characteristics [74]. In the case of 316 a binary alloy (Iron-Carbon) phase diagram is used to describe the characteristic phase transformations. Figure 2.1 show the iron rich portion of the Fe-C phase diagram. Only 0.02-0.03 % C is present in 316 stainless steel therefore only the region along the left vertical axis is considered.

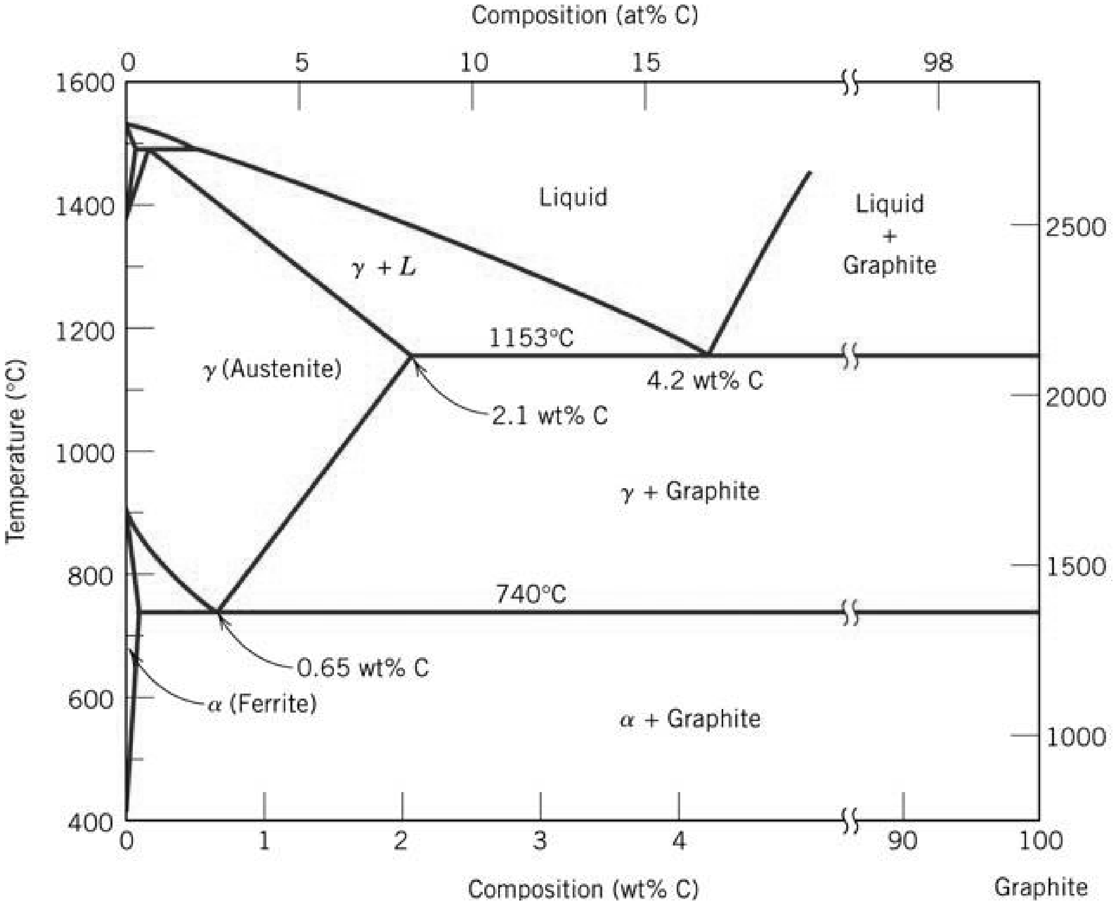

Figure 2.1, the iron-carbon binary phase diagram [74].

There are two crystal structure transformations that occur in iron before melting. Stable ferrite (α iron) with a BCC crystal structure exists at room temperature. At approximately 912 °C, a polymorphic transformation occurs; ferrite becomes an FCC austenite (γ iron). At 1394 °C, the austenite reverts to a BCC ferrite (δ iron) structure. The structure is similar to that of α iron except that it is stable at high temperatures. When alloyed just with carbon the austenite phase is known to be unstable at temperatures below 727 °C. Addition of alloying elements, i.e. in 316 stainless steel, stabilized the structure at lower temperatures. Melting finally occurs at approximately 1538 °C. In iron alloys like 316 SS, carbon is an interstitial impurity which forms solid solutions with α and δ ferrites as well as the austenite. Carbon in iron alloys significantly influences the mechanical properties of ferrite regardless of the small weight percentage (0.2%). The ferrite phases are known to be relatively soft. Mechanically, cementite is very hard and brittle, steels with the presence of cementite increase in strength.

It should be noted that addition of other alloying elements (Cr, Ni, Ti, etc.) brings about changes in the Fe-C phase diagram. Alloying elements alter the temperature of the eutectoid reaction and the relative fraction of pearlite and the pro-eutectoid phase that form. The phase transformation shown in Figure 3 assumes extremely slow cooling rates. Heat treatment for improved hardness properties is extremely difficult at such low cooling rates. Utilizing high cooling rates for low carbon steels can make them docile to heat treatment. High quenching prevents low temperature phase transformations from occurring by only providing a narrow window of time in which the reaction is both thermodynamically favorable and kinetically accessible. This can allow for reduced crystallinity thereby increasing the mechanical properties like hardness and wear resistance. Introducing a martensite structure radically improves the steels hardness, this is achieved by rapidly cooling it through the eutectoid point at which the austenite is unstable.

Phase transformation due plastic deformation: In austenitic stainless steel, martensite may be formed by deformation above room temperature in the case of unstable steels and below room temperature in the case of stable steels, depending on the martensite deformation temperature (M_d). Generally, the martensitic transformation is believed to be triggered when the austenitic stainless steel is deformed at temperatures below M_d, a temperature below which the transformation to martensite readily takes place. Over and above the M_d temperature, several other factors are thought to influence the martensitic transformation. In fact, several investigations have been carried out to understand the martensitic transformation in metastable systems and a review of these investigations brings out the fact that the extent of such phase transformation is controlled by the chemistry of the material, rate of deformation, strain, stress state and temperature of deformation. In other words, for a better understanding of the plastic deformation behavior of austenitic stainless steels, it is a priori to have the knowledge on the martensitic transformation characteristics. Although considerable knowledge base is available on this topic for austenitic stainless steels in general, the understanding development for a particular alloy system under certain deformation conditions cannot be generalized to other metastable systems [75-77].

The chemical composition can be adjusted to increase or reduce the microstructural stability before the imposed deformation. The most important alloy in this respect is Ni in austenitic stainless steels. As can be seen in Figure 2.2 a minimum of the Ni content for the stabilization of austenite exists at about 18 wt. % Cr. Higher Cr contents prohibit the formation of martensite, however the formation of ferrite is promoted, which itself must be prevented by a higher concentration of Ni. Since a high Ni content is connected to high costs, most of the common CrNi steels contain 18 wt. % Cr and 8 wt.% Ni.

The other parameter commonly used is the Md$_{30}$ temperature, which represents the lowest temperature where 50% vol. fraction of induced martensite is formed with a true strain of 0.3. In other words, the lower the Md$_{30}$ temperature is, the greater the stability of alloys designed will be [76]. Recently a linear equation relating the M$_s$ temperature to the composition has been developed for austenitic stainless steels (Eq. 1). This type of relation is important particularly when used to establish the Md$_{30}$ temperature in assessing the cold formability of austenitic stainless steels [77, 78].

Ms (^{o}C) = 1302- 42(%Cr)- 61 (%Ni)- 33 (%Mn)- 28 (%Si) – 1667 (%C + %N) -------- (1)

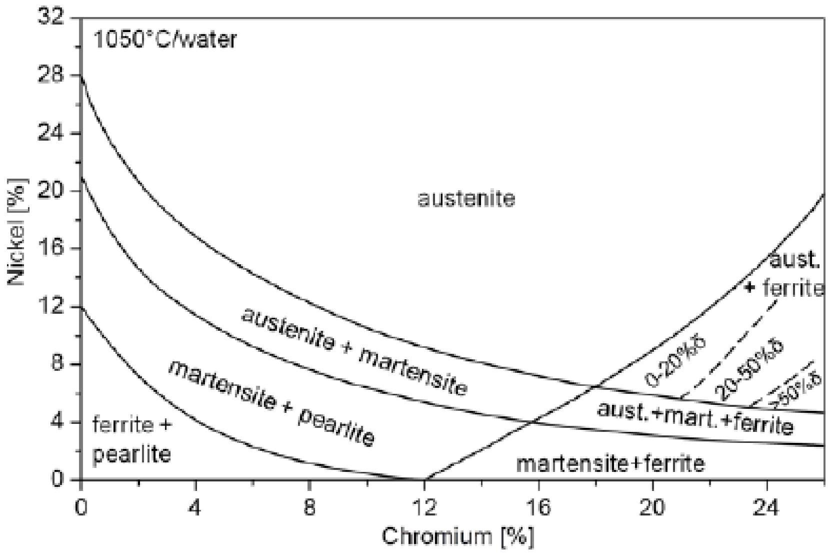

Figure 2.2, effect of nickel and chromium on the microstructural condition of 0.1 wt. % C steel

Md$_{30}$ (^{o}C) = 551- 462(% C+% N)- 9.2 (%Si)- 8.1(%Mn)- 13.7 (%Cr)-29 (%Ni+%Cu)-18.5 (%Mo)- 68(%Nb) ---------- (2)

In some stainless steels, Md$_{30}$ is higher than room temperature and therefore austenite is transformed to martensite due to plastic deformation and lead to decreases the corrosion resistance with martensite formation [79].

General Corrosion Resistance: The molybdenum bearing alloys such as Types 316L and 316Ti stainless steels are more resistant to atmospheric and other mild types of corrosion than the 18Cr-8Ni stainless steels. In general, media that do not corrode 18-8 stainless steels will not attack the molybdenum-containing grades. One known exception is highly oxidizing acids such as nitric acid to which the molybdenum bearing stainless steels are less resistant. Types 316L and 316Ti are considerably more resistant than any of the other chromium-nickel stainless steels to solutions of sulfuric acid. Where condensation of sulfur-bearing gases occurs, these alloys are much more resistant than other types of stainless steels. In sulfuric acid solutions, the acid concentration has a strong influence on the rate of attack.

Pitting corrosion: pitting corrosion is the result of the local destruction of the passive film and subsequent corrosion of the steel below. It generally occurs in chloride, halide or bromide solutions. If a fault in the passive layer or a surface defect results in the local destruction of the former, dissolution of the steel underneath leads to a buildup of positively charged metallic ions, which in turn causes negatively charges (e.g. chloride ions) to migrate near the defect. Even in a neutral solution, this can cause the pH to drop locally to 2 or 3, and can prevent regeneration of the passive layer.

In the passive condition, the current density is in the scale of nanoamperes/cm^2; in the pit, however, it may be above 1A/cm^2. Similarly, the concentration in chloride ions can be thousands of times greater than that in the solution.

Figure 2.3 illustrates the process: the anodic dissolution of the steel leads to introduction of M^+ in solution, which causes migration of Cl^- ions. In turn, metal chloride reacts with water following:

$$M^+Cl^- + H_2O \rightarrow MOH + H^+Cl^-$$

This causes the drop of pH mentioned earlier. The cathodic reaction, on the surface near the pit follows:

$$O_2 + 2H_2O \rightarrow MOH + 4OH^-$$

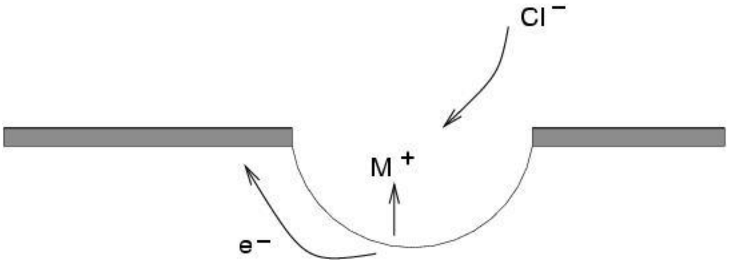

Figure 2.3, Schematic illustration of pitting corrosion

The initiation of pitting has long been associated with the presence of MnS inclusions which are difficult to avoid in the steel making process. It has recently been shown that these inclusions are surrounded by a Cr depleted region which is believed to cause the initiation [80]. The pitting resistance of a stainless steel is affected by its composition. Increasing the Cr content, or adding Mo or N both enhance the pitting resistance, though they are not equally potent in this respect.

Intergranular Corrosion: Type 316 stainless steel is susceptible to precipitation of chromium carbides in grain boundaries when exposed to temperatures in the 425°C to 815°C range. Such “sensitized” steels are subject to inter-granular corrosion when exposed to aggressive environments. Type 316L alloy is available to avoid the hazard of intergranular corrosion. Type 316L provides resistance to intergranular attack even after short periods of exposure in the 425-815°C temperature range. Stress relieving treatments falling within these limits can be employed without affecting the corrosion resistance of the metal. Accelerated cooling from higher temperatures for the “L” grades is not needed when very heavy or bulky sections have been annealed. Type 316Ti possesses the same mechanical properties as the corresponding higher-carbon Type 316, and offers resistance to intergranular corrosion. Although the short duration heating encountered during welding or stress relieving does not produce susceptibility to intergranular corrosion, continuous or prolonged exposure at 422-650°C can produce sensitization of Type 316Ti and of Type 316L stainless steels.

Stress Corrosion Cracking: Austenitic stainless steels are susceptible to stress corrosion cracking (SCC) in halide environments. Although the Type 316, 316L and 316Ti alloys are more resistant to SCC than the 18Cr-8Ni alloys, they still are quite susceptible. Conditions that produce SCC are: (1) presence of halide ion (generally chloride), (2) residual tensile stresses, and (3) temperature in excess of about 60°C.

Stresses result from cold deformation or thermal cycles during welding. Annealing or stress relieving heat treatments may be effective in reducing stresses, thereby reducing sensitivity to halide SCC. Although the stabilized Type 316Ti and low carbon “L” grades offer no advantage as regards SCC resistance, they are better choices for service in the stress relieved condition in environments which might cause intergranular corrosion.

2.3 Ti-6Al-4V alloys

Titanium and its alloys have been used as an implant material for various medical applications for more than 30 years. They are favorable to orthopedic implants due to their high specific strength and fatigue resistance, excellent biocompatibility properties, and good corrosion resistance [81-83]. The most widely used titanium alloy contain a combination of alpha and beta stabilizers and are heat treatable to various degrees; and beta alloys, which are metastable and contain sufficient beta stabilizers such as (Mo, V) to completely retain the beta phase upon quenching, and can be solution treated and aged to achieve significant increase in strength. The basic criterion for opting a metallic implant material is that it should possess the property of biocompatibility i.e. showing desirable local or systemic effects in the body and thus producing the most appropriate beneficial host response. The excellent biocompatibility is achieved by a dense TiO_2 layer that is always present in oxidizing media as in the human body fluid, and is rebuilt within milliseconds after any damaging [84-85]. Another advantage of titanium is the low elastic modulus compared to steel and Co-Cr alloys thus reducing the effects of stress shielding.

Phase diagram: The microstructure of Ti alloys depends on the alloy composition and its thermal history. To show the changes in microstructure with temperature variation a Titanium-Aluminum phase diagram is used, see Figure 2.4. The binary phase diagram shows the expected phases at equilibrium for different combinations of aluminum content. In the Ti-Al phase diagram there are two allotropic forms of solid titanium: hexagonal-closed packed (hcp) α Ti which is stable at room temperature and up to 882 °C and body centered cubic (bcc) β Ti which is stable from 882 °C to the melting temperature. In Ti-6Al-4V, the alloying elements aluminum and vanadium are alpha and beta phase stabilizers, respectively. Aluminum is the only standard metal that raises the beta transus temperature. The metal is miscible in both alpha and beta phase. Vanadium is a beta stabilizer that is completely miscible with βTi. Only 6% Al is present in Ti-6Al-4V therefore, Ti3Al and other phases are not taken into account. It should be noted that the phase transformation shown in Figure 2.4 is only for slow cooling rates. Water quenching can produce extremely high cooling rates; therefore, the phase diagram does not fully highlight the resulting phases.

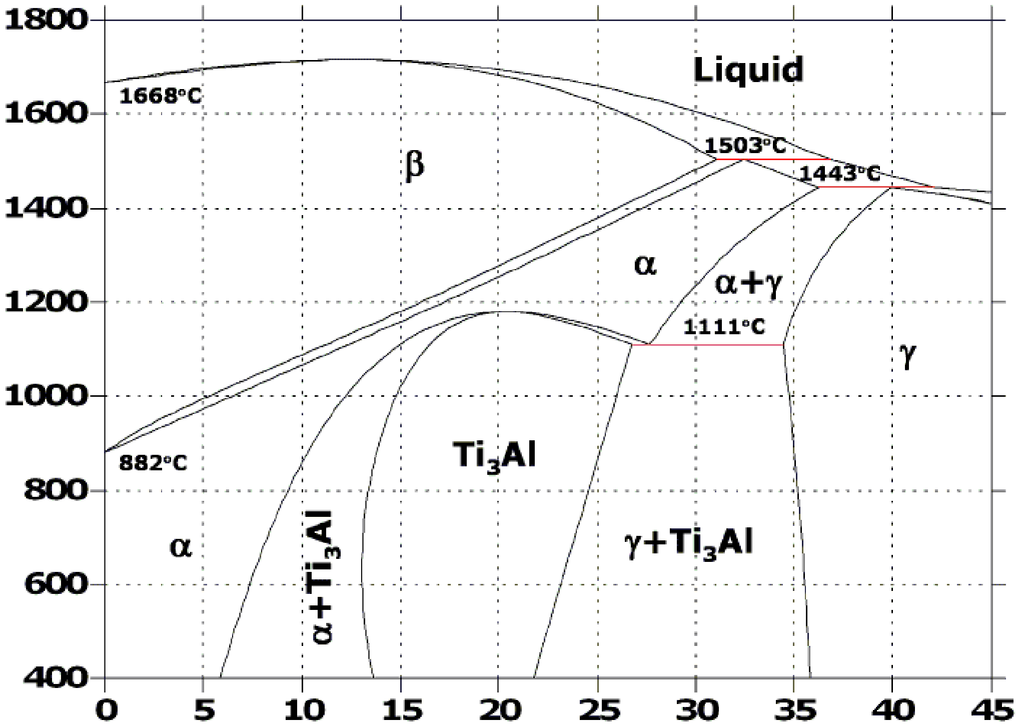

Figure 2.4, the titanium-aluminium binary phase diagram [86]

Microstructural Developments in Ti-6Al-4V: Ti alloys are generally classified into three different categories: α/near-β, α+ β, and β alloys [88]. The α+ β alloys are the most widely used because of the wide range of microstructural features that can be created by different thermomechanical processing and heat treatments [88-89]. The α phase with a hexagonal-closed packed (hcp) structure and the β phase with a body centered cubic (bcc) structure are the low- and high temperature phases, respectively [90]. The presence of the ductile α phase and the less ductile but stronger metastable β phase is enabled by the addition of phase stabilizers, aluminum and the vanadium, respectively. However, the exact amount of α and β phases ultimately present and their microstructural morphology is largely a function of processing parameters. While grain size and shape play a role, the mechanical properties found in these alloys are mostly determined by α and β crystal structure transformations. The added aluminum is distributed approximately equally between α and β phases and is not prone to segregation. Vanadium is β isomorphous with bcc titanium and does not form intermetallic compounds. The trace amounts of carbon, oxygen and nitrogen remain as interstitial elements and serve to stabilize α phase. A wide variety of microstructures can be generated in Ti-6Al-4V by careful control of thermomechanical process parameters. As seen in Figure 2.5, the two key factors are the highest temperature achieved beyond the β- transus temperature and the rate of cooling that follows. The α phase present at the time of cooling can remain relatively equiaxed (globular with equal axis). Any β phase transformed to α or martensite upon cooling from above the β -transus is referred to as transformed β. This transformed β can be very acicular or elongated. The amount of equiaxed α and the coarseness or fineness of the transformed β products affect mechanical properties.

Processing of α + β titanium alloys in α + β phase region can produce the bimodal (duplex) microstructure, which consists of equiaxed primary α grains and transformed β [88-89]. Enhanced fatigue crack initiation resistance and low-cycle fatigue resistance are the main mechanical benefits of the bimodal structure [92].

Coloration between corrosion and microstructure: A limitation of Ti-6Al-4V use arises from the corrosion related release of harmful products including aluminum which is related to neurotoxin effects and vanadium which is cytotoxic [93-94]. The release of vanadium ions by the way of passive dissolution or another process involving wear can cause discoloration of the surrounding tissue or an inflammatory reaction causing pain and even leading to loosening owing to osteolysis [95]. Corrosion fatigue triggered by body fluids is another factor limiting the use of titanium for biomedical implants [96]. Further, the presence of particulate corrosion and wear products in the tissues surrounding the implant may ultimately result in a cascade of events leading to periprosthetic bone loss [97]. Hence protection of an implant material from corrosion is indispensable.

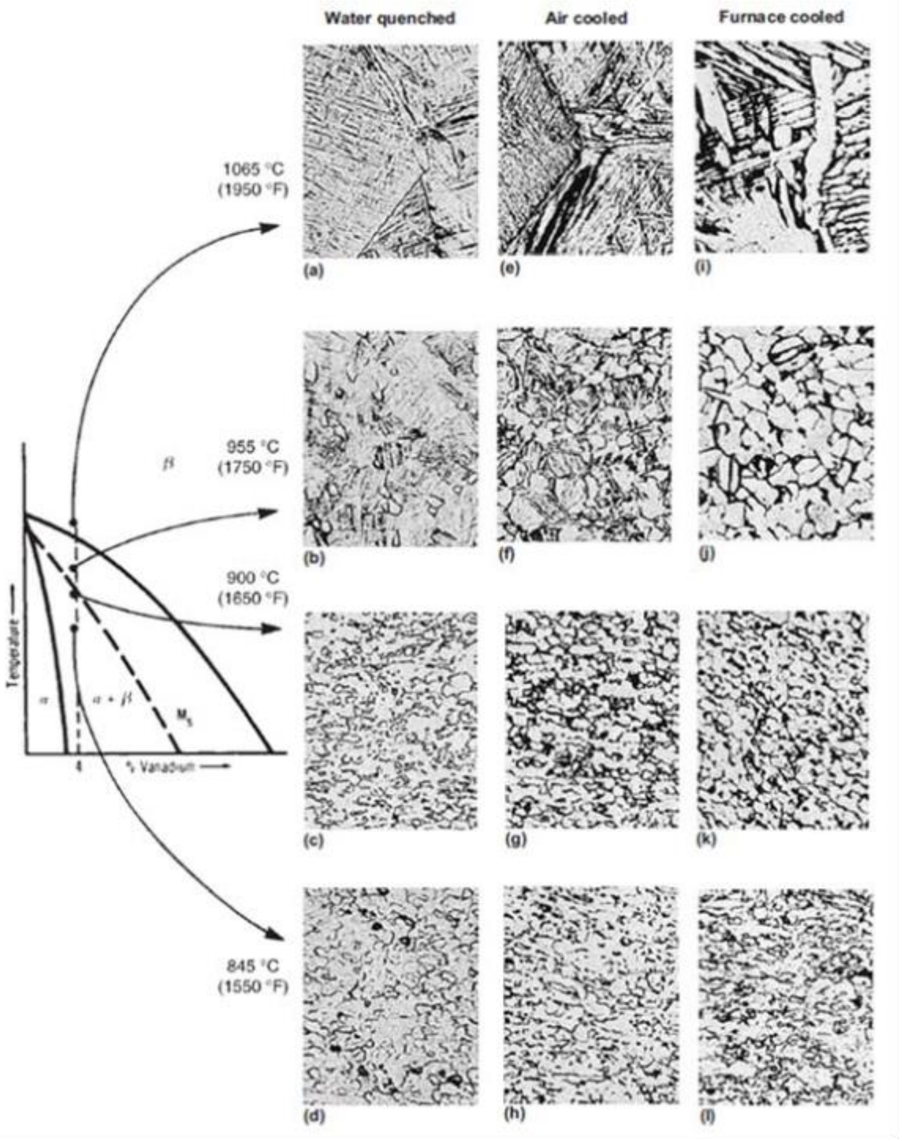

Figure 2.5, Effect of maximum heating temperature and subsequent cooling rate on Ti-6Al-4V microstructures [91]

Titanium and its alloys are found to offer superior corrosion resistance in several media including the human body environment. This high corrosion resistance has been attributed to the formation of a thermodynamically stable TiO_2 oxide layer on the surface. However, the titanium oxide gradually decreases in oxygen content from TiO_2 at the surface to titanium (III) oxide (Ti_2O_3) and titanium monoxide (TiO) closer to the metal oxide interface [98]. The effectiveness of the Ti passive film is threatened by three fundamental problems: general dissolution in a reducing acid, localized breakdown of the oxide layer in the presence of detrimental anions such as chlorides or bromides, or mechanical interruption or depassivation [99]. However, the corrosion resistance of Cp Ti is found to vary significantly with heat treatment temperatures. Fukuzuka et al. [100] documented that the corrosion rate of Cp Ti was very high when heat-treated at low temperature (823 K) as well as high temperature (1273 K). The decrease in corrosion resistance at low temperature is attributed to the textural changes, whereas the reduction at high temperature is due to the formation of acicular alpha phase. Thus, the texture and crystal structure play a significant role in corrosion behavior of pure Ti. However, the corrosion rate of the specimen heat-treated at 1073 K has been reported to be very low due to the precipitation of iron in the grain boundaries. On the other hand, the corrosion resistance of titanium alloys is found to vary with the alloy composition, environment and microstructure. The corrosion study done by Dull et al. [101] on α+β Ti–6Al–4V alloy reveals that the passive corrosion current density (i_p) increases with the α to β ratio owing to the formation of a galvanic cell between the two phases. The galvanic cell is formed between the two phases due to the enrichment of Nb or V in the beta phase and enrichment of Al in alpha phase. Also, studies carried out [102] on Ti–6Al–2Sn showed that the Widmanstätten structure obtained on β solution treatment is less corrosion resistant due to compositional variations within the structure.

In contrast to α+β alloys, β titanium alloys exhibit superior corrosion resistance. However, their corrosion resistance is also found to depend on various determinants such as composition, environment and microstructure [103]. The effect of the composition can be realized from the fact that the corrosion resistance of a β alloy such as Ti–5Mo–5Zr–3Al is higher when compared to pure Ti. Moreover, the corrosion resistance of the β alloy Ti–12Mo–6Zr–2Fe is very similar to the α+β alloy Ti–6Al–4V [103]. The effect of microstructure on corrosion is explained by Yu and Scully study [104] on βST Ti–15Mo–3Nb–3Al. From their research, it is observed that the β solution treated microstructure shows superior corrosion performance when compared to the aged one. The decrease in the resistance of the aged sample is due to the partitioning of the alloying elements occurring during aging process [105]. Thus, the corrosion studies carried out on various alloys, clearly indicate that the composition and microstructural features decide the corrosion characteristics of the alloy in addition to the texture and crystal structure.

In this study, we aspire to get the best performance of implant materials through a combination of the best mechanical properties and corrosion behavior. Most of the recent works to develop different microstructures have focused on the mechanical behavior. The effects of microstructure on the corrosion properties of titanium alloys have not been studied extensively. Therefore, the current study aims to investigate the relationship between microstructure and corrosion behavior of the Ti-6Al-1 4V alloy in Ringer’s solution as a simulated body fluid at 37 C.

2.4. Surface treatment and modification

Excellent mechanical properties, biocompatibility and high corrosion resistance are the main factors should be available in the implants materials. Surface modification through mechanical surface treatment and the coating by bioactive materials are the most suitable methods to satisfy the factors mentioned above. It's well known that the shot peening (SP) surface treatment improves the fatigue strength of the material largely [41]. Moreover, SP is widely applied as a surface treatment to enhance the interaction between biomaterials and the host tissue [34–38]. In principle, the procedure leads to roughing the surface which helps to adherence proteins well and subsequently initiate bone tissue development on the implant surface.

The hydroxyapatite (HA) coating is another surface modification technique that used widely to enhance the osseointegration of orthopaedic and dental implants [68]. These coatings [$Ca_5(PO4)_3OH$] consist of 39.9% Ca, 18.5% P, 41.4% O and 3.4% OH (values in weight percentage) and the Ca/P molar ratio is 1.67. This chemical composition resembles the mineral component of human bones and hard tissues [106]. Furthermore, HA coating of biomaterials improves the corrosion resistance by forming a barrier against the dissolution of metal ions from the substrate at the same time as promoting its bone bonding ability. However, there are several factors should be controlled in the two surface modification techniques to getting the desired results and this will be discussed in detail.

2.4.1. Shot peening

SP is a cold-working process in which a component surface is bombarded by tiny particles called shot (tiny balls of steel, cut wire, glass or ceramic). These small shots serving as hammer strike on the surface of the parts being treated. The kinetic energy of the shot stream is thus transferred to the material, resulting in plastic deformation of the surface, i.e. dimples. SP-induced plastic deformation in the near-surface regions leads to increases the dislocation density and compressive stresses layer. This layer has beneficial effects on fatigue and corrosion fatigue life. It can also increase the resistance of metallic materials such as steel, titanium, magnesium and aluminum alloys for hydrogen-assisted cracking. This is because fatigue cracks will not easily propagate in a compressively stressed zone [107- 108]. Since nearly all fatigue and stress corrosion failures originate at the surface of a part, the compressive stresses created by shot peening provide an increase in fatigue life of the part [107, 109]. The maximum residual compressive stress produced at or under the surface of a part by shot peening is normally at least half the yield stress of the material being peened.

The most important process parameters of shot peening are shot size and hardness, surface coverage, and the peening intensity. The quality and effectiveness of shot peening depend on the control of each of these independent parameters [108]. Typical shot is made of steel, ceramic or glass beads with size ranging from 50 µm to 6 mm in diameter. Impact velocities can reach up to 150 m/s. Target's material properties such as yield stress, hardening rate and cyclic softening or hardening and characteristics of shot such as size, material, velocities and shape influence the residual stress state.

It's known that the shot peening generates a rough surface and subsequently reduce the corrosion resistance. The surface active area became larger and the corrosion rate became faster with the increase in surface roughness [44]. Since the purpose of the shot peening process is to improve the mechanical properties of implants materials under corrosion environment, therefore the best combination of both a high strength and a minimum corrosion rate should be taken into consideration.

Shots type and size play the important role in the peening process. The selection of the shot is based on the peened material, its hardness, intensity, allowable contamination and permissible surface roughness [110]. The shot size depends on the smallest feature size that needs to be peened. Moreover, the shot size has a significant effect on the corrosion behavior. "In the one study [59], was observed that surface blasting treatment by using big steel ball-diameter led to a reduction in the corrosion current density as well as increasing the surface microhardness.

As a result of the different of influencing parameters on the results of shot peening process, J. O. Almen (1940) developed a standard method to measure the kinetic energy transferred by a shot stream using a strip of steel exposed to identical peening conditions as the treated component, in which the height of strip's deflection is determined after peening, as shown in Fig. 2.6.

The kinetic energy of shot flux is evaluated by the so called Almen-intensity. The measurement of the Almen intensity is performed by determining the effect on standard strips made of steel SAE 1070 CRS (cold rolled spring steel) with standard hardness of 44-50 HRC. Almen strips are classified into three types: ‘A’, ‘N’ and ‘C’. They differ in their thickness while have the same width and length. ‘A’ and ‘N’strips are predominantly used for SP with the cast, glass and ceramic shots. ‘C’ strips are rarely applied and are thicker than the other two. The fixed Almen strip is first exposed to the shot stream, and removed from the holding fixture. The arch height of the peened strip measured by a gage (Almen gage) is representing the Almen intensity.

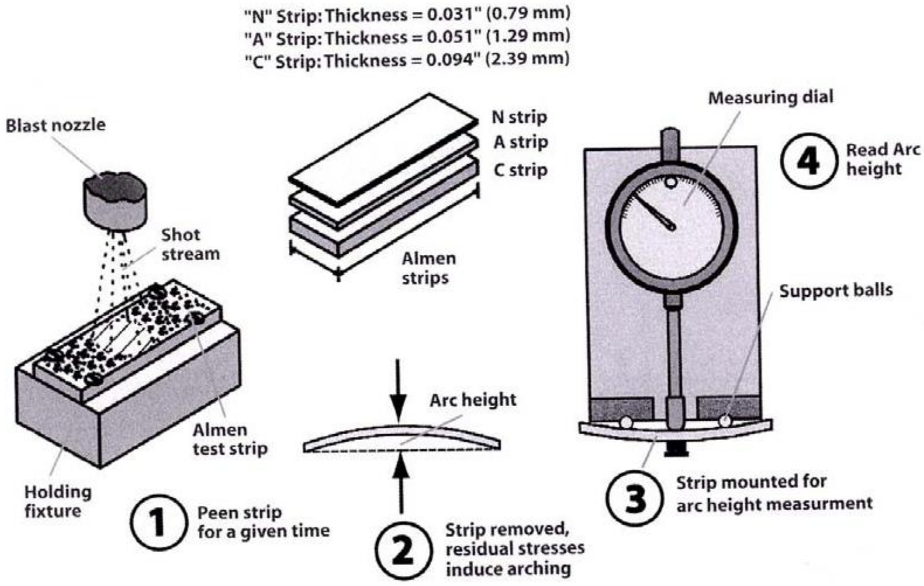

Figure 2.6, determination of Almen intensity of SP [111].

The intensity of shot peening at saturation refers to the earliest point of the saturation curve that, if the exposure time is doubled, the arc of height increased by 10% or less, Figure 2.7 [112]. Coverage of a shot peened surface is significant in performing high-quality SP. Coverage is the ratio of the area covered by hits and the whole surface area. A definite and quantitative relationship between coverage and exposure time exists. Peening at less saturation is not recommended because of the presence of un-peened surface areas. The peening time to coverage larger than 100% is defined as a multiple of the exposure time required to produce saturation. For example, 150% coverage represents a condition in which the sample or workpiece has been exposed to the blast 1.5 times the exposure required to obtain saturation.

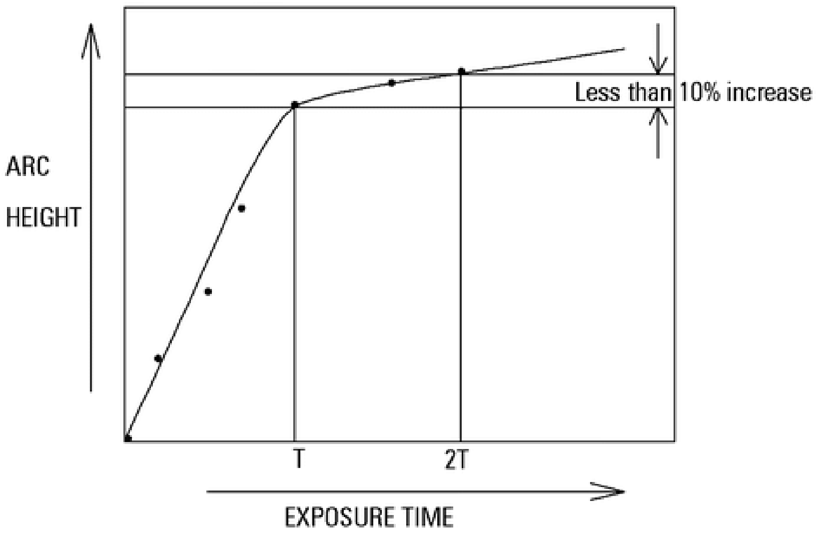

Figure 2.7, arc height vs. exposure time Schematic [112]

2.4.2. Hydroxyapatite coating

Hydroxyapatite (HA) is a bioactive ceramic coating that widely applied to improve the bone response in orthopedic and dental implants. It forms strong chemical bonds with bone in vivo, because of its chemical similarity to the apatite of the host's bone, while remaining stable under the harsh conditions encountered in the human body [113-114]. HA coating of biomaterials improves the corrosion resistance by forming a barrier against the dissolution of metal ions from the substrate at the same time as promoting its bone bonding ability [43,70,115]. There are several techniques to synthesize HA coating including plasma spraying [116], sol-gel [117], pulse laser deposition [118], biomimetic coating [119], and electrochemical deposition [120-121]. Plasma spraying is the most commonly used coating technique for this purpose. However, there are many drawbacks of plasma sprayed-coatings affecting its long-term stability i.e. its lifetime. Plasma sprayed HA coating is produced under extremely high temperatures that can easily destabilize crystal structure of the HA, causing its decomposition into a mixture of HA, calcium oxide, tri-calcium phosphate, tetra-calcium phosphate and considerable amount of amorphous phases [122]. Such transformation of the amorphous phase to crystalline oxide, may lead rise to cracking as a result of volume change (shrinkage). Cracking of the coated layer is often observed, primarily due to rapid temperature fluctuations and solidification of the coating. These cracks may also cause loss of adhesion of the coating, leading to coating delamination, premature wear and, finally, implant failure [122-124]. Therefore, other techniques have been proposed to apply HA coating on metallic implant substrates. Among these techniques is the chemical deposition of HA coating that allow obtaining a homogeneous coating at low temperature on dental and orthopedic implants with complex geometry (internal cavity) or macro-porosities. This coating method is simple and low cost-advantages for use in the biomaterials industry. Furthermore, the low temperature nature of the chemical deposition method allows the incorporation and therefore controlled release of osteoinductive drug such as bone morphogenetic proteins into the coating during the HA coating deposition process [125-126]. Thus, ensure a sustained release of the drug into the surrounding bony tissue after the joint replacement surgery that may reduce the healing time after the operation and the risk of a revision surgery.

The adhesive strength of the coatings is the combination of chemical bonding and mechanical interlocking between the coating and the implant substrate. The adhesive strength between the coating and the implant substrate is a very critical factor; it greatly influences the long-term performance of the HA-coated implants [127-128]. Separation of the coating layer from the implant during service in the human body results in adverse effects on the implants and the surrounding tissue caused by detached particles [129]. Adhesive strength could be improved by sintering that enhances the chemical bonding and the formation of possible intimate interconnects between HA coating and the implant substrate [130].

The mechanical strength of HA-based coatings could be improved by sintering. Sintering refers to the consolidation of HA coatings, at appropriate temperatures, to form dense polycrystalline aggregates through physical and chemical changes. It was reported that sintering of HA-coated substrates with high thermal expansion coefficient such as 316L, is advantageous, because of the induction of compressive residual stresses that act to close cracks and therefore “toughen” the coating [131]. Commonly, Sintering refers to the process by which a system of powder particles in contact is consolidated to form dense polycrystalline aggregates through physical and chemical changes when subjected to appropriate temperatures. The effects of sintering and post heat treatments on the properties of HA coating is a developing field of research [118,130,132-134]. However, there is a lack of published data addressed the influence of sintering on the characteristics of chemically deposited HA coating and the corrosion behavior of the implants. The current work intended to synthesize and characterize chemically deposited HA coating and investigate the effects of sintering at various temperatures on the crystallization, adhesive properties and corrosion behavior of samples.

2.5. Sever plastic deformation (SPD)

Severe plastic deformation (SPD) can be considered as advanced processes in the manufacturing of implant materials. They offer superior mechanical properties which regard necessary requirements for the biomaterials implants that are predominantly utilized in mechanically loaded regions to stabilize and promote the integrity of fractures, replace joints, and realign bone fragments. Furthermore, to mechanical endurance under physiological strains and stresses, the biomedical materials should implement the biological potential to promote the healing process. There are several biophysical factors conflicting with the functionality of implants materials in such applications, among which surface features as microstructure and topography are confirmed to play a significant role. A large body of knowledge has been provided by previous works on the effects of surface topography on cellular function at the cell substrate interface. Cell adhesion, morphology, proliferation, migration, and differentiation have been investigated in a wide variety of cell types ranging from fibroblasts to mesenchymal stem cells (MSCs) [135-137].

In the recent years, the role of crystal size in altering the material, biological characteristics has been studied in different series of material. Indeed nanograined (NG) surfaces are regarded to have the potential to alter absorption of proteins that interfere cell adhesion and control and enhance subsequent cell functions and tissue growth [138]. Relative increase in surface area and improved reactivity are the distinctive intrinsic features of NG materials giving them the potential to manipulate their interaction with cells.

It is well known that SPD can result in extreme grain refinement obtaining ultra-fine grained (UFG) material through large deformations applied at high strain rates. Two complementary strategies have been developed in attempts to create NG or at least UFG solids, namely, "bottom-up" and "top-down" approaches. In bottom-up approach, atoms, molecules and even nanoparticles can be used as the building blocks for the creation of complex structures. Examples of this technique include inert gas condensation [139], electrodeposition [140], physical vapour deposition, chemical vapour deposition [141] and ball milling with subsequent consolidation [142]. SPD such as rotary swaging (RS) [43,143-144], equal channel angular pressing (ECAP) [146] high pressure torsion (HPT) [146], friction stir processing (FSP) [147] and cold rolling [148] are belong to the top-down approach and theses processes are capable of leading to substantial grain refinement from the coarse-grained materials (CG), so that the grains can be reduced to sub-micrometre or even nanometre range. Materials produces by means of SPD provide several advantages in comparison NG materials produced by other methods. These benefits are connected with the fact, that the SPD technique provides large scale billets of fully dense bulk NG materials without any residual porosity, impurities from ball milling or complicated long-term processing, like cryo-milling, of difficult to handle metallic powders. It was found that the corrosion resistance of UFG aluminum and stainless steel 316L processed by SPD such as ECAP [149], rotary swaging (RS) [43] is improved in comparison with that of its counterpart material. Thereby, it is promising to enhance the corrosion resistance by processing the bulk materials through SPD, meanwhile retaining better mechanical properties.

2.6 Wettability Characteristics

The ability to promote bone cell anchorage, attachment, spreading and growth is a key factor for a successful biomaterial in orthopedics. It is important that the interface between the implant and host tissues do not induce any deleterious effects such as chronic inflammatory response or formation of abnormal tissue. The wetting of a surface to a liquid and the spreading of the liquid are vital features in surface design for biomedical implants. The wetting of biomaterials is influenced by various factors [150]. Surface energy of the biomaterial, which varies as a function of intrinsic chemical composition and net polarity, strongly influences wettability. Surface energy is to a solid what surface tension is to a liquid, and both have a unit of J/m2 (energy concept) or N/m (mechanical concept). If the surface energy of a biomaterial is higher than the surface tension of a liquid, the liquid becomes wettable on the substrate displaying low contact angle and the substrate is ‘hydrophilic’. For the reverse case, the liquid will form a droplet with high contact angle and the substrate is ‘hydrophobic’. Besides, viscosity of the liquid and surface roughness of the solid influence wettability. Wetting can be determined from the equilibrium contact angle. If $\theta < 90°$, the liquid is said to wet the solid and a zero-contact angle is known as complete or perfect wetting.

2.7 Motivation

The human body is an aggressive chemical environment, and the mechanical purpose of the implant requires cyclical loading. Due to these requirements, the typical artificial hip has a lifetime between ten and twenty years. Typically, this lifetime is long enough to last the patient to the end of their natural life, since arthroplasty patients are commonly about 60 years old. However, if the implant lifetime were increased significantly, then younger patients suffering from less-significant osteoarthritis would have the option of joint replacement without the concern of needing a revision surgery in the foreseeable future. To provide such an implant, the material would have to meet several requirements, which are detailed below.

Biocompatibility: Biocompatibility can be defined as “the ability of a material, device or system to perform without a clinically significant host response in a specific application”. While this term is rather broad, biocompatible materials can be further subdivided into being either bioactive or bioinert. Bioactive materials are those which positively interact with the surrounding tissue on a biological level, while bioinert materials, on the other hand, produce no biological interaction on their own and are simply tolerated by the surrounding tissue.

Most materials which meet the mechanical requirements to be used as implants are only bioinert as a result of their chemical dissimilarity to human tissue. A common strategy is a creating a bioactive surface on these bioinert materials through the use of surface modifications, such as coating with a different, bioactive material.

High corrosion resistance: Corrosion resistance is a counterpart to biocompatibility: it is certainly important that the implant not harms the biological environment, but it is also important that the biological environment not harms the implant. The human body is dangerously corrosive: it is hot, wet, and salty. For this reason, a great deal of research for combating corrosion is to use an alloy that forms a passivating layer and through a production of anti-corrosion coatings.

Mechanical properties: The most important mechanical properties that help to decide the type of material are hardness, tensile strength, Young´s modulus and elongation. The most reasons that cause the failure of the implants material related to the fatigue. Since most replacement joints are meant to be walked on, cyclical loading is expected. One million cycles per year is a reasonable estimate, so the implant should reliably last tens of millions of cycles. Considering also the danger of environmentally assisted cracking, due to the biological conditions, and it is clear that fatigue resistance is essential for an implant material. Therefore, the improvement of the mechanical properties and fatigue resistance under hard corrosion conditions should be imperative.

Cost: Finally, the cost is an important contributing factor for the selection of implant materials. Often, manufacturers must strike a suitable balance between a material’s performance and cost.

2.8 Aims of study

The success of implants in the human body depends on many factors such as biocompatibility and biofunctionality in the environment wherein the implants are placed. Therefore, this work aims to improve the performance of the materials that used as biomedical implants. The following points represent the goals of this study:

- Developing a combination of bulk and surface plastic deformations through rotary swaging, cold rolling and shot peening (SP) to keep good mechanical properties on the AISI 316L, 316Ti stainless steel and Ti-6Al-4V alloys.
- The effects of these treatments on fatigue, corrosion fatigue, microhardness, surface microstructure, surface roughness and corrosion resistance of the three alloys will be investigated.
- Applied hydroxyapatite coating (HA) on the deformed and the shot peened materials to enhance their corrosion resistance and biocompatibility.
- Investigated the effects of sintering at various temperatures on the crystallization, adhesive properties and corrosion behavior of HA coating.
- Evaluating several processing parameters such as the size of ceramic shots, Almen intensity, and the coverage percent during the SP to document the parameters that lead to optimum surface properties and corrosion behavior of materials used in this study.
- Investigate the wettability of shot peened samples with and without hydroxyapatite coating.
- Study the relationship between microstructure and corrosion behavior of the Ti-6Al-4V alloy in Ringer's solution as a simulated body fluid at 37^{o}C.

Chapter three

Experimental Work

This chapter covers the materials and methods used in this research. Two kinds of stainless steel alloys were used (as an economic choice) in this study to compare them in terms of corrosion resistance, especially after several mechanical processes. Moreover, Ti-6Al-4V alloy was used due to their low Young's modulus that makes it a very good choice for the material used in the femoral stem component of the hip by reducing the stress shielding of bone.

3.1 Materials and processing

In this study, two types of austenitic stainless steel (316Ti and 316L) and Ti-6Al-4V alloys have been used. For 316Ti stainless steel, was received in plate form with thickness of 30 mm, chemical composition is given in Table 1. The material was cold-rolled to different deformation degrees. The deformation degree is defined as $\varphi = \ln (A_{\circ}/A)$, where $A_{\circ}$ is the starting cross sectional area and A is the final cross sectional area. Samples of 20 x 10 x 2 mm were cut from the as-received and the deformed materials.

Table 1: Chemical composition of SS 316Ti and 316L in wt. %

Element wt%	C	Si	Mn	P	S	Cr	Mo	Ni	Ti	Fe
316Ti	0.024	0.50	1.57	0.038	0.015	17.75	1.94	10.2	0.23	Bal.
316L	0.03	0.44	1.24	0.03	0.03	18.48	1.75	11.96	-	Bal.

Cylindrical rod of AISI 316L stainless steel with a diameter of 25 mm was used in this study. The chemical composition of AISI 316L is shown in Table 1. The rod was hot swaged at 800^{o}C using a rotary swaging (RS) machine down to 11 mm diameter. Simple disk specimens were cut from the as received rod and RS materials. The Ti-6Al-4V was received as cylindrical rod with equiaxed microstructure. The diameter of bar was 20 mm with chemical composition displayed in Table 2.

Table 2: Chemical composition of Ti-6Al-4V in wt. %

Element	C	Al	V	Fe	O	Ti
wt%	0.08	6.34	4.23	0.25	0.18	Bal.

The rod was hot swaged at 900^{o}C using a rotary swaging (RS) machine down to 10 mm diameter. Simple disk specimens were cut from the bar swaged and subjected to two heat treatment conditions, to obtain DU and GL microstructure by annealing at 970°C and 840°C respectively for 1 h followed by water quenching. The materials were subjected to a final heat treatment at 500°C for 24 h followed by air cooling.

Rotary swaging

Rotary swaging is a hammer forming process for the reduction of cross-sections of solids, tubes and wires. The main application is the production of circular, concentric reductions. However, the process can also be used in producing other regular forms e.g. hexagonal, octagonal and square sections. Some of the advantages of rotary swaging include short cycle times, good surface finishes and tight size tolerances. A schematic sketch of a typical swaging unit is shown in Fig. 3.1 [151]. The main part of the unit consists of a 'spindle', with guiding slots which contain the dies (D) and hammer blocks (C). There is a cage containing rollers (B), which itself is contained within the machine retaining chamber (A). When the hammer blocks are between any of the rollers, there is an opening in the dies, Fig. 3.1a. As the hammer blocks strike the rollers, the dies close in and exert a blow onto the material.

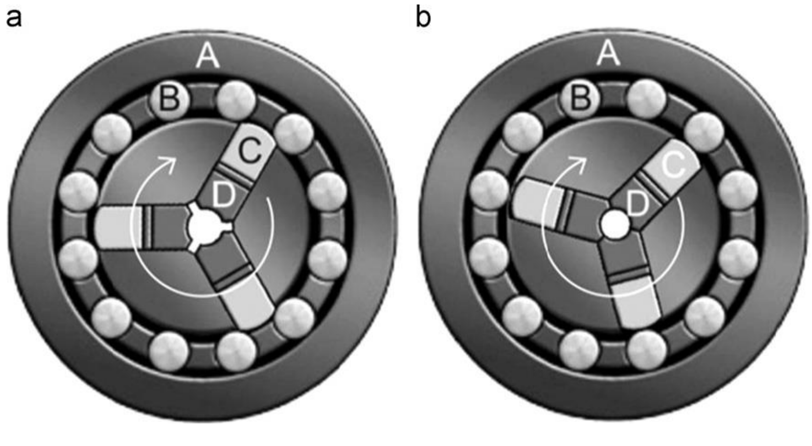

Figure 3.1, schematic picture of a typical swaging unit [151]

During rotation cycle of the spindle the dies close and open several times depending upon the number of rollers in the roller cage (B) and the number of dies used (D), e.g. in case of Fig. 3.1b, the dies close 12 times in one cycle. The spindle rotates normally at 300-500 rpm, and during each cycle the hammer blocks repeatedly strikes the rollers (B). The frequent opening and closing of the dies allow the component to be fed into the swaging machine with little effort from the operator or automatic feeder.

3.2 Shot peening

SP was performed on Injektoranlage – model 1000 shot peening machine. Ceramic balls of three different sizes, 125-250, 450 and 850 µm, were selected combined with two peening coverage percentages 100 and 200% and two levels of peening intensity 0.22 and 0.28 mmA. Ceramic balls composed of 65% ZrO2 and 35%SiO2, Figure 3.2. Coverage here is defined as the percentage of a surface area that has been indented at least once. The optical microscope can be used to make sure that 100 % of the surface has been impacted. The 200% coverage here was obtained by extending the SP duration to 2 times of the minimal time required to obtain 100% coverage. The peening intensity, related to the mass and velocity of the shots striking the surface, is determined by measuring the arc height of Almen strip peened to saturation according to the procedure described in [152]. Therefore, by using the smaller shots and the highest available pressure in the shot peening machine, the maximum Almen intensity that have been achieved was 0.22 mmA. The shots (850 µm) have been used to achieve the two Almen intensities 0.22 and 0.28 mmA. Optical microscopy was used to document the microstructure after SP.

Shots were propelled by air blast system into the path of high pressure air and accelerated through a blasting nozzle which is directed at the specimen. Then each shot functions as a small ballpeen hammer, impinging the specimen surface. A recycling system is operated to collect the blasted shots and refuel them back to the nozzle. In the process, the distance between the nozzle and the rotating specimen was kept constant to control the uniform coverage of the specimen. The major parameters of peening setup are listed in Table 3.

The key parameter to characterize the effect of SP is the peening intensity, which was gauged using Almen-strip A by determining the deformation of peened strip, i.e. the arch height of the bent strip. The corresponding Almen intensity achieved by the setups in the Table 3, which is moderate for samples.

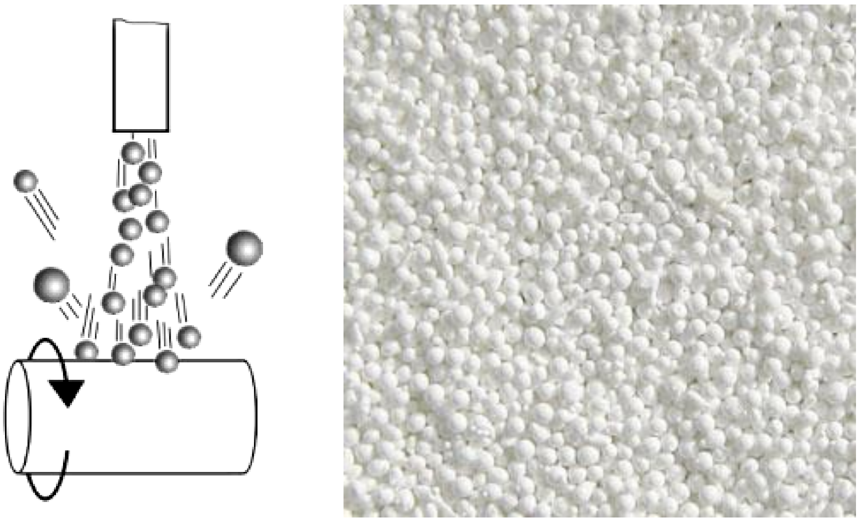

(a) (b)

Figure 3.2, (a) peening process and (b) peening media (ceramic shot ZrO2 and SiO2)

Table 3: Parameters of SP

Peening media	**Size of media, µm**	**Distance between nozzle and specimen**	**Peening Pressure, bar**	**Peening's time**	**Almen Intensity**
Ceramic	850	90 mm	3.0	40	0.22 mAA
	450	90 mm	5.0	40	
	125-250	90 mm	7.5	45	
	850	90 mm	4.0	40	0.28 mmA

3.3 Hydroxyapatite coating

Hydroxyapatite (HA) coating is widely applied for biomaterials because of its chemical similarity to the mineral component of bones. The bioactive nature of HA coating enhances the formation of strong chemical bonds with surrounding bones. In this work the hydroxyapatite was synthesize and characterize chemically deposited. This method has an advantage of depositing a homogenous HA coating on dental and orthopedic implants with complex geometry (internal cavity) or macroporosities. Moreover, this coating method is simple and low cost-advantages for use in the biomaterials industry.

Simple disk specimens were cut from the as received rods 316L. The samples were ground to 600 grit using silicon carbide (SiC) papers followed by ultrasonic cleaning in ethanol bath. The samples were coated by HA coating. HA coating was prepared using chemical deposition method. The samples were firstly soaked in 2M KOH solution for 2 h at 90°C in order to prevent the cracking caused by the evolution of H_2 during the dissolution of substrate.

3.3.1 The mechanism of coating formation

The chemical path deposition method depends principally on the following chemical reaction:

$$10Ca(^{+2}) + 6PO4(^{-3}) + 2OH(^{-}) = Ca_{10}\,(PO_4)_6(OH)_2$$

The coating solution was prepared using potassium hydroxide (KOH), calcium nitrate tetra hydrate ($Ca(NO_3)_2.4H_2O$ as a source of Ca^{2+} ions, and potassium dihydrogen phosphate (KH_2PO_4) as a source of PO_4^{3-} ions. The reaction rate has been controlled by using chelating agent. Ethylene diammine tetra acetic acid (EDTA) has been used as complexing agent, which has ability to "chelating" metal ions such as Ca^{2+} and PO_4^{3-}. When Ca^{2+} and PO_4^{3-} ions are mixed together in an aqueous solution, they immediately react even at room temperature to precipitate HA in the form of a powder rather than a coating. Hence, control of the reaction rate through EDTA is necessary for coating deposition. The solubility of EDTA is very low in acidic solution but high in alkaline solution. The deposition of hydroxyapatite was done by preparation of two solutions.

The first solution was prepared by dissolving 0.69M KOH in 75ml double distilled water followed by adding 0.49M EDTA (Ethylene diammine tetra acetic acid). 0.15M KH_2PO_4 was added to the solution after the complete dissolution of the salts. EDTA is ionized as it is dissolved in KOH. The reaction is exothermic and continues until EDTA is completely ionized. After the completion of the EDTA ionization, the solution is strongly alkaline with pH 14. No reaction occurs during the addition of KH_2PO_4. The solution was then continuously stirred on a magnetic hot plate.

The second solution was prepared by dissolving 1.14M of $Ca(NO_3)_2.4H_2O$ in 25ml of double distilled water. This solution is then slowly added to the first solution. The complete mixing of the two solutions is accompanied by the formation of $Ca(OH)_2$ white precipitates that dissolved to form EDTA– Ca^{2+} chelate compounds. As the temperature increases, Ca^{2+} ions are dissociated from the compounds and bond with PO_4^{3-} ions to form an HA coating.

The chemical bath deposition was performed in 50 ml beaker in which the samples were vertically suspended. The beaker was heated in a water bath up to 70°C for 2 h, after that the temperature was slowly raised to 95°C. After 3 h deposition, the substrates were removed, washed in water, and air dried at room temperature. The process was repeated up to three times to get a proper coating thickness and ensure that the whole surface is covered.

3.3.2 Coating sintering and adhesive test

The effects of sintering and post heat treatments on the properties of HA coating was investigated. Sintering was carried out on the HA-coated samples for 1 h at 500, 600 and 700 ^{0}C followed by air-cooling. The bonding strength of the HA-coated samples before and after heat treatment was tested using a standard tensile adhesion test. Figure 3.3 represents a schematic assembly of the test. The test includes the attachment of a stainless steel screw with same dimension of the samples to the HA-coated surface using Epoxy Adhesive (EpoFix Resin and EpoFixHardner), which was left to cure at room temperature for 24 h. After the coated sample/screw assembly was installed on a platen, the screw was then pulled until failure.

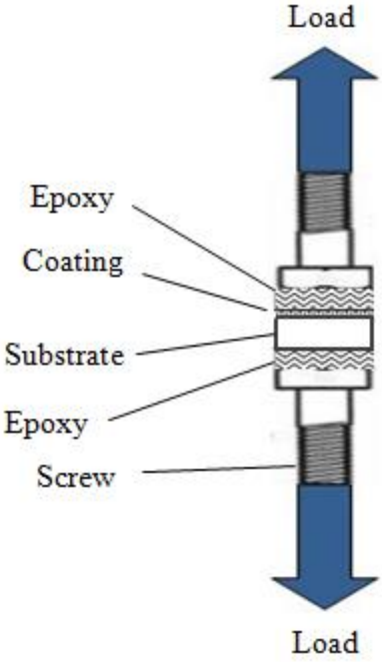

Figure 3.3, schematic assembly of adhesive testing

3.3.3 Coating analysis

The crystal structure of the HA coating before and after sintering was investigated with an X-ray diffractometer operated with CoKα radiation at a scanning rate of 1°/min over a 2θ range of 20-60°. The experiments were conducted using a Siemens D5000 diffractometer at 40kV and 40mA. The surface morphology and composition of all coatings were identified by scanning electron microscopy (SEM) “HITACHI X-50” operated at 20 kV with work distance 15mm and energy dispersive X-ray spectroscopy (EDX) using Ultra Dry Compact EDS

Detector from Thermo Scientific. Surface roughness after various surface conditions expressed in arithmetic average (Ra), maximum roughness (Rmax) and Average Maximum Profile (Rz) was measured by a profilometer supplied by the company Perthen Mahr.

3.4 Surface layer properties

Shot peening surface treatments influence on the surface finish strongly. Therefore, it was necessary to characterize surface layer properties.

3.4.1 Microhardness

Hardness is the resistance of a material to localized deformation. The term can apply to deformation from indentation, scratching, cutting or bending. Indentation hardness tests were used to demonstrate the hardness of materials, wherein a small indenter is forced into specimen surfaces, resulting in the formation of impressions or indentations. The depth or size of the indentation was a measure of the hardness index number. Microhardness acquired at lower indentation load is considered as an effective criterion to describe the local strength levels of the materials in the microscopic scale.

The measurements of microhardness-depth profiles were conducted on the SP specimens at the identical process parameters by using a Struers Duramin hardness tester with a Vickers hardness pyramidal indenter and an applied load of 50 g. The indenter is pressed on the mechanically polished surface sample by the loading force and maintained for a dwell time of 10 to 15 seconds. After the dwell time is complete, the indenter is removed leaving an indent in the sample that appears square shaped on the surface. The size of the indent is determined optically by measuring the two diagonals of the square indent. Microhardness test was conducted from the surface to the center of the specimen cross-section at an interval of 50 µm.

3.4.2 Residual stress

The residual stress against depth profile at the near surface region produced by SP is measured by the hole-drilling strain-gage method. Namely, the test surface is bind hole drilled. The method involves attaching strain gage rosettes to the surface, drilling a hole in the vicinity of the gages and measuring the relieved strains using an oscillating drill with 1.9 mm diameter driven by an air-turbine with a rotational speed of 200,000 rpm. The induced strains in the surface layers were measured at drilled depths of about every 10 µm. The measured strains are then related to relieved principal stresses through a series of equations using the macroscopic Young's modulus and Poisson's ratio. A strain gage rosette with three elements of the general type schematically illustrated in Fig. 3.4 is placed in the area under consideration. The numbering scheme for the strain gages follows a clockwise convention. A hole is drilled at the geometric center of the strain gage rosette to a depth of about 0.4 of the mean diameter of the strain gage circle. The residual stresses in the area surrounding the drilled hole relax. The entire measurement process is PC-controlled. This ensures a high degree of measurement reliability.

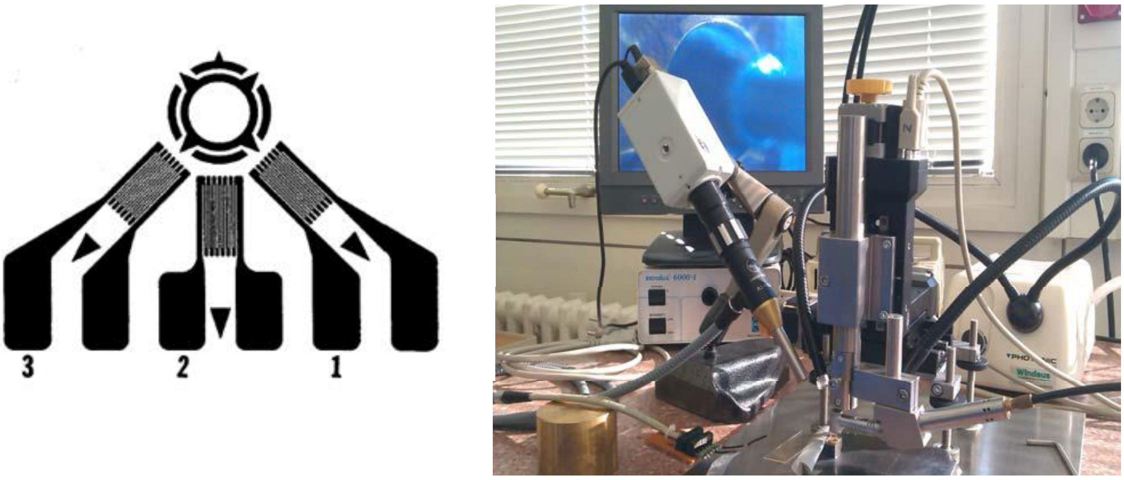

Figure 3.4, hole drilling rosette to the left and high speed special (oscillating) drill to the right

3.4.3 Roughness

Roughness includes the fine irregularities in the surface texture, usually including those resulting from production processes such as marks caused by machining or surface treatments, or SP. The surface roughness after various surface conditions expressed in arithmetic average (Ra), maximum roughness (Rmax) and Average Maximum Profile (Rz) was measured by a profilometer supplied by the company Perthen Mahr.

The Mean Roughness (Roughness Average Ra) is the arithmetic average of the absolute values of the roughness profile ordinates. Ra is one of the most effective surface roughness measures commonly adopted in general engineering practice. It gives a good general description of the height variations in the surface. R_{max} is the maximum peak to valley height. Rz is a parameter that averages the height of the five highest peaks plus the depth of the five deepest valleys over the evaluation length.

3.4.4 Wettability of surface

The surface wettability was quantified through a sessile drop test to obtain the droplet contact angle on each sample. The surface wettability measurements were also done on the shot peened samples coated with HA. All samples were cleaned up using ethanol, rinsed in distilled water, and dried before the measurement. A Ringer's solution droplet was deposited three times on the surface of each sample. The static droplet on sample’s surface was recorded using a high resolution camera. The angle of contact was calculated five seconds after a drop of liquid was placed onto the surface. The contact angle Ө was calculated by the formula (1):

$\Theta = 2 \tan^{-1}(2h/d)$ degrees ---------------------- (1)

Where Ө: is the contact angle of drop
H: is the height of apex
D: is the diameter of the drop

3.5 Microstructure analysis

3.5.1 Optical microscopy

The standard metallographic preparation was carried out to reveal the microstructures under the optical microscope, including sectioning, mounting, grinding, polishing and etching. Cold mounting was used by mixed solution of 25 g epoxy resin and 5 g hardener was used to fix the specimens after 12 hours aging. Then Grinding was carried out manually on a series of SiC papers with different grits ranging from 500 to 4000. Following polishing was done semi automatically by Struers LaboForce machine. Specimens fixed in sample holder within the 35 polisher were ground on rotating woven cloth plates and further polyester cloth using lubricants (e.g. soft soap) and diamond pastes having average grain sizes of 6 and 3µm sequentially and finally polished with OPS suspension. Prior to etching, specimens were cleaned in ultrasonic bath for 30 seconds. The microstructures of the stainless steel were revealed by etching using glyceregia (15 ml HCl , 10 ml Glycerol and 5ml HNO_3) for approximately 1 minute. Etching of Ti-6Al-4V was carried out by immersion in Kroll’s etchant which consists of 92 ml distilled water, 6 ml HNO3 and 2 ml HF for one and a half minutes.

3.5.2 Scanning electron microscopy (SEM)

The scanning electron microscope (SEM) is a type of electron microscope that images the samples surface by scanning it with a high energy beam of electrons in a raster scan pattern. The electrons interact with atoms in the sample, producing various signals that contain information about the sample's surface topography and composition. Magnifications in a SEM can be controlle over a range of up to 6 orders of magnitude from about 10 to 500,000 times. The surface morphology and composition of samples were identified by scanning electron microscopy (SEM) ‘‘HITACHI X-50’’ operated at 20 kV with work distance 15 mm and energy dispersive X-ray spectroscopy (EDX) using Ultra Dry Compact EDS Detector from Thermo Scientific.

3.5.3 Phases analysis

The phases analysis after sever bulk and surface plastic deformation were recorded by X-ray diffractometer operated with CoKα radiation at a scanning rate of 1°/min over a 2θ range of 20-60°. The test set-up is schematically shown in Figure 3.5. Samples were cleaned with acetone and rinsed with deionised water prior to analysis. A z scan was used to position samples at correct heights on the z drive prior to XRD measurement. The experiments were conducted using a Siemens D5000 diffractometer at 40kV and 40mA. The diffraction patterns produced were plotted with intensity against 2 theta angles, and used for phase transformation and crystallinity analysis.

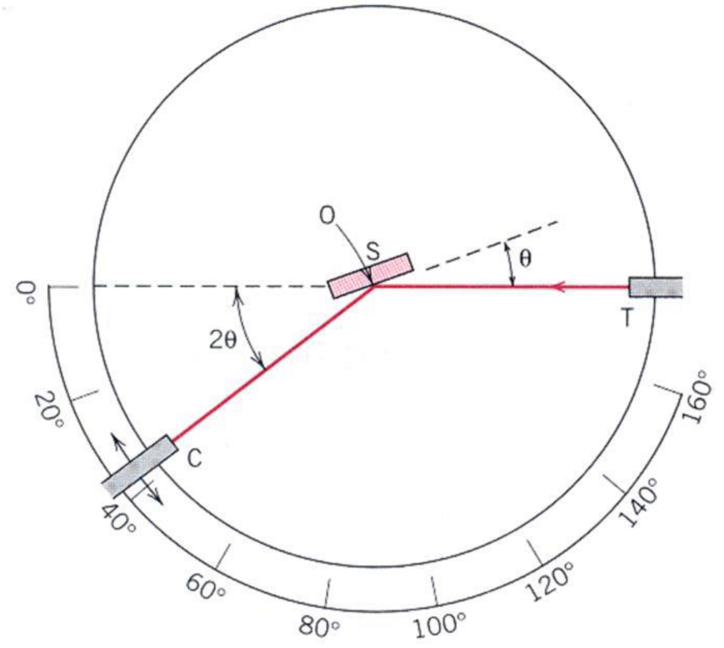

T= x-ray source, S = Specimen, C = detector, and O = axis.

Figure 3.5, schematic and image of XRD set-up [153].

3.6 Mechanical properties examination

3.6.1 Tensile test

Tensile tests were performed using threaded cylindrical specimens having gage lengths and diameter of 50 and 5 mm, respectively (Figure 3.6). Tests at room temperature were carried out on Instron 5582 universal testing machine (Figure 3.7) at the load of 50kN, with straining speed of 1 mm/ min.

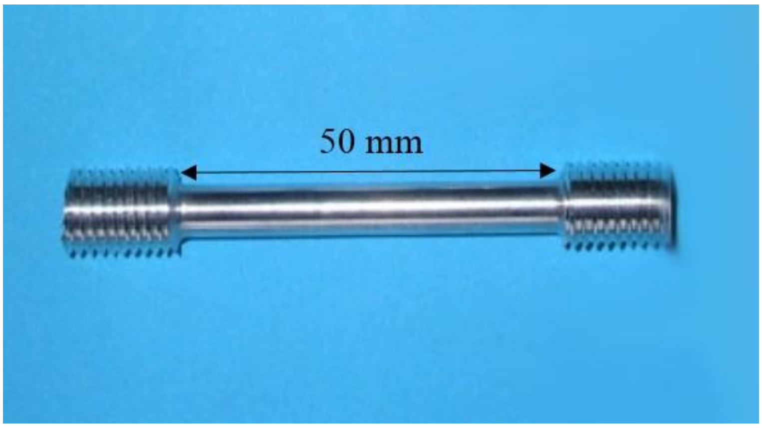

Figure 3.6, standard tensile specimens

Figure 3.7, universal testing machine (Instron 5582)

3.6.2 Fatigue testing

Fatigue tests were achieved using Mayes-GTG, Rolls Royce rotating beam fatigue machine (R= -1), where R represents the stress ratio (R= σ_{min} / σ_{max}), at frequency of 50 Hz at room temperature in air which served as a reference environment. Tests were performed on hour-glass-shaped specimens with gage diameter of about 6 mm (Figure 3.8). In order to exclude the machining effects on fatigue properties, before testing, all the specimen were first ground off about 100 μm by a series of SiC papers with grits ranging from 500~2400, then electrolytically polished for another 100 μm in a mixed solution of 750 ml methanol and 250 ml HNO3. During polishing, the voltage was kept constant at 20 V, temperature used was -8^oC and the polishing time was 5 min.

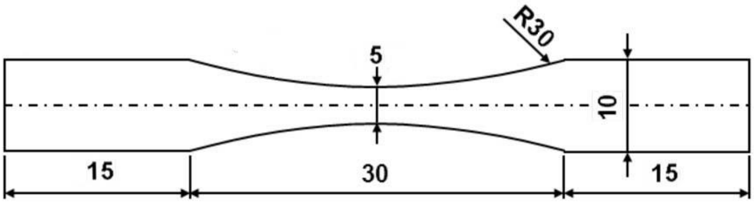

Figure 3.8, cylindrical fatigue specimens

3.6.3 Corrosion fatigue testing

As possible, all the tests concerning biomaterials should be done under similar environment to the human body. Therefore, the corrosion fatigue test has been done by using Ringer solution at 37^oC. The corrosion environment chamber (Figure 3.9) used in conjunction with the Rolls Royce dynamic rotating beam loading machine at a frequency of 50 Hz (R = -1). An amount of 10 liters of Ringer solution (8.6 NaCl, 0.3 KCl, and 0.48 CaCl2 gm/l) were used in a heating jacket as a pump and preheated of the solution. The solution was circulated through the heating jacket and chamber at a flow rate of 25 ml/min. The test solution was renewed every 5 days. Testing was continuously conducted until the samples failed or until the number of cycles reached 1×10^7 cycles.

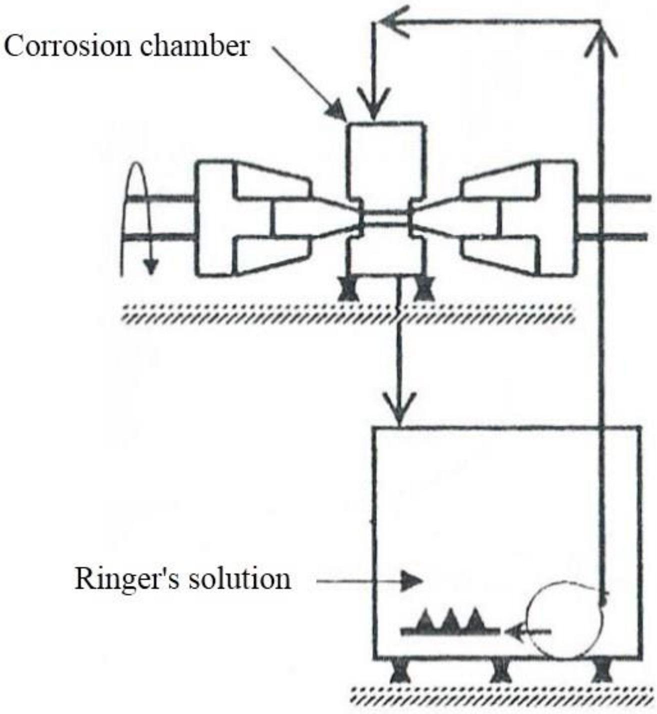

Figure 3.9, Corrosion fatigue cell

3.7 Electrochemical tests

To accelerate the corrosion process and save the time, electrochemical tests were used to directly amplify the impact of corrosion processes. This was possible since electrochemical tests use a fundamental model of the electrode kinetics associated with corrosion processes to quantify corrosion rates. Two types of electrochemical testing were employed. The first was the potentiodynamic polarization and the second was the impedance spectroscopy techniques. Electrochemical experiments were conducted by using a round bottom polarization cell using VersaSTAT3 potentiostat from the Princeton Applied Research company, interfaced to a computer (Figure 3.10). The tests were conducted according to ASTM G5-94 [154]. The electrolyte used for simulating human body fluid conditions was Ringer's solution, prepared using laboratory grade chemicals and distilled water. The composition of the Ringer's solution used was (in gm/l) 8.6 NaCl, 0.3 KCl, and 0.48 $CaCl_2$. A conventional three-electrode cell was used, the counter electrode was a platinum sheet and all the potential values were reported relative to saturated calomel electrode (SCE). The specimens were prepared by connecting a copper wire to one face of the specimen; the specimen with the attached wire were then cold mounted in resin and dried in air for 24 h at room temperature. The samples were consecutively wet grinded with 1200, 2400 and 4000 SiC paper and then polished sequentially using 6, 3 and 1 lm diamond paste. The samples were cleaned ultrasonically in an acetone bath and dried in a cool air stream before the electrochemical measurements. Haber Luggin capillary was placed close to the working electrode. A constant electrolyte temperature of 37±1°C was maintained using a heating jacket. All the potentiodynamic polarization studies were conducted after stabilization of the free corrosion potential. The scan rate used was 1 mV/s. The corrosion rate was determined using the Tafel extrapolation method. The surfaces of the corroded samples were examined using SEM and light microscope. The Corrosion rate (in mpy), which was extracted from the extrapolation of the Tafel lines of each polarization curve, is calculated by the following equation:

$$C.R. = \frac{I_{corr} \times K \times EW}{\rho \times A}$$

Where I_{corr} = corrosion current density in Ampere (A), K = constant that defines the units of corrosion rate (1.288 × 105 mils/A cm year), EW = equivalent weight in (g/equivalent), ρ = density and A = sample area in cm2. The equation indicates that, corrosion rate is directly proportional to corrosion current density.

All electrochemical impedance spectroscopy (EIS) were performed at the same three-electrode cell arrangement than potentiodynamic polarization curves. In order to reach steady state, each sample was held at least for 20 minutes at open circuit previous to the EIS experiments. EIS were conducted in the frequency range of 100 kHz-100mHz, with a potential sine wave amplitude of 10mV(rms). The impedance diagrams are given in the Nyquist plots representation.

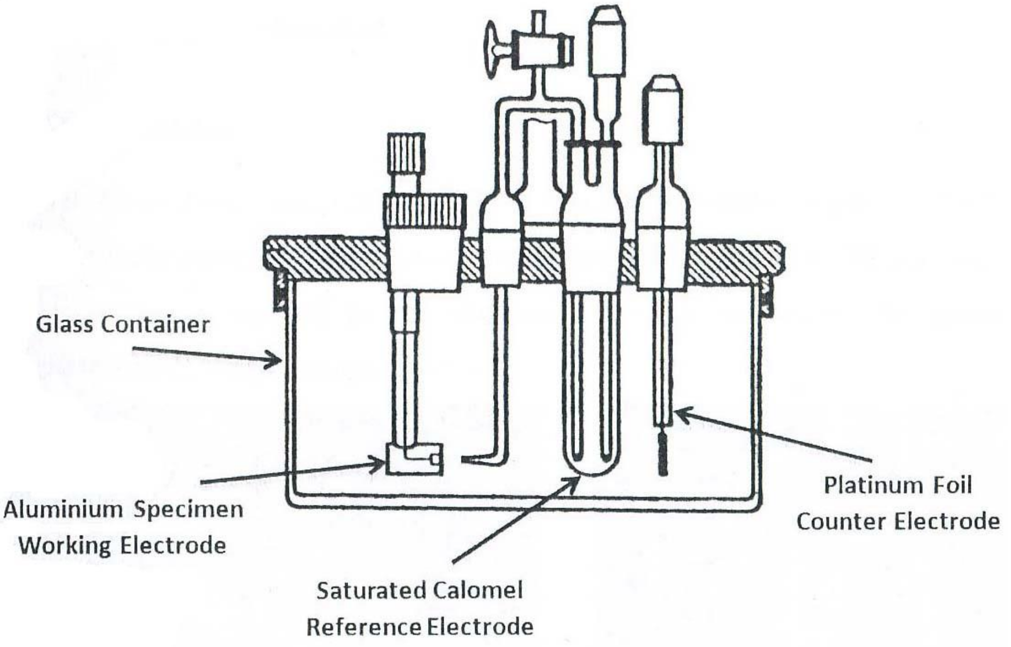

Figure 3.10, Schematic diagram of polarization of the three electrode cell

Chapter four: 316Ti and 316L Stainless Steel
Results and Discussions

4.1 Materials characterization 316Ti SS

The microstructures of 316Ti SS before and after cold rolling are illustrated in Figure 4.1. Figure 4.1a represents a typical equiaxed grained austenitic microstructure of the non-deformed ($\varphi = 0$) condition, after cold rolling ($\varphi = 2.25$) the grains were highly deformed and elongated in rolling direction (Figure 1b). The average grain size of the as-received material is about 38 µm. It was hardly to calculate the grain size of the deformed material. The effect of cold rolling on the hardness is shown in Figure 4.2. With an increase in the degree of deformation by cold rolling, the hardness increased significantly from about 125 to 430 HV10. The ductility of the non-deformed material ($\varphi = 0$) was of 0.44 (strain to fracture, $\varepsilon F = \ln (Ao/AF)$. After deformation, the material still had a ductility of 0.19 that ensures a suitable workability. Moreover, the deformed material exhibited higher strength values, which are suitable for higher fatigue lifetime. This strong strain hardening is mainly due to the very low stacking fault energy (SFE) in austenitic stainless steels in which plastic deformation is characterized by the dissociation of perfect dislocations in Shockley partial dislocations and the formation of wide stacking faults [155, 156]. Furthermore, part of the observed strengthening may be caused by strain-induced transformation of the austenite to martensite as shown in Figure 4.3 [148].

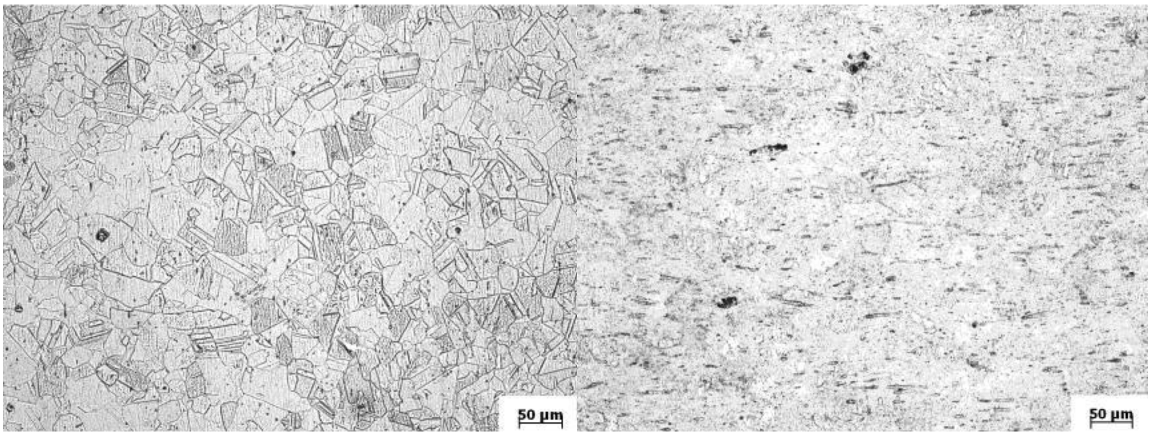

a) $\varphi = 0$ b) $\varphi = 2.25$

Figure 4.1, microstructure of SS 316Ti

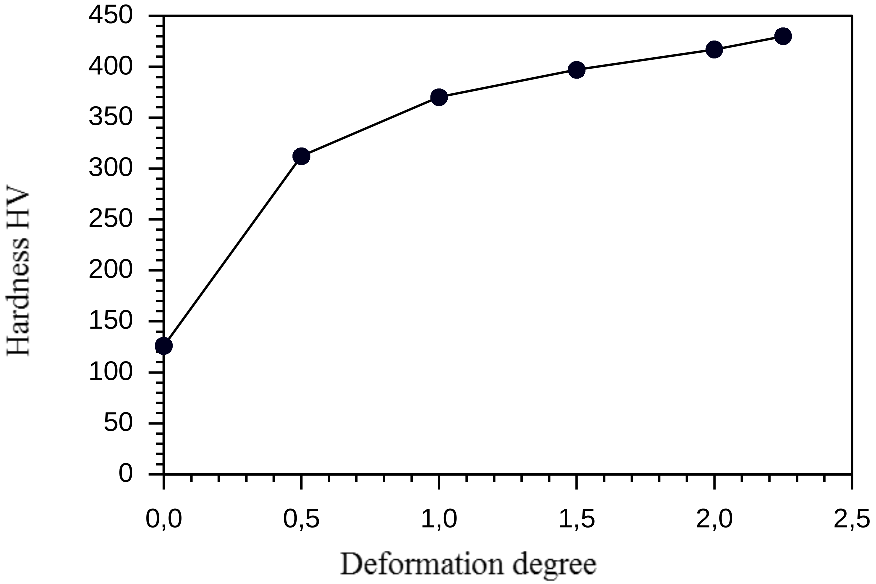

Figure 4.2, relation between hardness and deformation degree in cold rolling

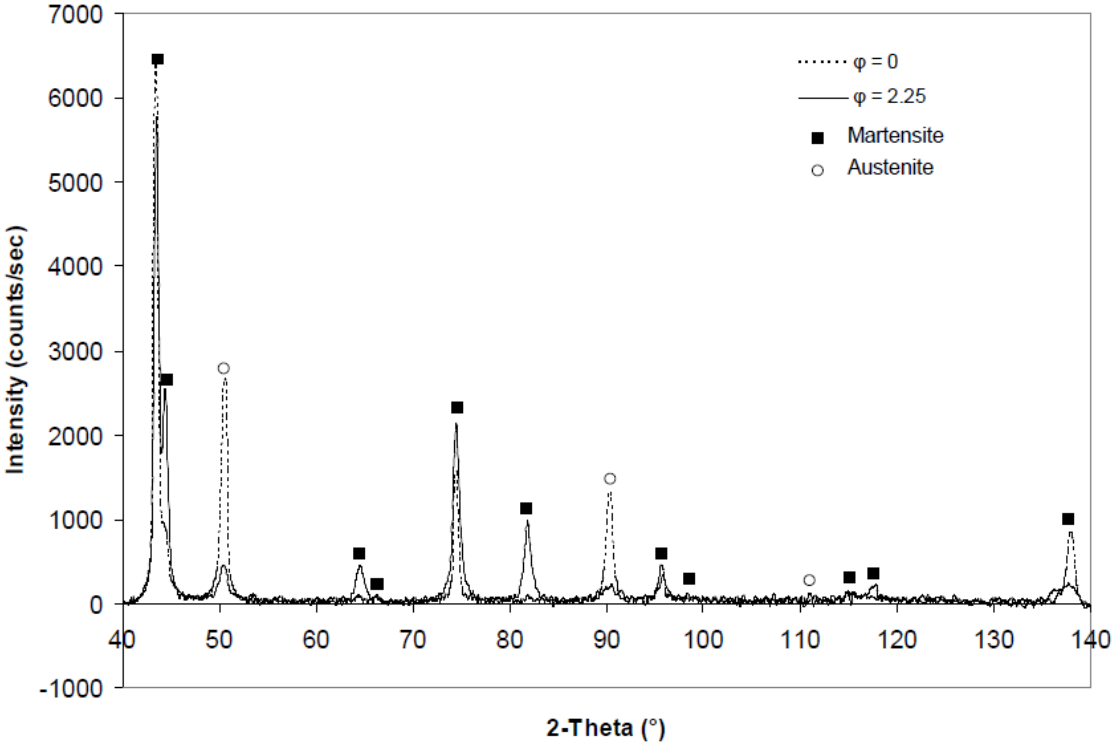

Figure 4.3, XRD spectra of non-deformed (φ = 0) and highly deformed (φ = 2.25) SS 316Ti

4.2 Materials characterization 316L SS

The microstructure of the deformed materials by rotary swaging (RS) is shown in Fig. 4.4. Starting with the as-received (AR) condition having a grain size of about 35µm (Figure a), the grains size was drastically reduced by RS down to 3 µm grain size (Figure b). Equiaxed austenite grains with twining boundaries were found in the RS specimen-matrix. There were narrow inclusions band caused by the elongation of the grains.

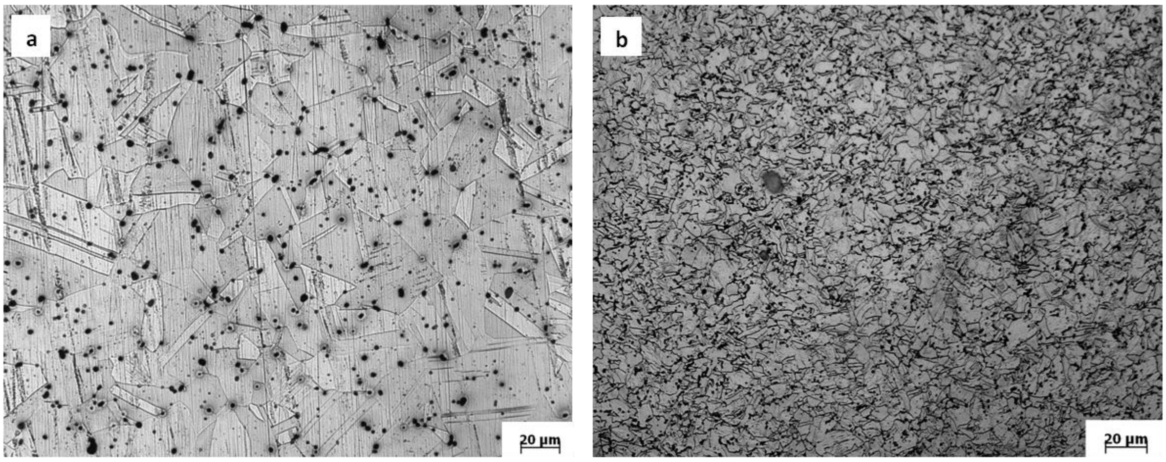

Figure 4.4, Microstructure of a) as-received and b) swaging ϕ = 1.65

Figure 4.5 shows the development of the hardness values as a function of the deformation degree. The hardness of the AR material was 218 HV10 which increased up to 322 HV after deformation of φ = 1.65; the increase in hardness values is due to the high dislocation density that is built inside the materials during RS, and the evolution of fine sub-grain structure within the original structure.

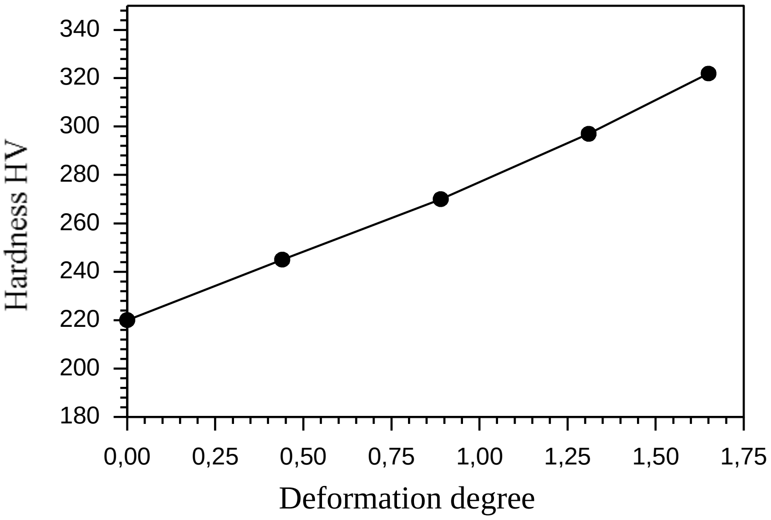

Figure 4.5, hardness vs. deformation degree

The tensile properties of the AR and RS conditions are summarized in Table 4.1 (yield strength, ultimate tensile strength and elongation percent to fracture). The AR material revealed higher work hardening capability (UTS–YS) than the RS material. The total elongation to fracture drastically reduced as a result to decrease the ductility and increase the hardness of the RS material.

Table 4.1: Tensile properties of as received and swaged conditions

Condition	YS (MPa)	UTS (MPa)	Elongation (%)
AR	454	696	55.1
RS $\phi = 1.65$	647	736	35.3

XRD was used to study the phase transformations taking place after RS and SP. Figure 4.6 shows the XRD patterns of the AR, RS and SP (0.28 mmA) samples. The patterns revealed no significant effect of deformation provided by RS and SP on the austenite transformation. Similarly, D. Kirk and N.J. Payne [157] did not observe any martensitic transformation even with gross surface plastic deformation in the AISI 316 stainless steel whilst martensite formation was easily induced by plastic deformation in the AISI 304 stainless steel. The reason for this is attributed to the higher nickel content in the AISI 316 stainless steel that's made the austenite phase more stable. The difference between the intensities of XRD patterns (Figure 4.7) of AR and SP samples refers to high roughness and defects of SP material. The high surface roughness leads to a decrease in the intensity that caused by micro absorption of the X-rays due to the microstructure of the surface sample [158].

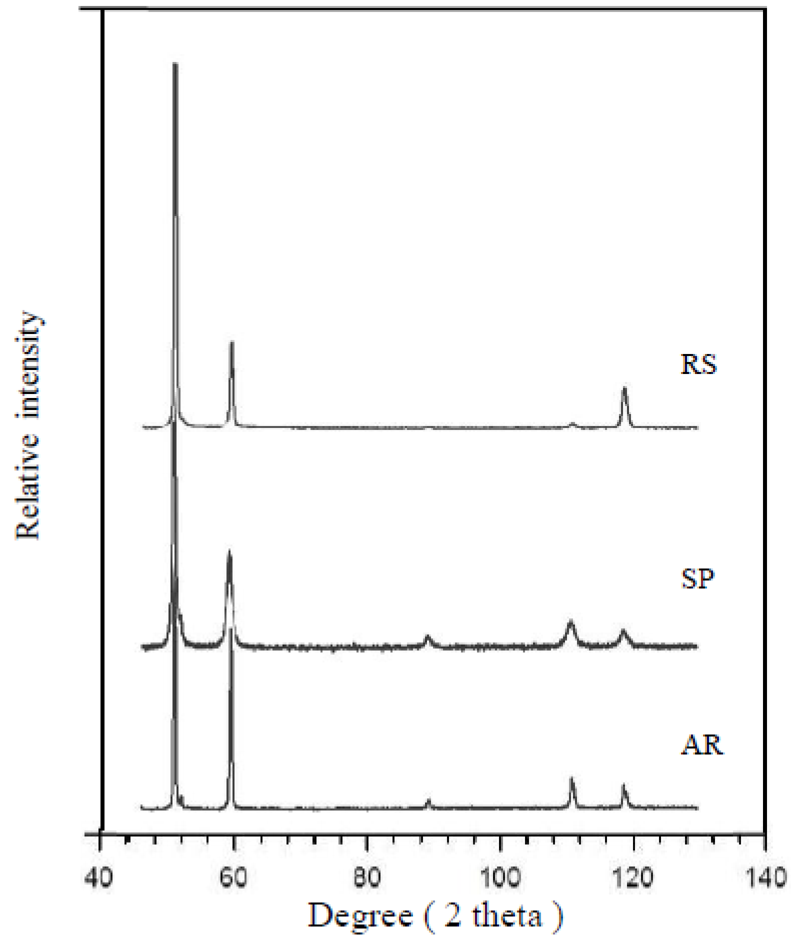

Figure 4.6, XRD spectra of the AR, RS and 0.28 mmA SP 316L stainless steel

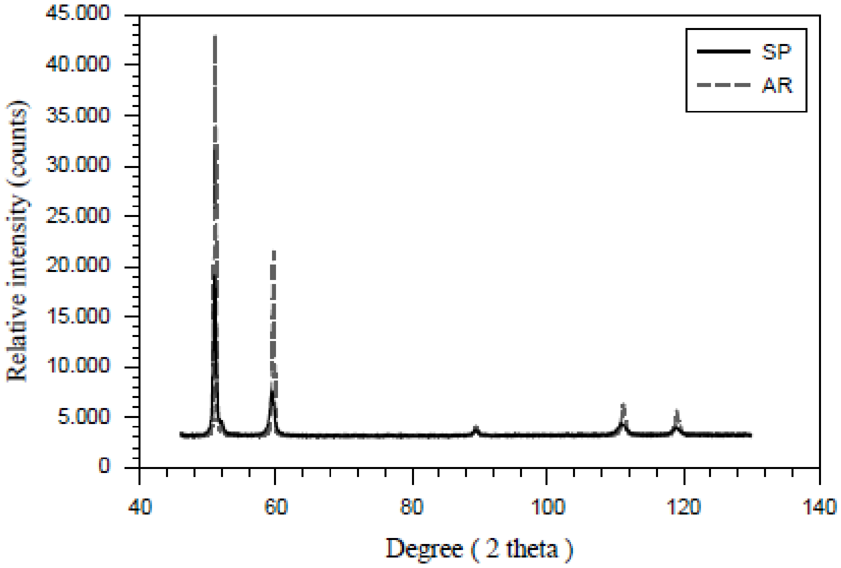

Figure 4.7, XRD spectra of the AR and SP 316L stainless steel

4.3 Shot peening

4.3.1 Mechanical properties

The microhardness depth-profiles of the SP 316L-samples are shown in Figure 4.8. Increasing the shot size resulted in a clear surface strengthening and a thicker hard layer (Figure 4.8a). SP at 200% coverage led to an increased surface microhardness as shown in Figure 4.8b. Figure 4.8c explains that the Almen intensity has significant effect on the microhardness by using the same shot size. However, the micro-hardness of the surface layer after peening of all conditions are higher than that of the reference (RE) specimen by about 220-380 HV at a depth of 200 µm. The grains refinement and the dislocation density in the top outer layer arise from shot peening, as shown in Figure 4.9, gives rise to the hardness of the surface layer [28, 159]. Figure 4.10 compares surface residual stresses for the shot peened samples at different parameters. In general, increasing peening intensity, coverage or shot size led to the higher surface compressive residual stress. Consequently, the largest compressive surface stresses were achieved by using the largest shot (850 µm) and the highest intensity (0.28 mmA) of SP. Decreasing the shot size leads to a lower surface stresses as shown in Figure 4.10a. The maximum compressive stresses reached about 980 MPa after 200% coverage and high peening intensity (0.28 mmA), Figure 4.10b. Indeed, the results indicated that the shot size, peening intensity and peening coverage have been effective parameters in work hardening, the effect of this treatment can be observed up to the depth of 500 µm, as shown in Figure 4.10. A significant influence of shot size is revealed by reference [160]. It’s reported that increasing shots diameter increases the depth of work hardened layer and the effect saturates at a limiting diameter. With the same shot size, increasing intensity means a higher impact speed. Because of the increased kinetic energy, the degree of plastic deformation and its penetration in the sample is significantly increased. A much larger compression zone with higher subsurface compressive stresses is therefore induced. The higher level of plastic strain can be obtained by increasing coverage more and more [161]. This can be interpreted as the motivation to move from conventional to severe SP in order to produce grain refinement. The coverage effect on residual stresses can be related to the cyclic behavior of the peened material. Peening coverage is a parameter related to the number of shots that impinge upon the surface during the duration of SP. The shots arrive at different times and the impact force from shots striking the same point or slightly different location leads to cyclically loading. The surface residual stresses were formed during the impact of the ceramic shots with the surface. Since the impacting loads were sufficient to achieve the plastic regime of the target material, the residual stresses were developed at the surface. The formation of residual stresses on AISI 316L after SP is reported in reference [162]. In addition, the increasing in the surface hardness due to presence the residual stresses on the surface layer of metallic materials has been demonstrated in Refs. [163-164]. Since most metal failures, e.g. fatigue cracking and fracture are initiated at the surface, the increase of hardness and compressive residual stresses at the surface layer of samples by SP is considerably beneficial to retard or sometimes prevents fatigue cracking and consequently enhance the service lifetime of materials [165-166].

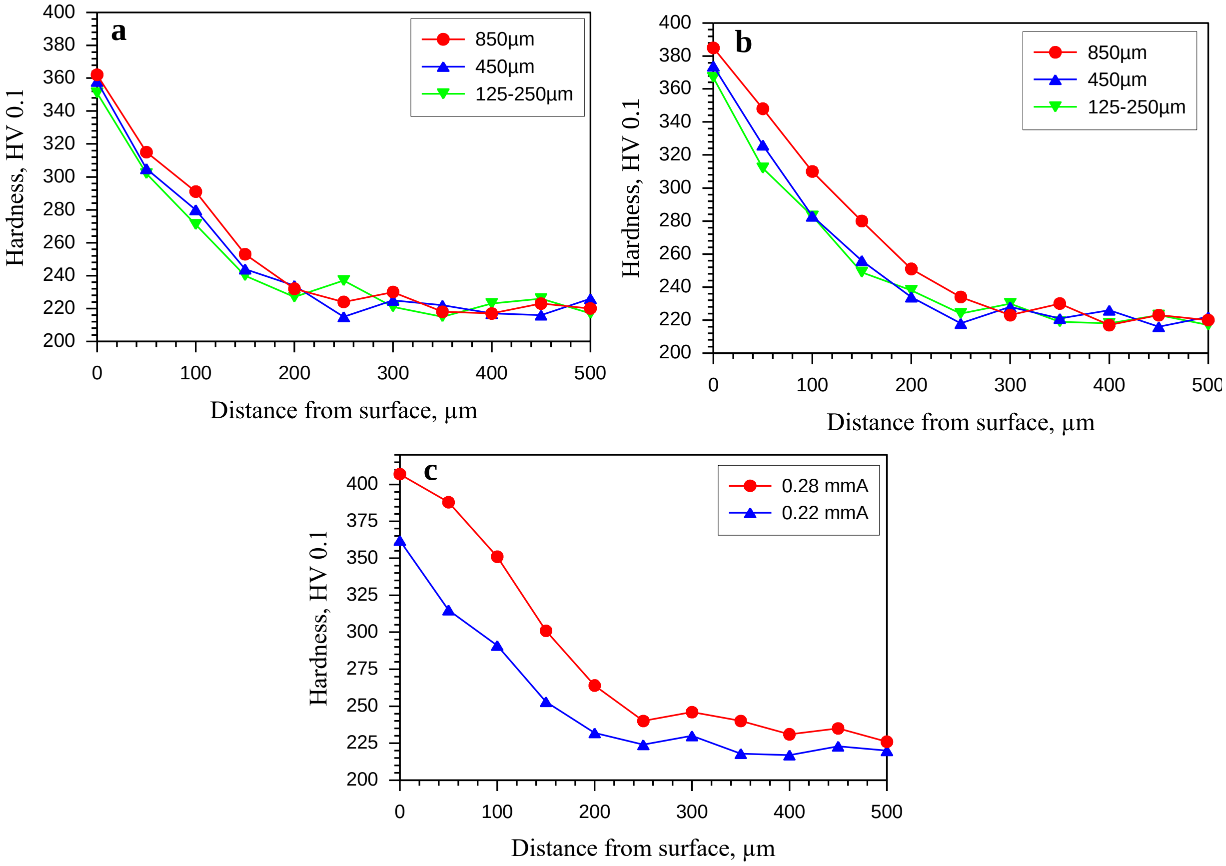

Figure 4.8, Microhardness-depth distributions, a) effect of shots size at 0.22mmA and 100% coverage, b) effect of shot size at 0.22 mmA and 200% coverage, c) effect Almen intensity at 100% coverage

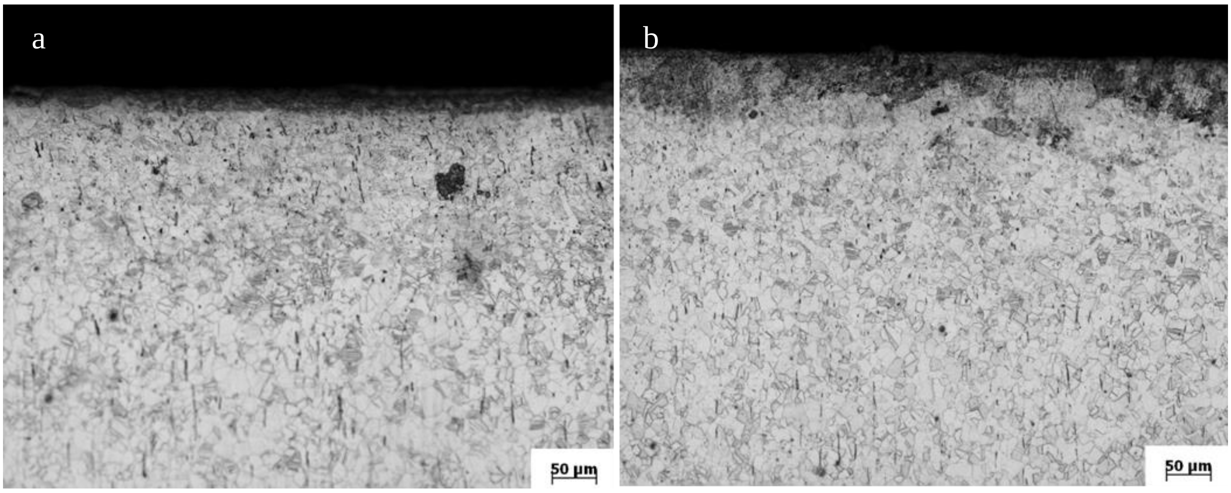

Figure 4.9, Cross-section of SP samples showing modified surface layer at two Almen intensity a) 0.22 mmA and b) 0.28 mmA

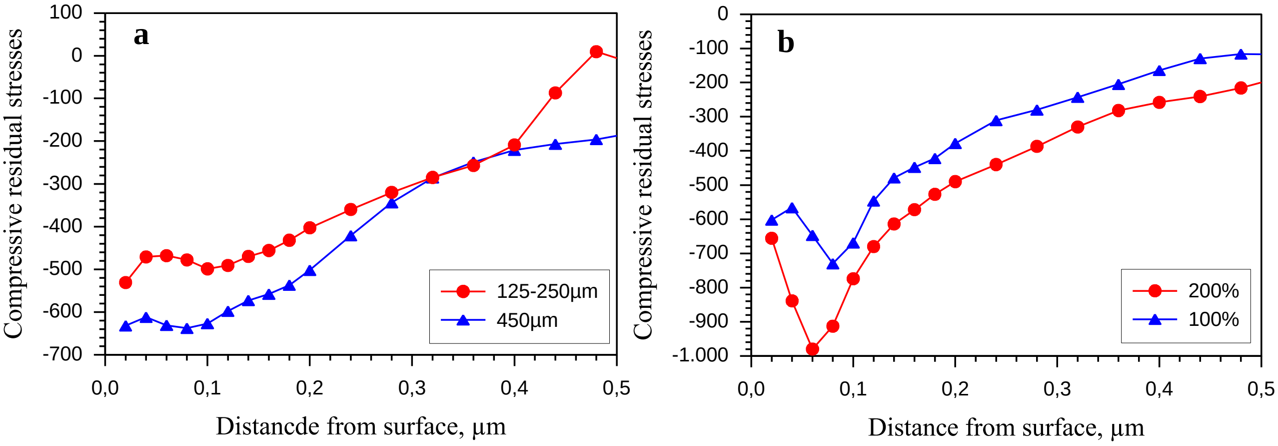

Figure 4.10, compressive residual stress-depth distribution, a) effect of shot size at 0.22mmA and 100% coverage, b) effect of peening coverage at 0.28mmA

4.3.2 Surface structures and roughness

The surface topography of AISI 316L after SP with various processing parameters are presented in Figure 4.11. The reference surface (RE) is smooth and clear from scratches. Figure 4.11, show that decreasing the shot size will decrease the size of the peening dimple. That means an increased number of dimples per unit area. Therefore, uniformity and homogeneity of the surface increased as shot size increased. The fact that homogeneity of the surface increases after SP by using big shots is verified by surface roughness measurement results. As clear from the Table 4.2, the surface roughness parameters (R_a, R_{max} and R_z) decrease from (0.87, 8.55 and 4.91) to (0.57, 4.96 and 3.21) µm after using the small shots 125-250 µm and the large shots 850 µm respectively. Figures 4.12 represent the effect of coverage peening on the surface topography and the roughness at fixed Almen intensity (0.22mmA). The higher peening coverage led to more deformation of surface and generated irregular surface structure. A similar finding can be found in Figure 4.13 where more craters and higher roughness values were observed due to increasing the intensity of SP from 0.22 to 0.28mmA. The choice of peening parameters affects the resulting surface roughness. Using larger shot typically yields a lower roughness [167]. Analytical calculations based on Hertz theory [168] can be used to compare the indentation radius (r) and depth (D) at the same Almen intensity for two cases as indicated in Figure 3.14. The results showed that $r_2 > r_1$ and $D_2 < D_1$, where r_1 and r_2 are the indentation radii for cases 1 and 2, respectively, and D_1 and D_2 are the indentation depths for cases 1 and 2, respectively. Wagner et al. [169] reported that ultrasonic peening with 1.5 mm shots results in a lower surface roughness compared to the conventional SP with 0.35 mm shots. Barzoukas, et al. [170] reported that surface roughness decreases when using larger ceramic shot for a constant Almen intensity, as well as, the surface roughness can be increased by increasing the peening pressure under constant shot size.

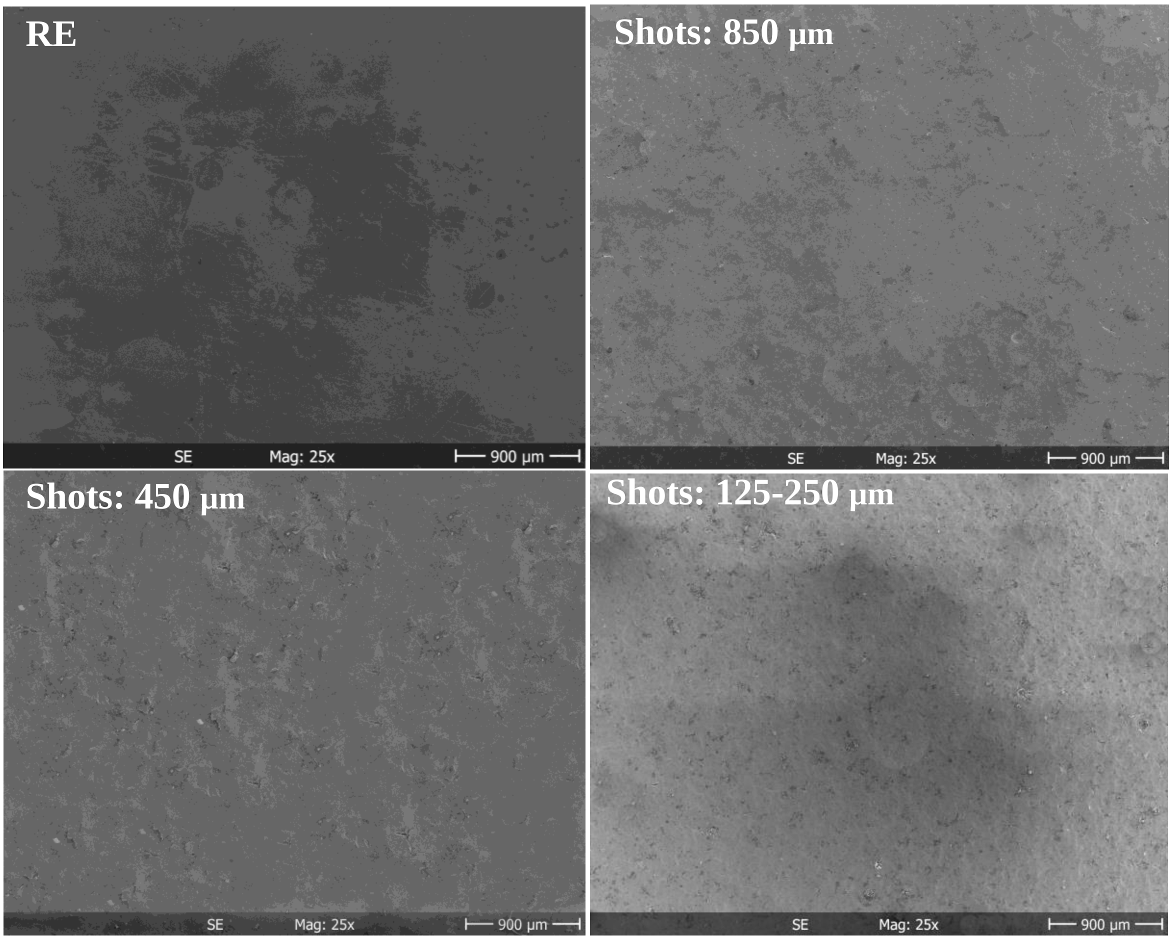

Figure 4.11, effect of the shot size at 0.22mmA on the surface topography

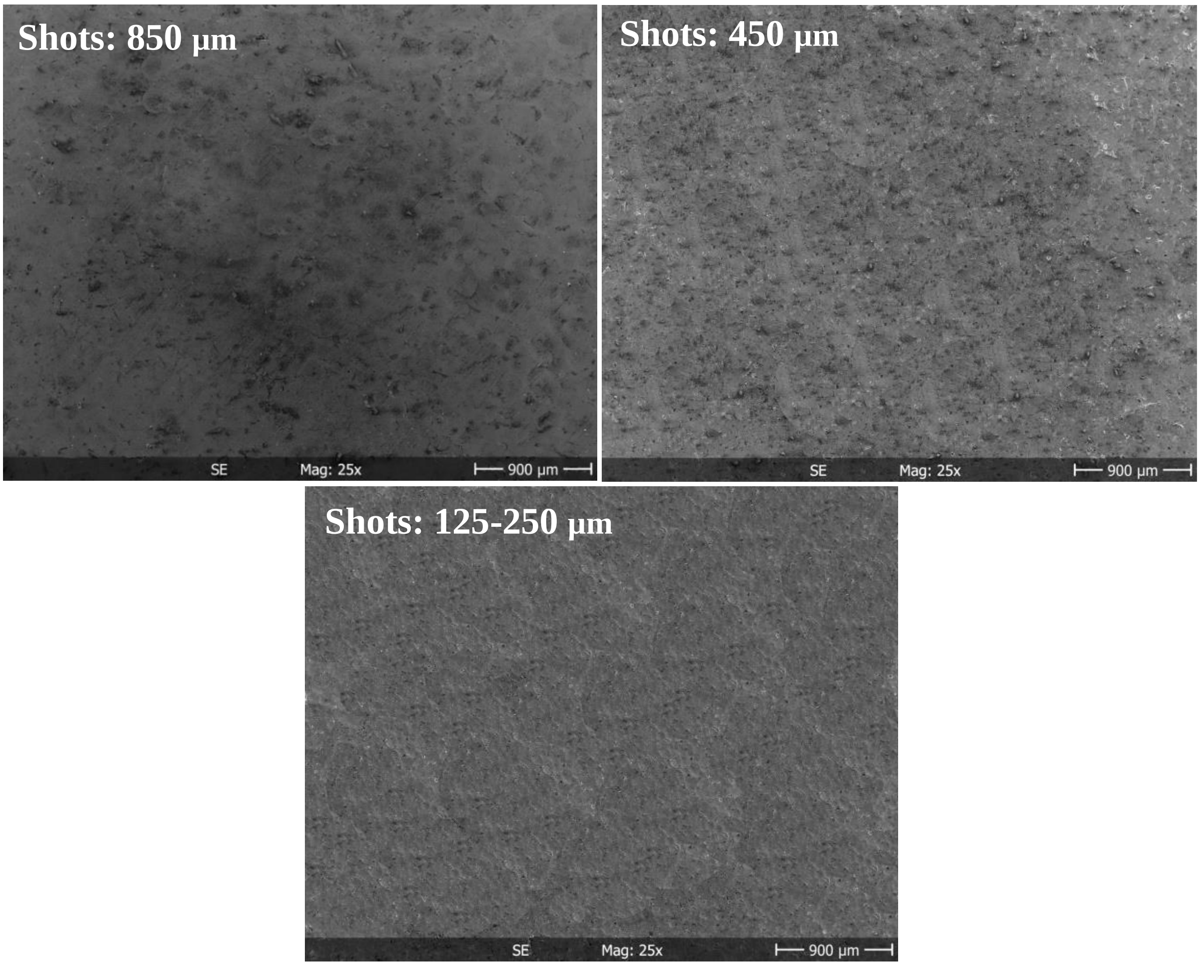

Figure 4.12, effect of the 200% peening coverage at 0.22mmA on the surface topography

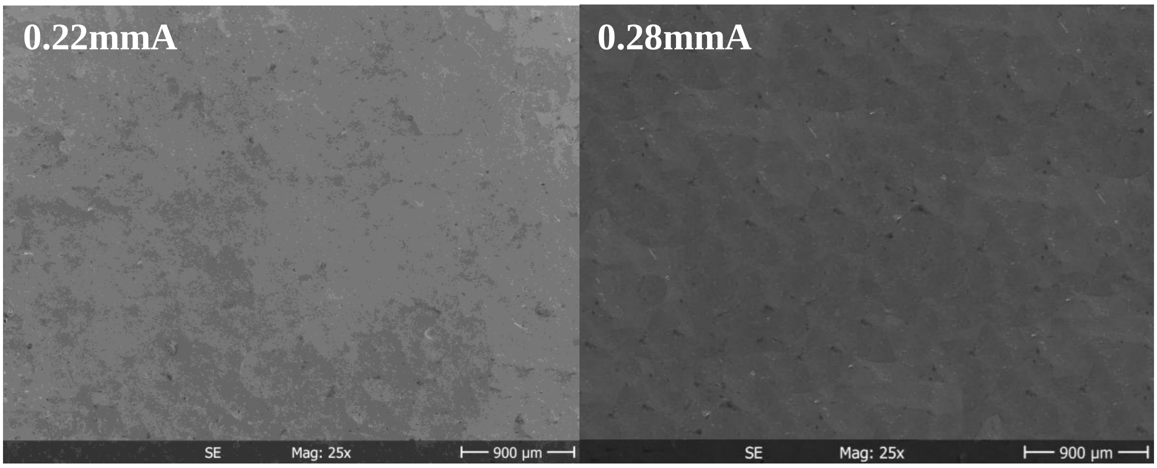

Figure 4.13, Effect of the Almen intensity on the surface topography

Table 4.2: Roughness parameters values

Almen intensity/ mmA		surface conditions	Rmax/ µm	Ra/µm	Rz/ µm
0.22	100%	RE	0.55	0.05	0.44
		SP, 850 µm	4.96	0.57	3.21
		SP, 450 µm	7.20	0.74	4.20
		SP, 125-250 µm	8.55	0.87	4.91
	200%	SP at 850 µm	7.10	0.65	3.52
		SP at 450 µm	10.41	1.29	6.45
		SP at 125-250 µm	13.18	1.32	8.43
0.28		SP at 850 µm	5.13	0.77	3.85
		SP at 850 µm + HA coating	9.33	1.34	8.45

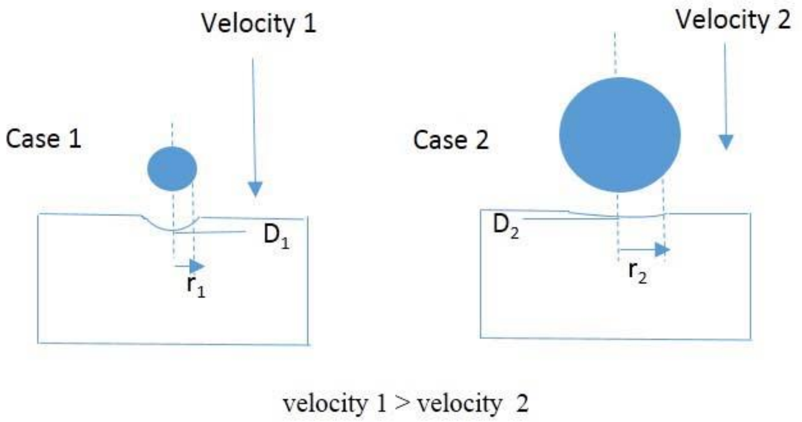

Figure 4.14, Different combinations of impact velocity and shot diameter can yield the same Almen intensity, but resulting roughness is not the same. Larger shots with lower velocity generally yields a lower roughness

4.4 Coating characterization

Figure 4.15a shows a SEM micrograph of the as chemical deposited HA coating. The HA coatings exhibited a needle-like micro porous morphology. The obtained coatings were homogeneous, dense and crack-free. Sintering at 500 and 600°C (Figures 4.15 b and c) fused the HA needle particles and increased the grain size of the HA coating significantly, however the coating’s fusion is not as good as the materials sintered at 700°C (Figure 4.15d). Sintering at 700°C led to a denser, fused and aggregated HA with agglomerated particles. This can be

clearly seen in the highly magnified SEM micrographs in Figure 4.16. Figure 4.16b obvious that the grains particles of coating at 700°C sintering were bigger and denser than sintering at 500°C, Figure 4.16a. The SEM graph in Figure 4.17a presents a cross-section of HA-coated sample before sintering. The graph revealed a uniform layer between the coating and the substrate with a visible separation at the interface. This could be an indication of poor adhesion due to insufficient mechanical interlocking. M. J. Filiaggi el al.[171] reported that existence of a weak link in the metal/ceramic interface still the major problems which requiring further heat treatment to improve HA/substrate bonding through enhanced diffusion of coating/ metal interface. Sintering at 700°C (Figure 4.17b) led to better integrity of HA coating that resulted in a good packing and incorporation with the substrate. The separation at the interface disappeared after sintering at 700°C due to the fused and incorporated HA coating with the substrate, showing that the mismatch in thermal expansion between the coating and substrate during heating and cooling was well tolerated. The thickness of the formed HA coating layer after single deposition process was about 4 to 5µm as indicated in SEM micrograph in Figure 4.18. Repeating the deposition process for three times increased the thickness of the coated layer to about 12µm. Therefore, the repeating of the deposition process more than one time was useful to get a dense coating and ensure the total coverage of the substrate surface. The thickness of the HA coating was reduced from 12µm to 6-8µm after sintering at 700°C. Thin HA coating is more desirable in order to avoid crack formation that arises from the difference in thermal expansion coefficients of HA coating and substrate during heating and cooling, which leads to degradation of mechanical properties of the alloy [172]. J. Ma et al.[173] reported that the HA coating became denser as the temperature increased (from 1000 to 1300°C). However, a high
temperature will result in the decomposition of HA into undesirable α- and β-$Ca_3(PO_4)_2$ with reduced biocompatibility [174] and increased in vitro dissolution [175]. Y. P. Lu et al. [176] stated that post heat treatment of plasma-sprayed HA coating at 650°C intensified their aggregation and hard aggregation occurred when HA coatings were repetitively post-heat treated. Moreover, the post-heat treated HA coatings exhibit an obviously better osteoblast response than the as-sprayed coatings.

The EDX spectra of the HA coating before and after sintering are shown in Figure 4.19. Figures 4.19 b and c refers to a deficiency of the substrate alloying elements in the outer layer of the coated surface after sintering at 500 and 700°C compared to the as-HA coated material (Figure 4.19a). Moreover, the intensity of the HA coating elements increased with increasing the sintering temperature. This could be explained by the presence of some micro- pores on the as HA-coated. The swelling and increasing of HA grains that aggregated within agglomerated particles due sintering (as shown in figure 4.16) led to a clear decrease of the pores and improved the surface coverage that probably hindered the penetrating X-rays to the substrate.

XRD studies of synthesized coating confirmed the formation of HA coexisting with CaP phase on the surface of the coating (Figure 4.20). The XRD spectra referred to the presence of the HA crystalline phase at the highest peak of $2\theta= 30°$, which confirm that HA was the dominant phase in the coating. Sintering at 500 and 700°C resulted in higher HA-peaks intensities of HA, with retained CaP, which refers to the improved apatite crystallinity.

Figure 4.21 shows the surface roughness profiles and the values of the maximum surface roughness (R_{max}) of HA-coated surfaces. Compared to the as HA-coated surface, increasing the sintering temperature from 500 to 700°C resulted in significantly rougher surfaces. The value of the maximum surface roughness R_{max} of as HA-coated surface increased from 4.93 to 12.21μm after sintering at 700°C. The increased surface roughness after sintering is related to the increase of the aggregated surface particles. Higher roughness implies exposure of more surface area for interaction with biomaterials. Hence, surface roughness is regarded as very important factor for implant tissue interaction that affects the biocompatibility in clinical use [177-179].

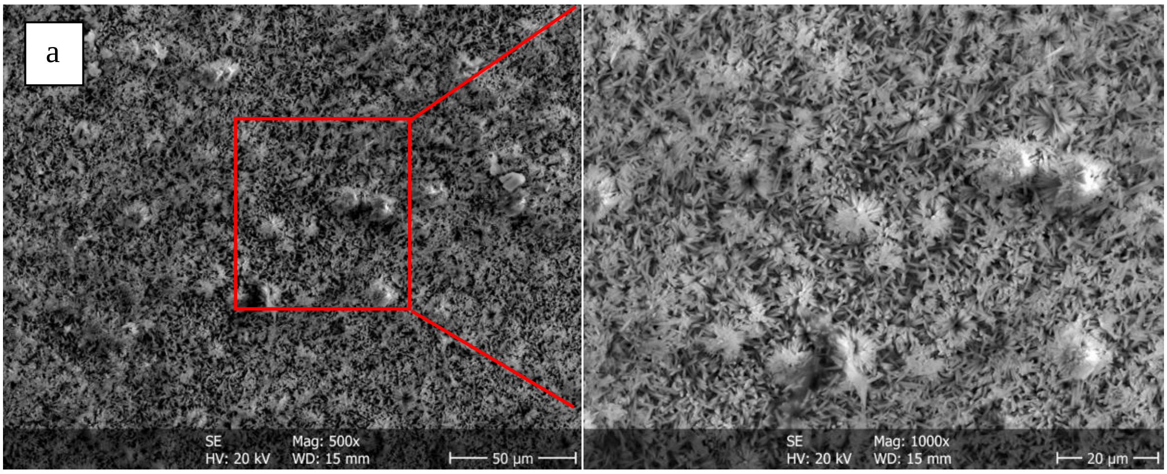

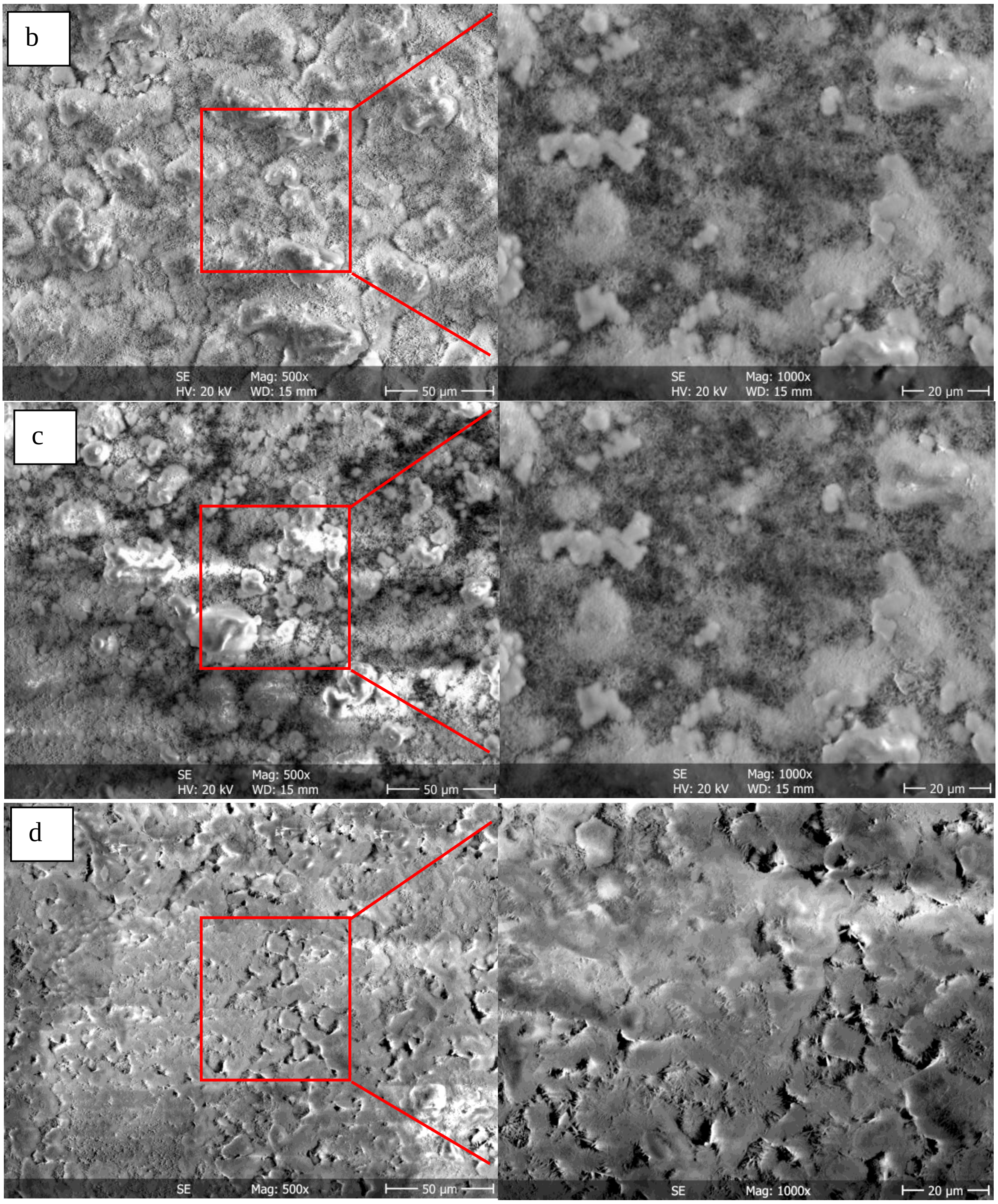

Figure 4.15, SEM images of (a) as HA coated surface, (b) HA-coated + 1 h at 500°C, (c) HA-coated + 1 h at 600°C and (d) HA-coated + 1 h at 700°C.

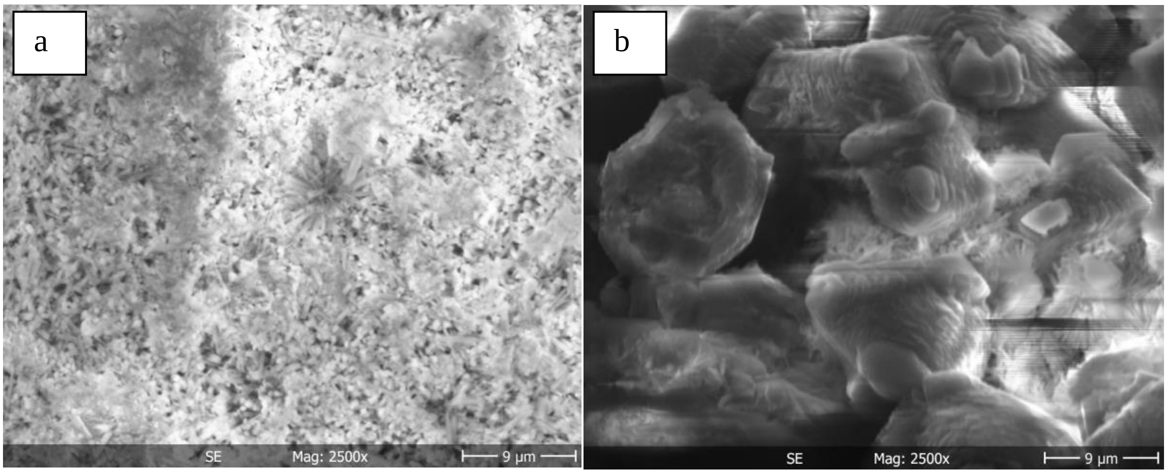

Figure 4.16, highly magnified SEM images of (a) HA- coated + 1 h at 500°C and (b) HA-coated + 1 h at 700°C

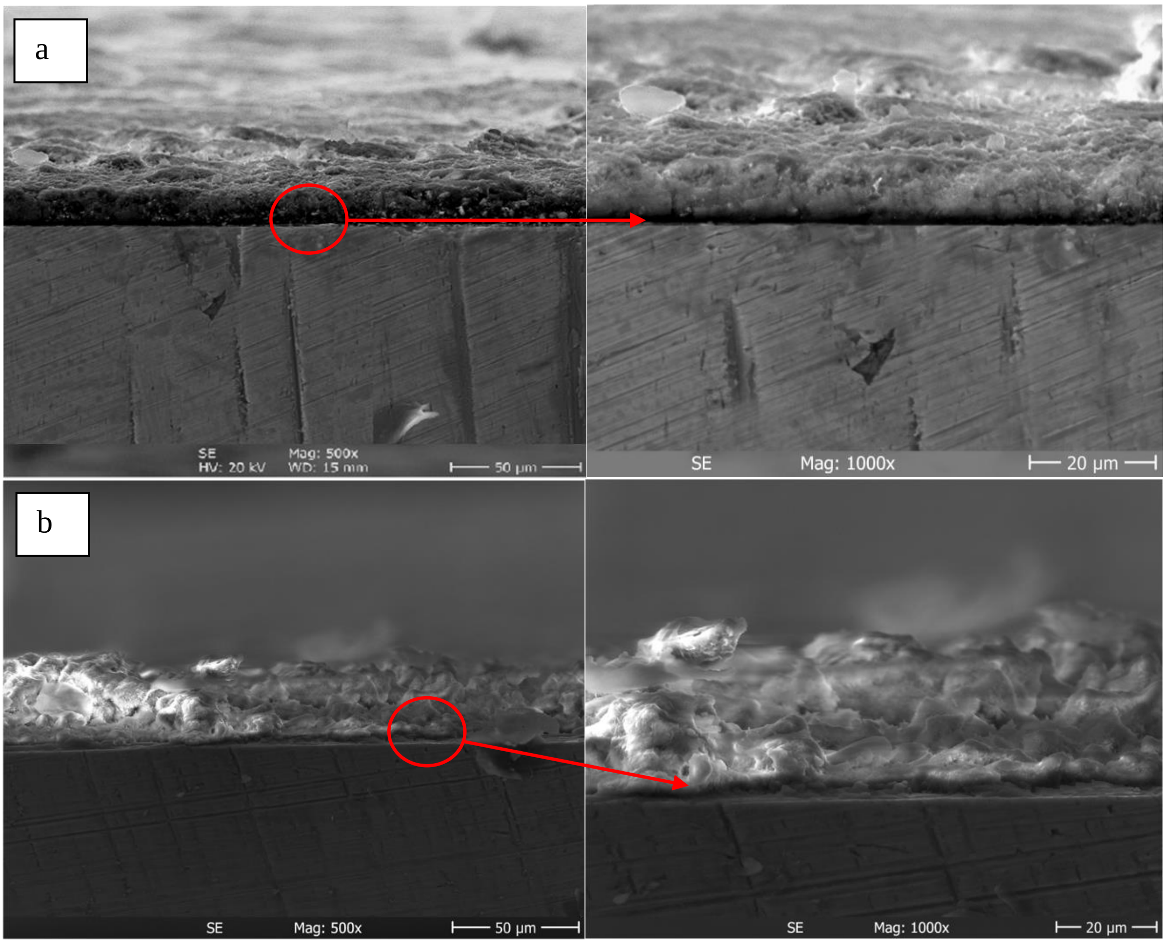

Figure 4.17, SEM micrographs of (a) as HA coated surface and (b) after Sintering at 700°C

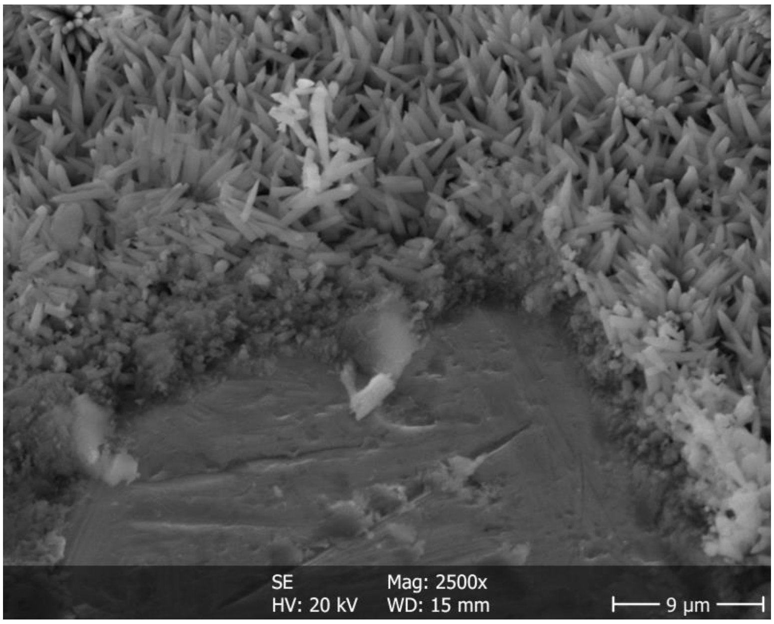

Figure 4.18, SEM micrographs of as HA coated surface for one-time coating

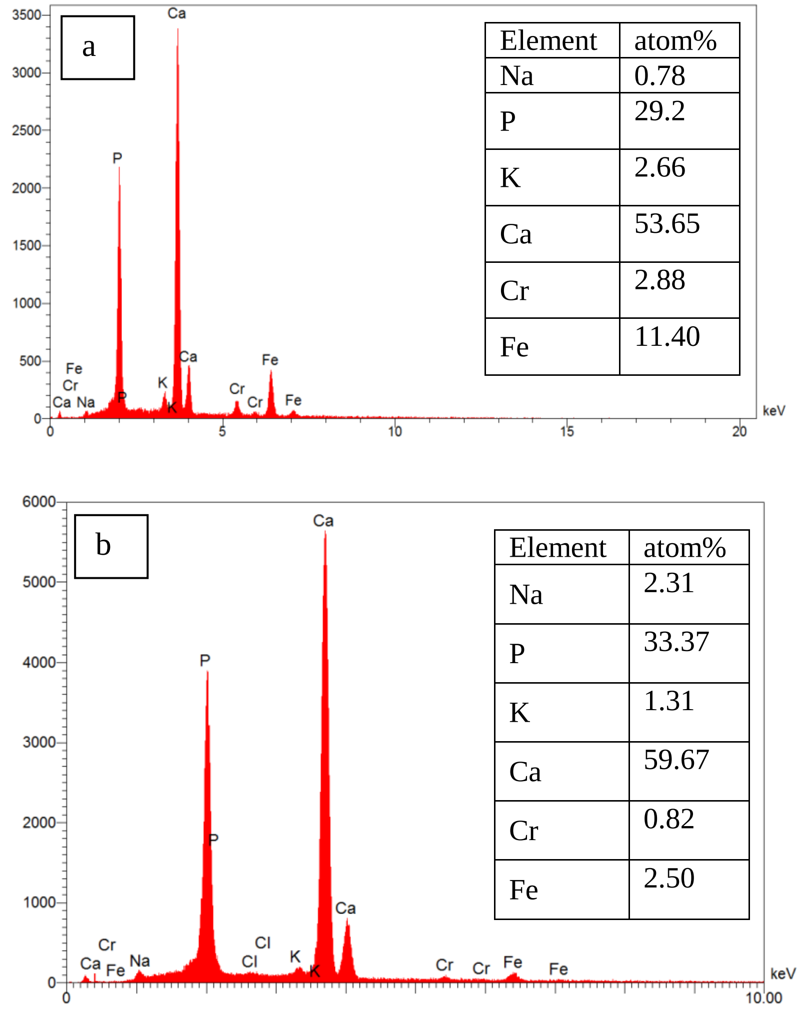

Element	atom%
Na	0.78
P	29.2
K	2.66
Ca	53.65
Cr	2.88
Fe	11.40

Element	atom%
Na	2.31
P	33.37
K	1.31
Ca	59.67
Cr	0.82
Fe	2.50

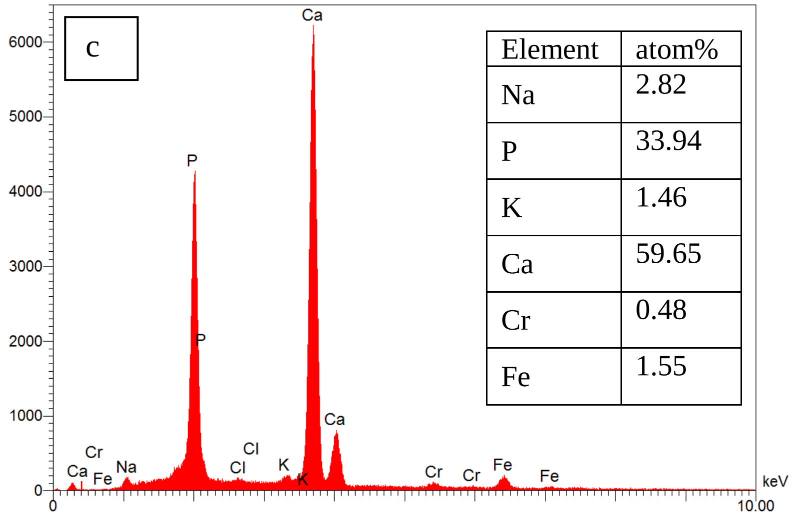

Element	atom%
Na	2.82
P	33.94
K	1.46
Ca	59.65
Cr	0.48
Fe	1.55

Figure 4.19, the EDX analysis of (a) as HA coated surface, (b) HA-coated + 1 h at 500°C, and (c) HA-coated + 1 h at 700°C

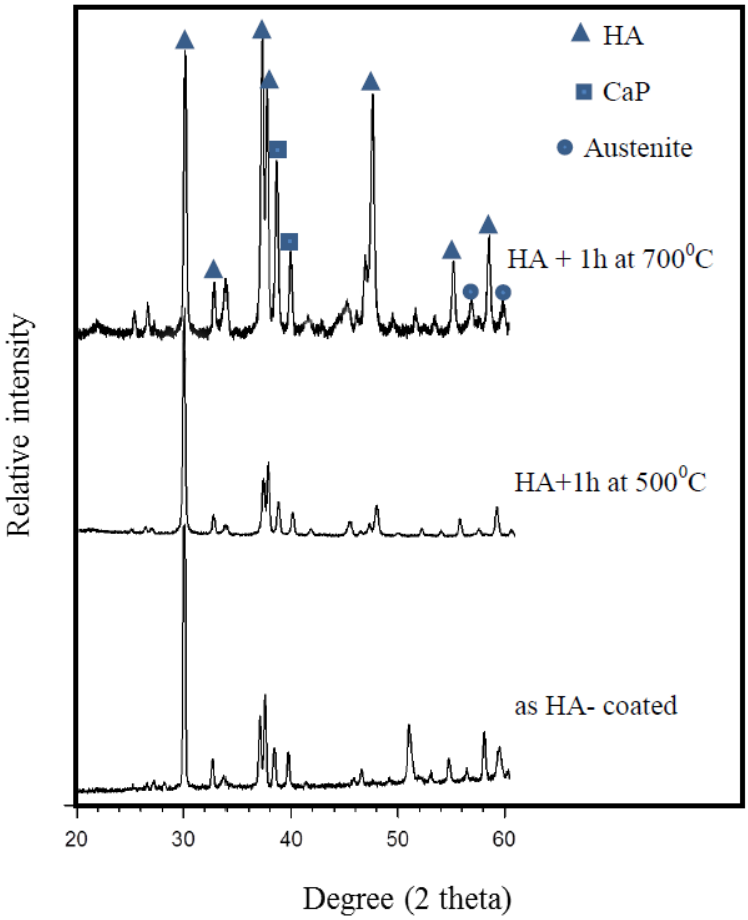

Figure 4.20, XRD patterns of as HA coated surface, HA-coated + 1 h at 500°C, and HA-coated + 1 h at 700°C

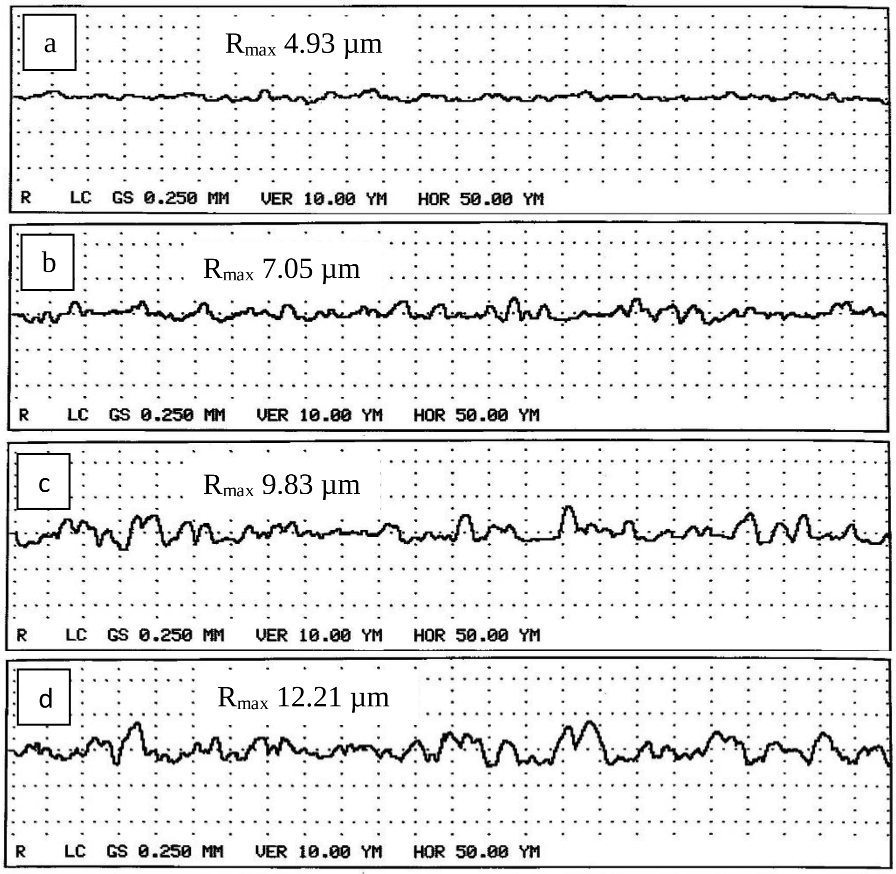

Figure 4.21, surface rroughness profiles and values of (a) as HA coated surface, (b) HA-coated + 1 h at 500°C, (c) HA-coated + 1 h at 600°C and (d) HA-coated + 1 h at 700°C

4.4.1 Coating/substrate adhesion strength

Table 4.3 lists the values of the adhesive strength of the as HA-coated and sintered samples. The as-HA coated material exhibited an adhesive strength of 8.3 MP_a. Sintering of the HA-coated samples at 500, 600 and 700°C increased the adhesive strength to 12.3, 16.8 and 19.8 MP_a, respectively.

The relatively low adhesive strength of the as HA coated material compared to the sintered-samples is related to the presence of a separation at the coating/substrate interface of the as HA-coated samples. Sintering led to an incorporation and diffusion of the coating elements in the substrate which increased the coating/substrate interlocking [180]. In addition, the increase in the adhesive strength after sintering is related to the lower pores and more fused coating/substrate interface.

The adhesion strength of coating/substrate depends on the chemical bonding and mechanical interlocking [181-183]. The chemical bonding is enhanced by sintering. Whereas, the mechanical interlocking could be improved by increasing the surface roughness of the substrate by pretreatments such as shot peening or etching. Yan, et al. [184] documented that heat treatment significantly affects coatings. They have noticed that coatings show little variation in the position and intensity of OH and PO_4 bands along the thickness direction of coatings, which indicates that the heat treatment promotes homogeneity and phase transformation to HA in the entire layer of coating.

Y. C. Yang, B. Y. Chou [185] reported that the bond strength between plasma sprayed HA coating and alumina substrate increased with the increasing temperature of post heat-treatment. The authors contributed the increased bond strength to various reasons. Among these reasons are (a) the stronger cohesive strength of HA coating due to the initial sintering, (b) chemical bonding was formed between the HA coating and bond coat, bond coat and substrate by the inter-diffusion, and (c) the porcelain bond coat became denser and increase its strength after heat-treatment.

Table 4.3: Adhesive strength of various conditions

Conditions	Bond strength/ MP_a
HA coated	8.3
HA-coated + 1 h at 500°C	12.2
HA-coated + 1 h at 600°C	16.8
HA-coated + 1 h at 700°C	19.8

4.4.2 Corrosion behavior

The potentiodynamic polarization curves of the un-coated and HA-coated samples are shown in Figure 4.22 and Table 4.4. The results revealed a marked improvement of the corrosion resistance of the HA-coated material due to the better barrier that protect the substrate. The polarization curves of as HA-coated and sintered samples are presented in Figure 4.23. The values of the electrochemical characteristics, which were calculated by Tafel extrapolation method, are illustrated in Table 4.4. The HA-coated material exhibited a more noble value of corrosion potential (E_{corr}) of -183mV. Increasing the sintering temperature after HA coating led to a clear drop of the corrosion current density (I_{corr}) compared to only HA-coated material. The lowest value of I_{corr} was achieved after sintering at 700°C. I_{corr} of the as HA-coated material decreased from 0.405 to 0.0943 $\mu A.cm^{-2}$ after sintering at 700°C.Accordingly, the corrosion rate of the HA-coated material decreased from 0.138 to 0.032 mpy after sintering at 700°C. This represents a drastic drop of about 400% in the corrosion rate after sintering at 700°C.The corrosion resistance of the materials sintered at 500 and 600°C is better than that of the as HA-coated material. However, the values of corrosion rates of the materials sintered at 500 and 600°C were higher than the corrosion rate observed after sintering at 700°C. This could be ascribed by the un-complete fusion of HA coating resulting after sintering at 500 and 600°C (Figures 4.15 b and c).

The micro-pores at the surface of the HA-coated samples conducted paths between the Ringer's solution and substrate. These paths facilitate the permeation of water and Cl^- into the coating and the subsequent electrochemical reactions at the coating/substrate interface. This explains the lower corrosion resistance of the only as HA-coated material. The corrosion of HA coatings that include pores was described by Zhang et al [186]. The produced hydrogen ions (H^+) at the coating/substrate interface lowers the local pH at coating/substrate interface that accelerates the dissolution of HA according as following:

$$Ca_{10}(PO_4)_6(OH)_2 + 2H^+ \rightarrow 10Ca^{2+} + 6PO_4^{3-} + H_2O$$

Sintering resulted in fused, well-dispersed structure and good adherence HA coating that acts as insulation that efficiently prevent the direct contact between the electrons and ions Ringer's solution and the substrate, which led to the pronounced improvement of the corrosion resistance. Moreover, the thinner HA coating after sintering contributes to an improved corrosion resistance. B. Aksakal etal.[187] reported that the HA coating thickness is an effective parameter on both adhesion and corrosion resistance, increasing coating thickness led to a lower corrosion resistance. In addition, the thick coatings often exhibited porosity that weakened the interfacial strength and provided an easy fracture path for adhesion failure, thus lead to a lower corrosion resistance [188].

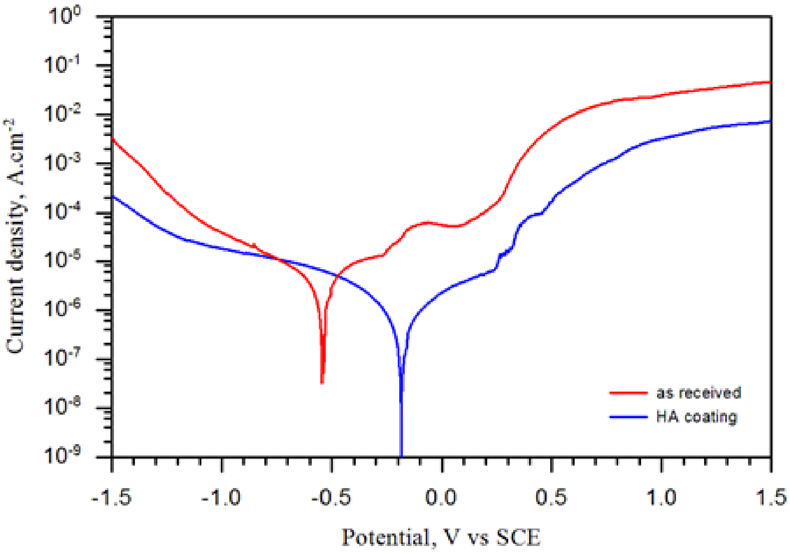

Figure 4.22, potentiodynamic polarization curves of as HA coating comparison with uncoated AISI 316 L in Ringer's solution at 37±1°C

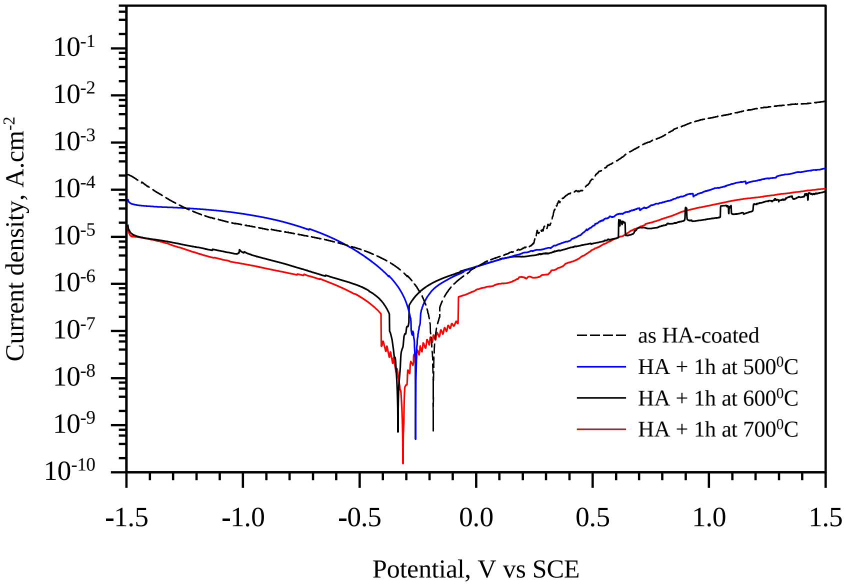

Figure 4.23, potentiodynamic polarization curves of various conditions tested in Ringer's solution at 37±1°C

Table 4.4: Electrochemical characteristics of various conditions

Conditions	Corrosion current density, I_{corr}, µA.cm^{-2}	Corrosion potential E_{corr}, mv	Corrosion rate, mpy
Uncoated AISI 316L	4.2	- 541	0.89
HA coated	0.405	-183	0.138
HA-coated + 1 h at 500°C	0.374	-259	0.127
HA-coated + 1 h at 600°C	0.196	-335	0.066
HA-coated + 1 h at 700°C	0.0943	-313	0.032

4.5 Wettability

Figure 4.24 shows the initial contact angle (by using Ringer solution) of shot peened samples at various processing conditions. The SP markedly enhances the surface wettability as indicated by reduction of droplet contact angles in all the treated samples. The droplet contact angle of the RE sample is ±69.3◦, Figure 4.24; indicating its less hydrophilic property due to the polishing treatment. Since the roughness regards effective parameter to increase wettability of surface [189] therefore, the contact angle decreased gradually from ±51.2◦ to ±31.2◦ with increased the surface roughness R_a from 0.57µm to 0.87µm respectively. The shot peened sample at 0.28mmA coated with HA registered less contact angle (±22.6^o) with respect to the reference and the other shot peened materials. The HA coated samples displayed a very low contact angles due to the surface irregularities porous morphologies [190], as it shown in Figure 4.15 (a). Similar results have been observed in the reference [67]. It's reported that the contact angle was significantly lower in the HA-coated samples compared to the non-coated titanium samples. F. Rupp et al. [66] stated that wettability is affected by surface characteristics, such as surface chemistry and surface topography. The physical characteristics of the substrate surface (e.g., roughness, microcavities, pores, coatings, adsorbed layers, prior thermal or ionic cleaning etc.) can alter the spreading and wetting behaviors, often dramatically. According to Figure 4.11, the increase in surface roughness is the main reason for the reduced of contact angle. Generally, an average roughness less than 100 nm yields fair repeatability of measured contact angles, whereas large roughness values yield significant dispersion in the measured angles [191]. The surface energy of the solid is another factor affects the ability of a liquid to wet the surface of a solid. The outer atoms are not equally attracted to each other as in the inner layer of atoms. The energy is greatest on the outermost atomic layer because the unsaturated bonds generate surface energies. When a liquid is placed on a lower-energy surface metal, the contact angle will be higher as compared with a higher-energy surface metal (greater surface roughness) [192]. Surface parameters such as roughness and wettability affect the interaction of the material with the surrounding environment. The rough and hydrophilic surfaces are appropriate for the bone-cells adhesion and the successive osseointegration of implants [40, 193]. Bagherifard et al. [194] indicated that the surface topography and grain size can affect cell behavior in the different ways. They concluded that the grain refinement and dissimilar densities of the surface defect play an important role in promoting cell adhesion and activities. The interaction between the outermost surface of a biomaterial and its environment was a highly dynamic process, in which direct and indirect cell adhesions induced by protein previously adsorbed onto the surface were two competing processes. Direct cell adhesion, means attaching cells directly on the surface while the indirect cell adhesion means culturing an intermediate layer, like protein, between surface and cells. The attachment of molecules with different protein are expected to modify the surface of the implant and result in improvement of cell adhesion when placed into its physiological environment. [195]. In general, the direct cell adhesion tends to occur efficiently on hydrophilic surfaces but inefficiently on hydrophobic surfaces, whereas indirect cell adhesion dominates over smooth and hydrophobic surfaces [196].

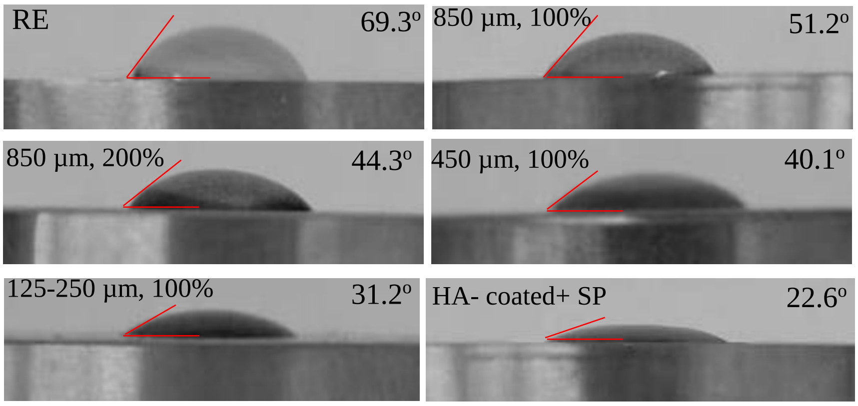

Figure 4.24, effect of different surface conditions on water droplet contact angle

4.6 Corrosion behavior of deformed 316Ti SS

Figure 4.25 shows the potentiodynamic polarization curves of non-deformed (φ= 0) and deformed specimens. It is obvious that increasing the deformation degree led to a clear shift in the corrosion potential (E_{corr}) to the negative direction, and an increase in the anodic current density (I_{corr}). Table 4.5 represents the electrochemical characteristics of the different tested conditions. The corrosion current density I_{corr} of the non-deformed material (φ= 0) increased from 1128 to 9980 $nA.cm^{-2}$ after deformation at φ= 2.25. Correspondingly, the corrosion rate of the nondeformed material (φ= 0) increased from 0.302 to 3.09 mpy after deformation at φ= 2.25. The increased electrochemical activity by increasing the deformation degree might be related to the increased martensite content due to deformation. The martensite phase could act as an anode in an electrochemical cell and thereby prone to selective dissolution. Chloride ions are adsorbed preferentially on martensite locations and then react with the surface film. This leads to destruction of the surface film and delays its restoration. Metallographic observations (Figure 4.26) of samples surfaces after electrochemical tests showed numerous corrosion pits. Generally, corrosion resistance of stainless steels is achieved by dissolving a sufficient amount of chromium in iron to produce a coherent, adherent, insulating and regenerating chromium oxide protective film (Cr_2O_3) on the surface. This passive film of chromium oxide formed in air at room temperature is only about 1–2 nm. Pitting corrosion is the result of the local destruction of the passive film and subsequent corrosion of the steel underneath this layer. The micrographs in Figure 4.25 indicated that the pit initiation frequency increased with the deformation degree. The pits formation is influenced by many factors such as martensite content, dislocations density and internal stresses [197]. A. Barbucci et al. [198] has related the pit initiation to the passive film stability, which is influenced by cold deformation. The increased number of pits by increased cold work suggests a much higher defective oxide film in deformed material. The surface defects may lead to a selective Fe dissolution and diminish the protection of the substrate by the film, i.e., they increase its apparent conductivity. Previous studies reported that the equilibrium ferrite/austenite structures could promote galvanic corrosion with dissolution of ferrite in open circuit conditions [199]. Moreover, it is reported that the inclusions are likely to affect the pitting initiation [200].

The effect of HA coating on the corrosion behaviour, in terms of potentiodynamic polarization, is illustrated in Figure 4.27. The Figure shows the potentiodynamic polarization curves of the nondeformed (φ= 0) + HA coating and deformed (φ= 2.25) + HA coating. It is clear that HA coating resulted in a significant reduction of the corrosion current density. The corrosion potential E_{corr} shows a relative shift to the positive direction. More interestingly, the cathodic and anodic current of the deformed material (φ= 2.25) + HA coating were lower than those of the nondeformed material (φ= 0) + HA coating. Correspondingly, the values of I_{corr} and corrosion rate calculated based on Tafel extrapolation, of the deformed (φ= 2.25) + HA coating, were relatively lower than those of the non-deformed (φ= 0) + HA coating (Table 4.5). Introducing HA coating on the surface of the deformed material (φ= 2.25) led to a reduction of the corrosion current density and corrosion rate from 9980 nA.cm-2 and 3.09 mpy to 328 nA.cm-2 and 0.167 mpy, respectively. The progressive enhancement of the corrosion resistance after HA coating is related to the fact that HA is a non-interactive ceramic material. Accordingly, HA coating forms a barrier that prevents ions release from the substrate hence provide a good protection against corrosive environment.

The coating thickness is an effective important factor influencing adhesion and corrosion resistance. B. Aksakal et al. [187] found that adhesion and corrosion resistance decreased with increasing coating thickness on 316L SS. The authors observed an increased surface cracks after thicker HA coatings. The number of cracks reached a significant level when the thickness was more than 40 µm and the highest corrosion susceptibility was found on 72 µm HA-coated 316L SS. Such cracks may lead to loosening of the implants. Moreover, the bonding strength of thicker HA coatings was lower than that of thinner ones. Bonding strength of HA coatings decreased with increasing coating thickness. After the corrosion tests, it was observed that the bonding strength was reduced. S. Sonmenz et al. [201] stated that the micro-scale HA-coated Mg substrates were more corrosion resistant than the nano-scale HA-coated substrates. Thicker coatings often exhibited porosity that weakened the interfacial strength and provided an easy path for adhesion failure. The coating with higher crystallinity and fewer defects may be preferentially considered. The nucleation, growth of crystals onto the substrate, dissolution and precipitation rates of HA coatings are critically dependent on the crystal structure developed in the coatings. HA coatings with higher crystallinity yielded a decreased dissolution rate [202] and higher rates of cell proliferation [203]. Darimont et al. [204] concluded that implants in trabecular and cancellous bone require coatings with a very high crystallinity. Another study by W. Xue et al. [205] deduced that the HA coating with high crystallinity showed the lower dissolution compared to the low crystallinity coating. They found that, after three months' implantation, the high crystallinity coating showed the higher shear strength and remained integrated. Whereas the separation of the coating fragments was clearly observed in the low crystallinity coating. In brief, the high crystalline HA coating is suitable for long-term implantation and the low crystalline coating has superiority in promoting faster initial bone fixation [206].

The formation of the passive film was found to occur with wider potential range for both HA coated materials in comparison with the uncoated materials. This indicates that the passivation through the HA coating leads to a significant enhancement of the passivation properties of the surface oxide film [207]. The passive film prevents the dissolution of the substrate into the electrolyte.

These observations confirm the marked enhancement of the passive film and corrosion resistance after HA coating. According to the current results, the significant improvement of the corrosion resistance of the deformed 316Ti SS after HA coating together with the high mechanical properties offer promising advantages of the studied material for clinical applications.

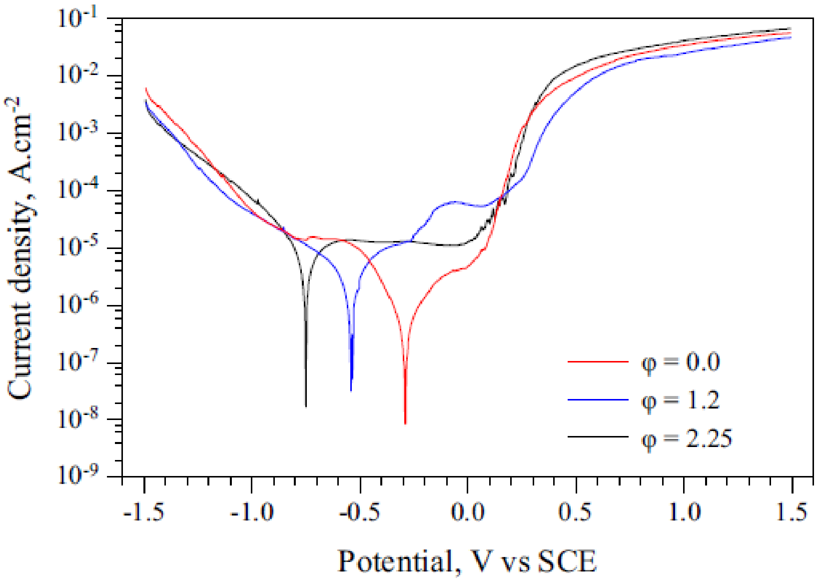

Figure 4.25, potentiodynamic polarization curves of the non-deformed (φ = 0) and deformed (φ = 1.2 and φ = 2.25) SS 316Ti in Ringer's solution at 37°C

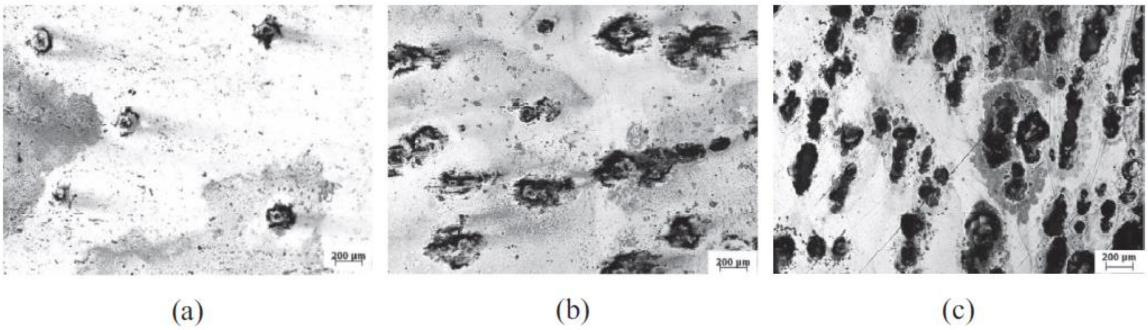

(a) (b) (c)

Figure 4.26, optical micrographs revealing corrosion pits formation after potentiodynamic polarization of uncoated SS 316Ti (a) φ = 0, (b) φ = 1.2 and (c) φ = 2.25

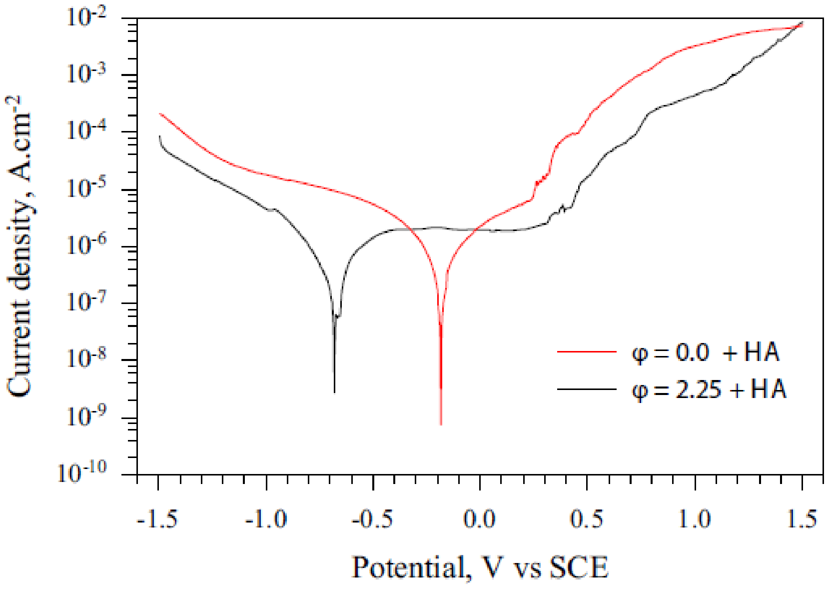

Figure 4.27, potentiodynamic polarization curves of the HA-coated SS 316Ti in Ringer's solution at 37°C.

Table 4.5: Results of the electrochemical tests of SS 316Ti cold rolled at different deformation degrees

Deformation degree	Corrosion current density, I_{corr} (nA.cm^{-2})	Corrosion potential E_{corr} (mV)	Corrosion rate mpy
φ = 0.0	1128	-291	0.302
φ = 1.2	6730	-541	1.58
φ = 2.25	9980	-752	3.09
φ = 0.0 + HA	370	-184	0.275
φ = 2.25 + HA	325	-677	0.167

4.7 Corrosion behavior of 316L SS

4.7.1 Rotary swaging samples

The potentiodynamic polarization curves of RS and AR samples are shown in Figure 4.28 the electrochemical data are listed in Table 4.6. The plastic deformation through rotary swaging led to a reduction in the current density and shift to the noble direction of the potential compared to AR samples. Metallographic observations (Figure 4.29) of the sample's surface after electrochemical tests showed a slight increase in resistance to pitting corrosion after rotary swaging. It can be seen that the number of corrosion pits on RS surface are less than that on the surface of AR samples. Therefore, it can be concluded that RS causes a reduction in the corrosion rate. The improvement of the corrosion resistance after RS due to the high density of grain boundaries in metals with nano-size grains enhances the formation of a passive film at the sample surface [208]. This consequently improves corrosion resistance through restriction of interaction between metal ions and surrounding corrosive environment.

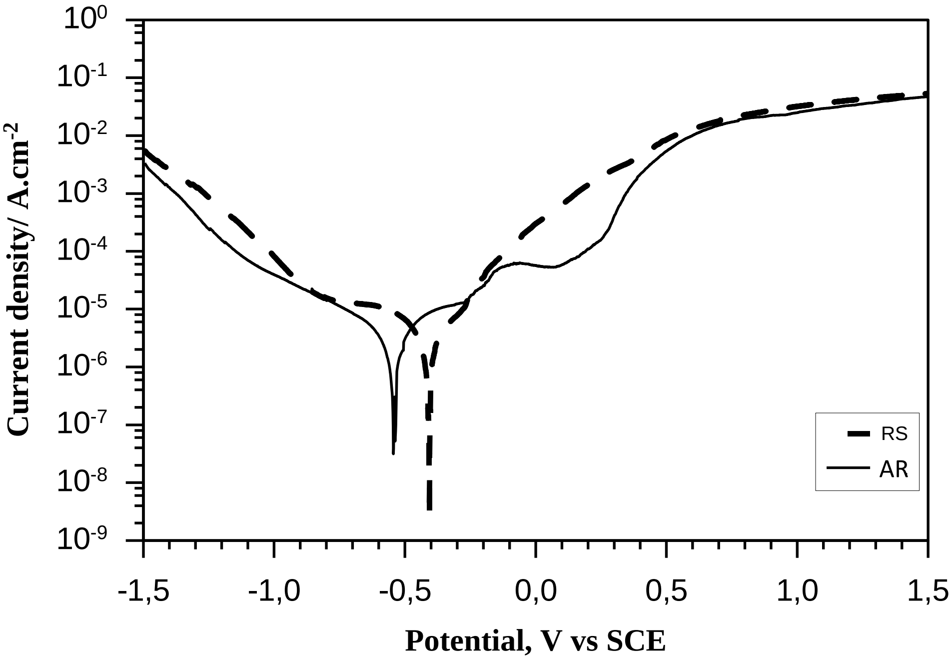

Figure 4.28, Potentiodynamic corrosion behavior of RS and RE of AISI 316L materials

Table 4.6: Results of electrochemical corrosion of AR and RS stainless steel

Surface condition	Corrosion current density, I_{corr}, µA.cm-2	Corrosion potential E_{corr}, mv	Corrosion rate, mpy
AR	4.2	- 541	0.89
RS	2.1	- 407	0.731

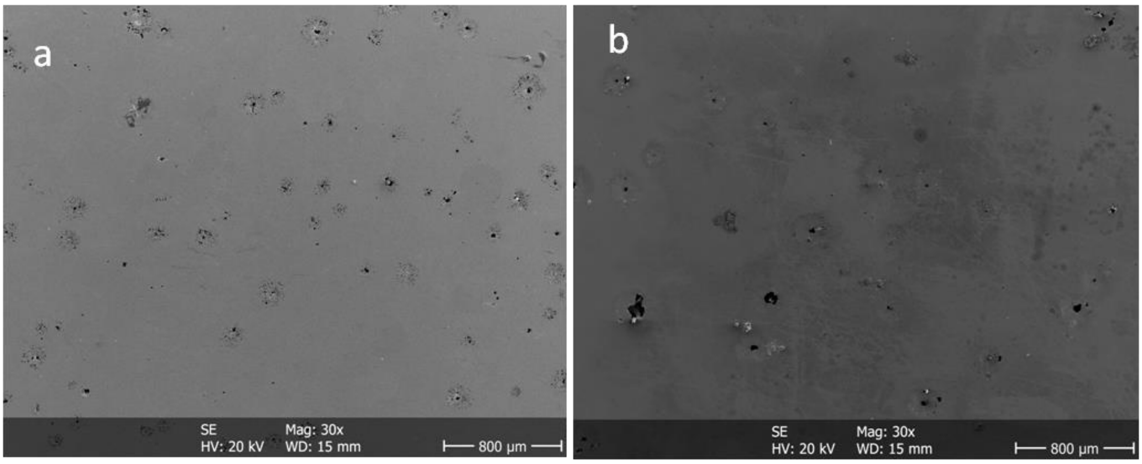

Fig. 4.29, SEM micrographs of surface morphologies of (a) AR and (b) RS samples

4.7.2 Shot peened samples

The corrosion current density (I_{corr}), corrosion potential (E_{corr}) and corrosion rate (C.R) of RE and SP specimens under different conditions were determined from polarization curves, Figure 4.30, and the results are shown in Table 4.7. Generally, SP affected inversely on the corrosion resistance of all shot peened materials with respect to RE sample. According to Figure 4.30 a, SP at the condition, 0.22mmA, 850µm shot size and coverage 100% (which it has the best corrosion resistance among all shot peened samples), led to increasing the corrosion current density (I_{corr}) compared with the RE specimens, where the corrosion rate of the RE sample increased from 0.89 to 1.73 mpy after SP. The effect of shot size on the corrosion resistance are represented in Figure 4.30 (b), It is evident from this figure that the corrosion potentials were found to shift slightly towards positive direction with an increase in shots size. Also, the results revealed that the corrosion current density increased with the decrease in the shot media size. The corrosion rate of shot peened samples reduced from 3.42 to 1.74 mpy after treatment with shots size 125-250µm and 850µm respectively. The increasing in the coverage peening has minor effect on the corrosion resistance. Figure 4.30 (c) show that the 200% coverage led to slightly increasing in the current density and potential corrosion subsequently increasing in the corrosion rate compared with 100% coverage peening under fixed other conditions. Table 4.2 shows that SP at 200 % coverage using 850 µm shots affected slightly the surface roughness compared to SP using shots size of 450 and 125-250 µm. The relatively low surface roughness, of samples treated at low and high coverage using 850 µm shots, led to a slight increase in the corrosion rate compared to the other SP conditions. Metallographic observations after polarization test show that the SP led to decreases the corrosion pitting resistance compared with the RE sample, Figure 4.31. It can be seen that the SP samples that have been treated with the smaller shots showed more pits compared to the reference and other SP samples. Therefore, it can be concluded that the shot size of peening treatment regards important parameters effect on the corrosion resistance. Stress corrosion cracking (SCC) was observed in the 200% peening coverage, Figure 4.32. It's obvious that cracks primarily nucleated at the left most or right most edges of the pitting. The defects and the structural inhomogeneity, which induced by high penning coverage, led to the SCC formation. Different analytical techniques such as autoradiography [209] SIMS [210] and XPS [211] exhibited local adsorption of Cl^- ions on the defects and inhomogeneity of oxide films because of the lower adsorption energy at these sites. It is deduced that a less defective oxide film with lower localized states is more resistant to pitting corrosion [212].

Research into stress corrosion cracking of SS 316 has shown that at high stress level, strain incompatibilities between ferrite and austenite encourage cracks to propagate along their interface [213]. Moreover, it is reported that the inclusions are likely to affect the pitting initiation [214]. The large number of defects on the rough samples increases the practical area for corrosion per unit area [44]. The higher surface roughness and heterogeneity are preferred locations for pit initiation, which subsequently results in the destruction of the passive region of the sample surface [45]. C. Aparicio et al. [215] revealed that the presence of surface compressive stress, instead of roughness, influences the corrosion behavior of metals after sandblasting. The change in the internal parameters of the crystal lattice because of sandblasting causes more reactive surface, which subsequently decreases the corrosion resistance of metals.

More investigation about the SP parameters effect on the corrosion behavior is possible by using electrochemical impedance spectroscopy (EIS). Figure 4.33 shows Nyquist plots obtained in Ringer solution at different surface conditions. Nyquist plots are often used in the electrochemical literature because they allow for an easy prediction of the circuit elements [216]. The Nyquist plot is a plot of real ($Z^{/}$) versus imaginary impedance ($Z^{//}$). The bigger the radii of arc are, the stronger the electrochemical impedance will be. Figure 4.33(a) show impedance spectra for RE, HA coated and uncoated SP samples. Firstly, it is worth noting that the impedance in the two un-coated systems is substantially lower than that seen in coated systems, it reached about 14 kΩ for coated sample compared with 6 kΩ and 4.2 kΩ for the reference and uncoated SP materials respectively, which is a logical situation due to the obvious corrosion barrier provided by the HA coating. Comparing the three Nyquist plots it is apparent that SP has a significant effect in reducing the impedance and thereby increasing susceptibility to corrosion. SP using larger shots led to a notable improvement of the corrosion resistance compared to the samples that have been SP with small shots. Figure 4.33(b) show that the oxide film impedance dropped from 4.7 kΩ to 1.8 kΩ after treatment at 850 µm and 125-250 µm shots respectively. The unfinished semicircle-arc was attributed to charge transfer process occurring at the metal/electrolyte interface or related to the surface passive film property [217]. In the same way, the high peening coverage (200%) affected to reduce the impedance compared with the low coverage peening (100%), where the impedance of the oxide film dropped from 4.7 kΩ to 2.3 kΩ after treatment at 100% and 200% respectively. The results obtained from the polarization technique were good agreement with those obtained from the electrochemical impedance spectroscopy (EIS) with a small variation.

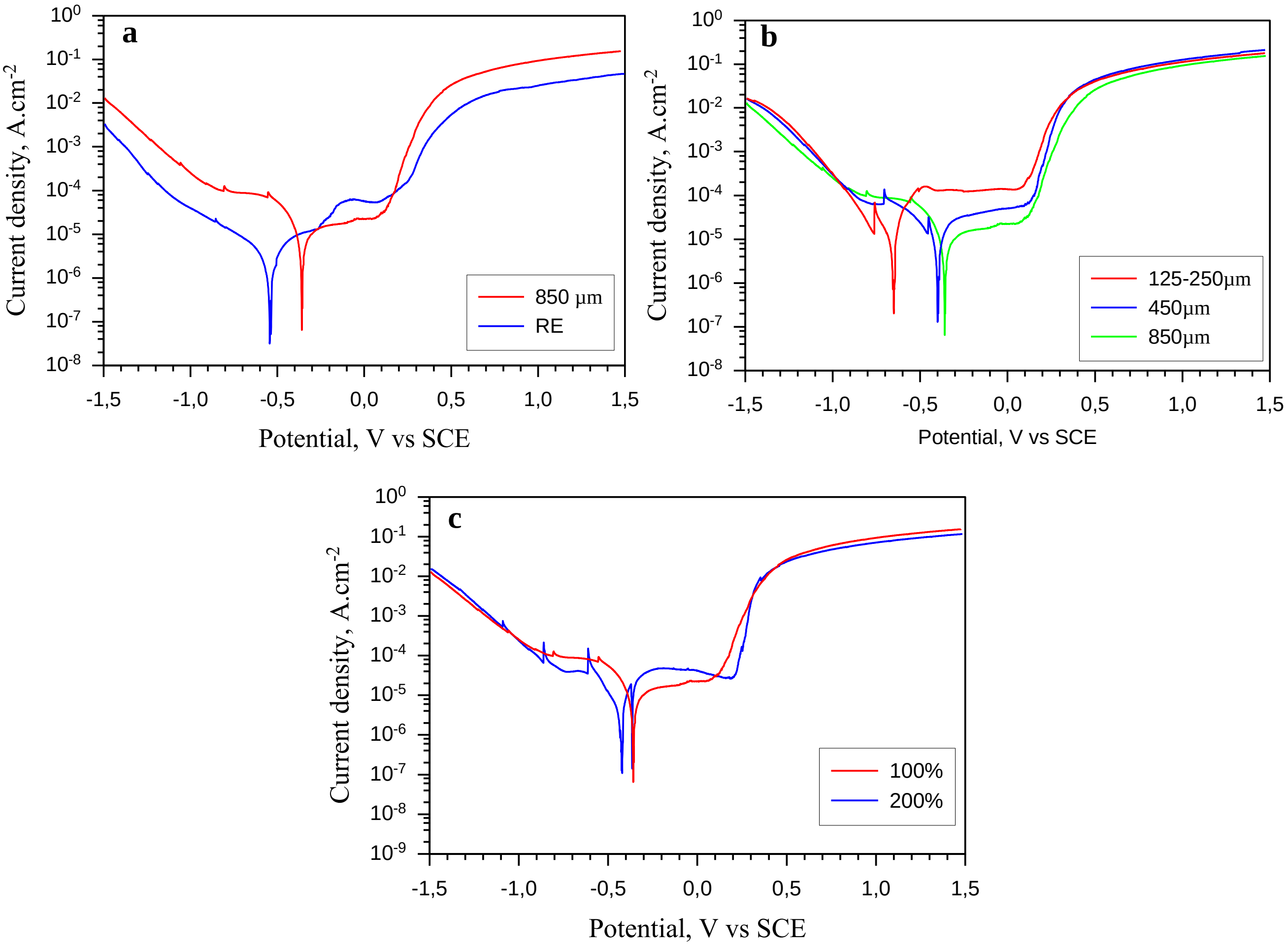

Figure 4.30, potentiodynamic polarization curves, (a) SP compared with RE sample, (b) effect of shot size and (c) effect of peening coverage

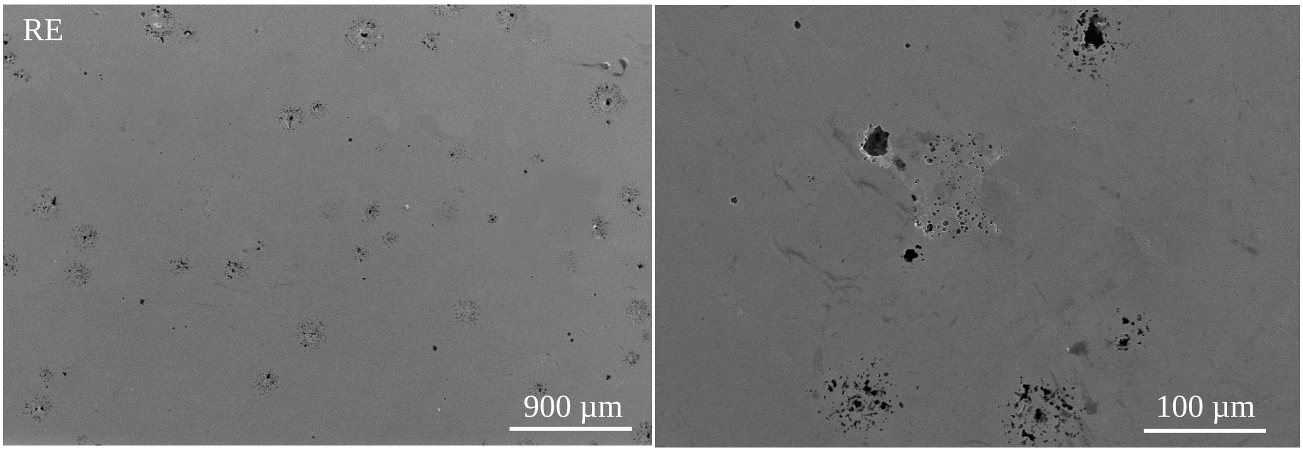

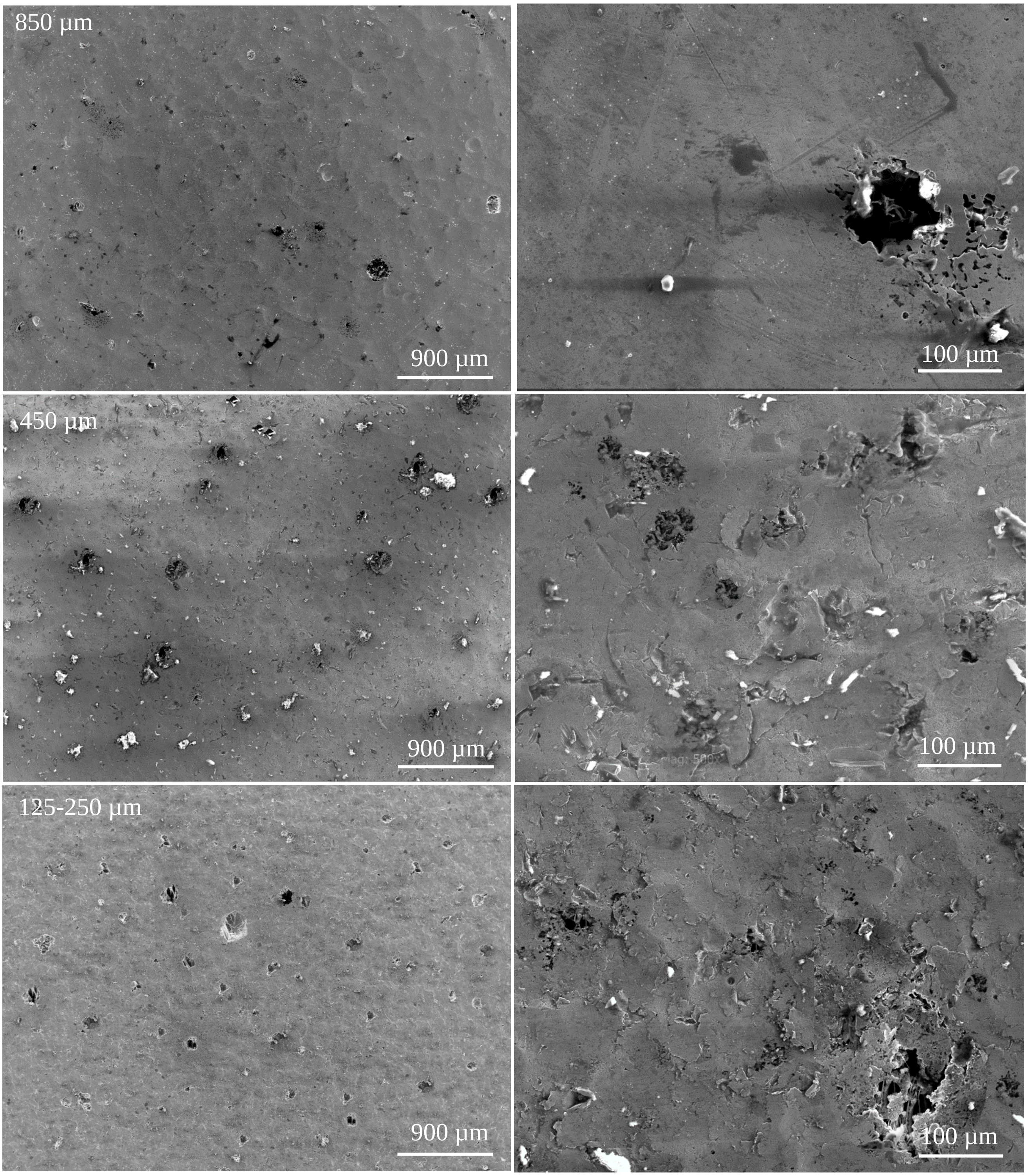

Figure 4.31, SEM micrographs with two magnifications: effect of shot size on the surface morphology after corrosion

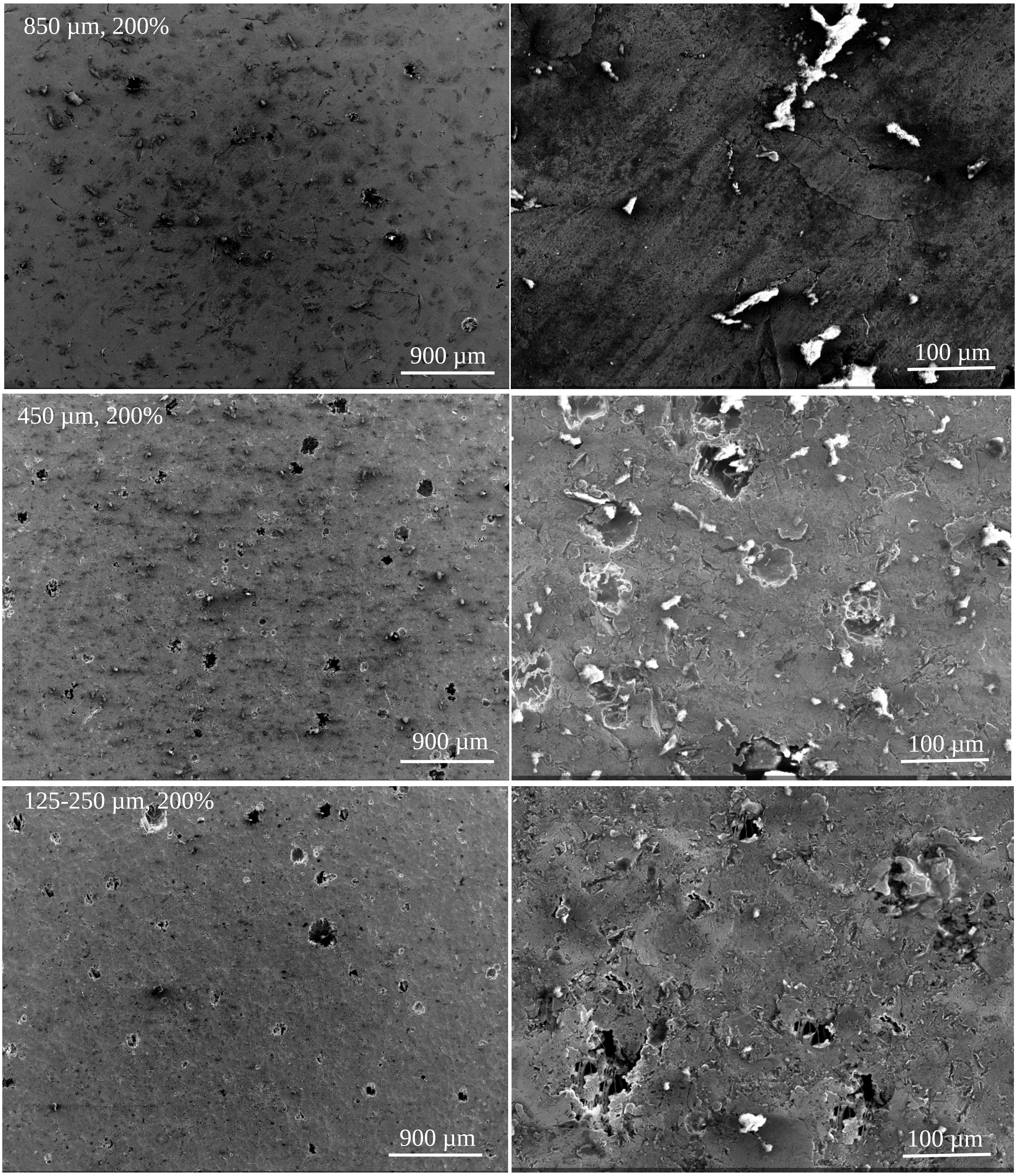

Figure 4.32, SEM micrographs with two magnifications: effect of coverage peening on surface morphology after corrosion

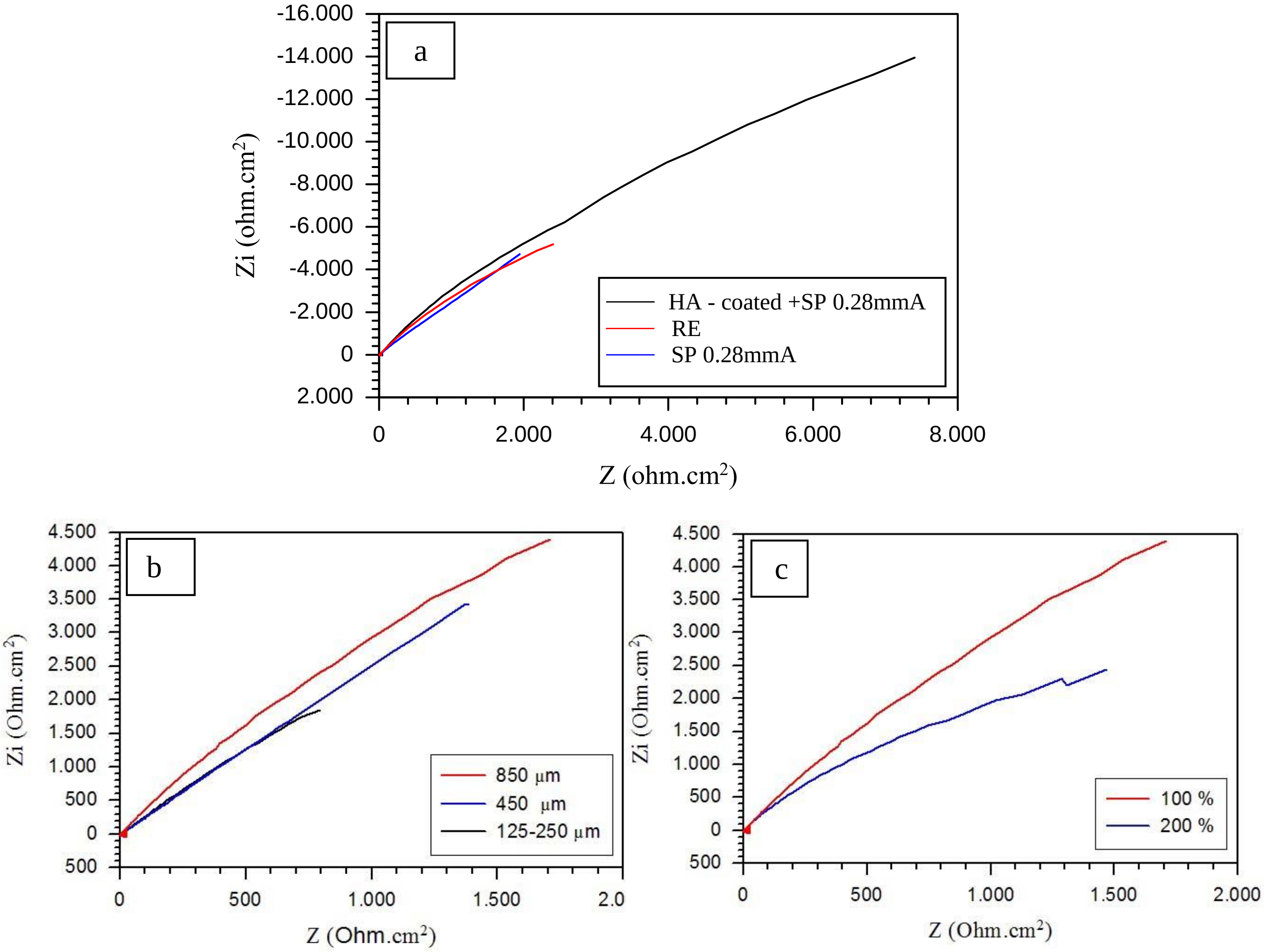

Figure 4.33, Nyquist plots of different surface conditions, a) RE compared with HA- coated and uncoated SP materials, b) effect of shot size, c) effect of peening coverage

4.8 Corrosion fatigue of SS 316L

The S–N curves of the AR material in the ambient air and Ringer solution environment are represented in Figure 4.34. The results show a significant decrease in the fatigue strength for the specimens in the corrosive environment compared to those tested in air. The high cycle fatigue (HCF) performance of the specimens in the corrosive environment decreases by 21% compared to those tested in air. The SEM observations show the fatigue cracks initiated from the corrosion defects at the surface as shown in Fig. 4.35 (a). For the fatigue test in air, fatigue crack initiation sites are located on the specimen surface as indicated in Fig. 4.35 (b). No clear evidence of defects (pores, inclusions, etc.) was found at the crack initiation locations.

Therefore, the fatigue crack growth rate in the Ringer solution was obviously faster than in air. Figure 4.36 depicts the S–N curves of uncoated and HA coated of AR, RS and SP materials in the Ringer solution. It is clear that, the fatigue strength of the AR material was increased by 40% and 35% after RS and SP respectively. SP introduced compressive residual stresses, work hardening and grain refinement in the surface layers that postpone the initiation and growth of surface cracks [218]. On the other hand, the superior HCF performance of RS material is explained by the very low surface roughness of condition RS that in addition, leads to a retardation of fatigue crack nucleation. M. Abdulstaar et al. [219] reported that the dislocation density accumulated during plastic deformation by RS markedly enhances the strength of the deformed material. Fig. 4.36 (b) shows a significant increase in the fatigue strength of the coated materials compared to the uncoated condition. The fatigue strength of coated-AR increased by about 27% compared to the uncoated-AR samples. HA coating after RS and SP led to a further increase of the fatigue strength by about 44 and 39% respectively compared to the AR material. The HA coating plays an important role by forming a barrier layer to prevent chloride ions from penetrating the substrate during cyclic fatigue and to reduce the corrosion pitting. The coating exhibits excellent adhesion to the substrate during the fatigue tests (Figure 4.37) that could increase the resistance of the material to fracture.

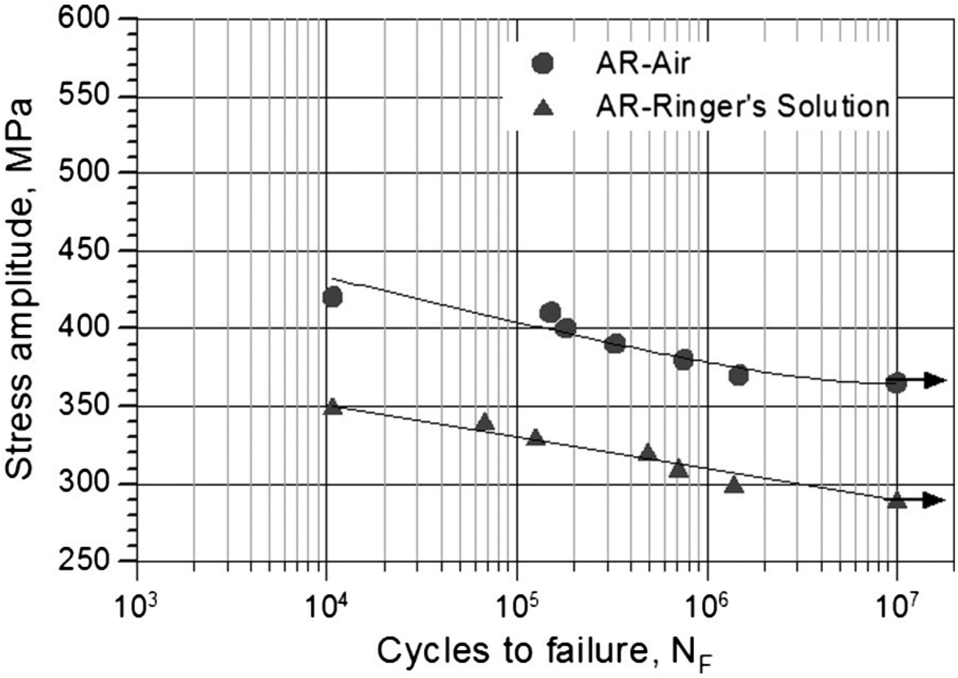

Figure 4.34, S–N curves of AR samples in rotating beam loading (R= −1) in the Ringer solution environment and in ambient air.

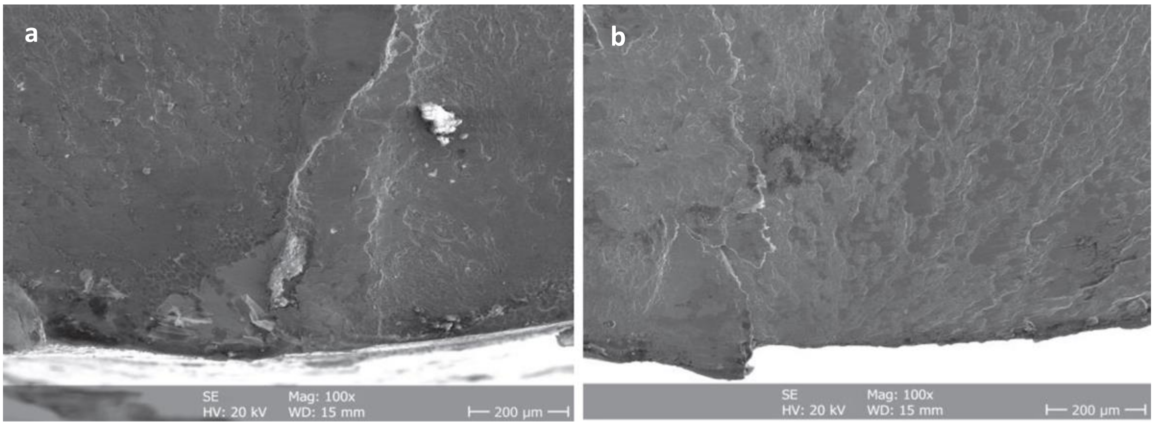

Figure 4.35, crack initiation sites in Ringer solution environment (a) and in ambient air (b)

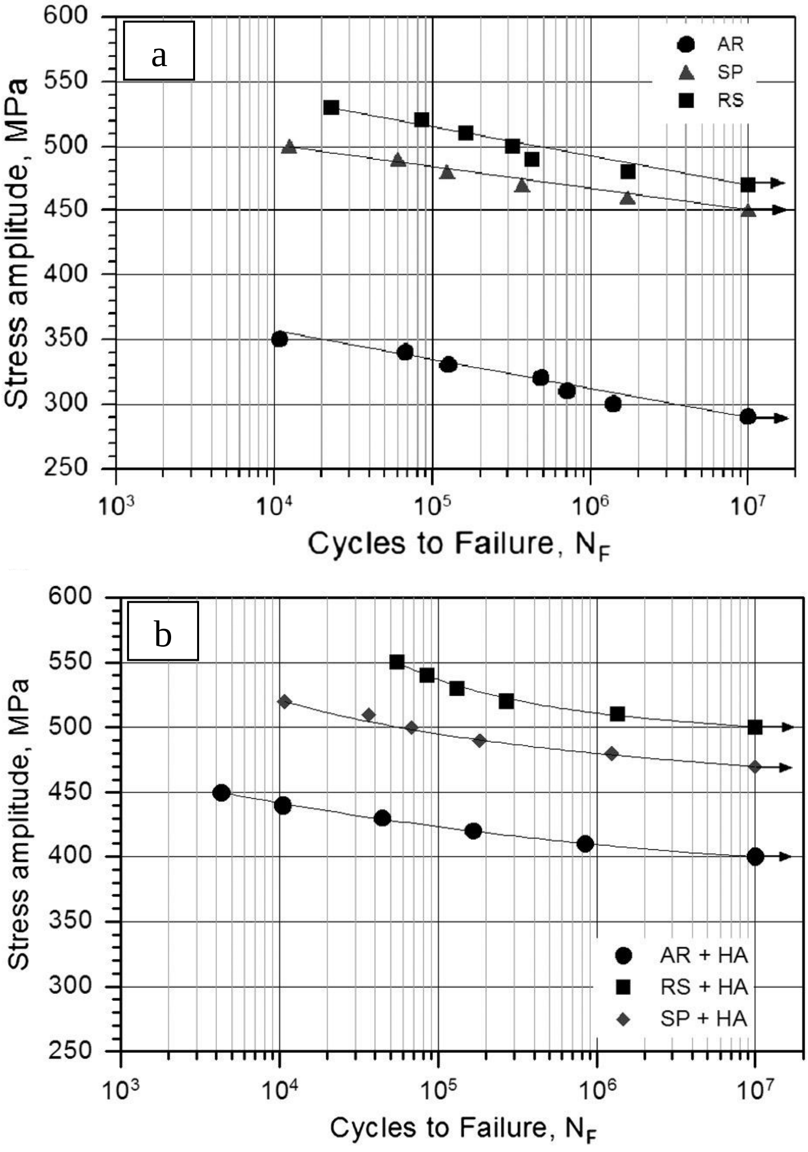

Figure 4.36, S–N curves of AR, RS and SP samples in Ringer solution environment (a) without coating and (b) with coating.

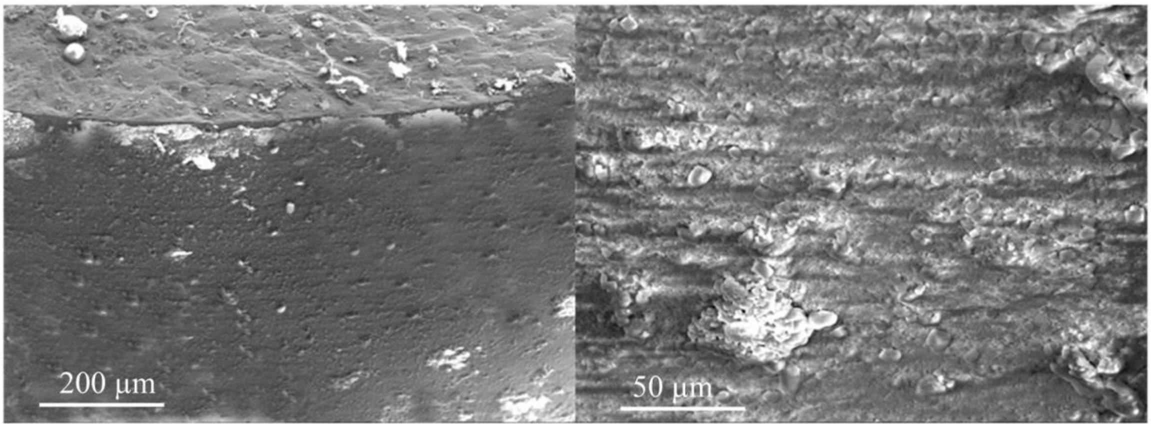

Figure 4.37, SEM observation of coating on fatigue sample after fracture.

Chapter five: Ti-6Al-4V

Results and Discussion

5.1 Metallographic features

The microstructure, of the three processed conditions, namely RS, GL and DU is characterized by optical microstructure and is presented in Figure 5.1, respectively. It can be seen that the grain size is too fine for the swaged material. Obviously, annealing the swaged sample at 840^{o}C for 1 h (GL) led to increasing the grain size gradually and became more coarsening after annealing at 970^{o}C (DU). GL microstructure consists of equiaxed particles of primary α phase (α_P) and β-phase is along the grain boundaries. Duplex (bimodal) structure consists of lamellar structure (α + β area) and in the grain triple-points there are created equiaxed α -particles. In the micrographs, the β phase appears dark and α phase is lighter [220]. Metallographic examination of the cross-section of the SP specimen using largest shot (850 µm) exhibited significant severe plastic deformation near the surface in the GL and DU materials (Figure 5.2). There is a clear difference in the grain size of the surface layer and the bulk substrate. Similar results were reported by Liu et al. [221], where significant grain refinement and severe plastic deformation in the top 30 nm thick were observed in type 316L SS as a result of ultrasonic shot peening.

5.2 Mechanical properties

The tensile properties (yield strength, ultimate tensile strength and elongation percent to fracture) and microhardness of the GL and DU conditions are summarized in Table 5.1. The DU materials showed the highest values of strength and hardness. The hardness value obtained for DU corresponds to extra hard condition obtained when it is quenched from high temperature solutioning [222]. The current results related to hardness and tensile properties are in agreement with the previous study [223]; it was found that tensile strength and hardness increase as the quenching temperature increases while the ductility decreases due to the higher volume fraction of α′ at higher quenching temperature. Mechanical properties of two-phase (α + β) titanium alloys are very sensitive to the morphology and geometrical arrangement of the two phases. A lamellar structure is characterized by high fatigue crack propagation resistance and high fracture toughness.

Important parameters for a lamellar microstructure with respect to the mechanical properties are the β-grain size, the size of the colonies of α-phase lamellae, thickness of the α-lamellae and the nature of the inter-lamellar interfaces (β-phase) [224-225]. One of the most influential microstructural parameters is the α colony size, since the α colony size determines the effective slip length in lamellar microstructures. The cooling rate from the homogenization temperature determines the α colony size and width of the α-lamellae within the β grains and the extent of the continuous α-layer at β grain boundaries.

Table 5.1 show that the values for the ultimate tensile strength that is significantly higher than the yield stress in GL and DU materials due to high work hardening capability.

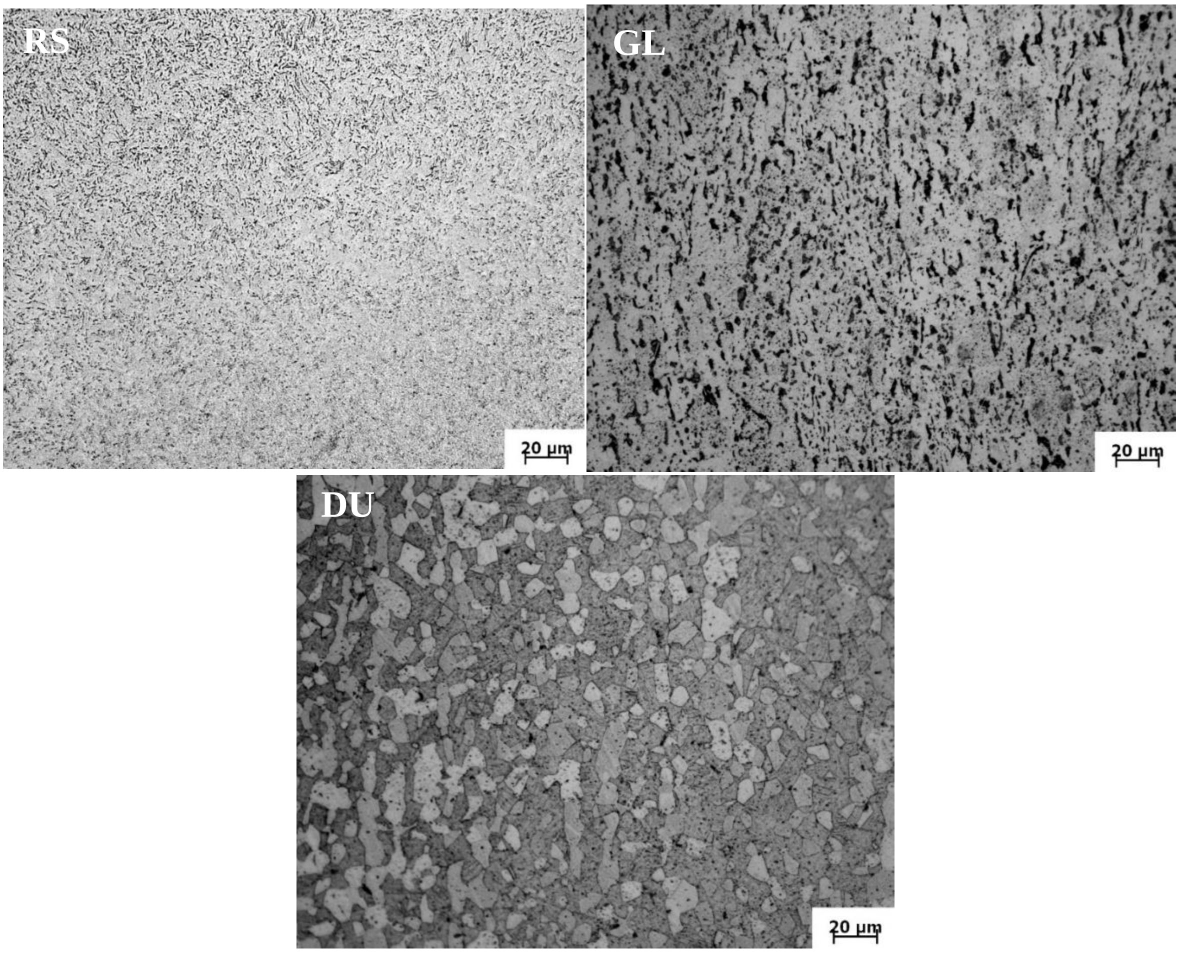

Figure 5.1, Microstructure of RS, GL and DU conditions of Ti-6Al-4V

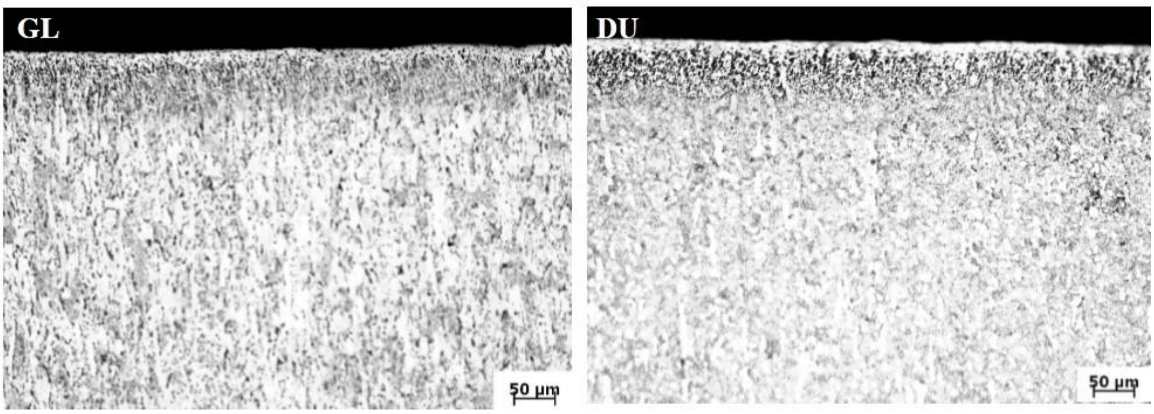

Figure 5.2, Cross-section of SP GL and DU samples showing modified surface layer by using 850 µm

Table 5.1: Tensile properties and hardness of GL and DU conditions

Condition	YS (MPa)	UTS (MPa)	Elongation (%)	Hardness (HV10)
GL	936	1037	16.6	332
DU	1097	1176	14.6	362

The total elongation to fracture of DU materials reduced as a result to decrease the ductility and increase the strength compared with GL materials.

Figure 5.3 displays the residual stress profiles of DU and GL specimens after SP using large shot 850 µm. The maximum residual compressive stresses of around 1096 MPa in DU and 1049 MPa in GL are produced at 100 µm beneath the surface. With the increase of depth from the surface, the residual stress profiles show drastic declining gradients, ending up with around -170 MPa at 300 µm beneath the surfaces. These areas should be considered as the main effective zones of the compressive residual stresses. Beyond these zones, residual stresses gradually approach zero.

Microhardness distributions across the samples sectional area with various SP shot size (850, 450 and 125-250 µm) are shown in Fig. 5.4 (a). SP markedly increased the surface hardness, which could confirm the SP-induced work-hardening effect due to the increase in dislocation density. An increase in the shot size slightly enhances the surface microhardness and the thickness of the plastically deformed, however, the effect of SP is limited to a very small depth of deformed layer. Both DU and GL are hardened to similar levels, reaching maximal values around 490 HV at the surfaces, Fig. 4.b. However, the influenced zone of DU spans to 0.25 mm, shallower than that of GL (Figure 5.4.b), which arrives at the depth of 0.4 mm. The surface hardness decreases gradually and approaches the bulk hardness 332 and 362 HV for GL and DU materials respectively.

The effect of SP varies depending on the microstructure of the material. It results in work-hardening, work-nonhardening or work-softening on the target material [226]. Work hardening occurs in the low-hardness target materials while work-softening happens in high hardness materials [227]. The material responses due to SP depend on the target material microstructure. But, the microstructure is also modified during the SP. The microstructure changes of target material include recrystallization, nano-grain formation [228], phase-transformation [229] and hardness changes.

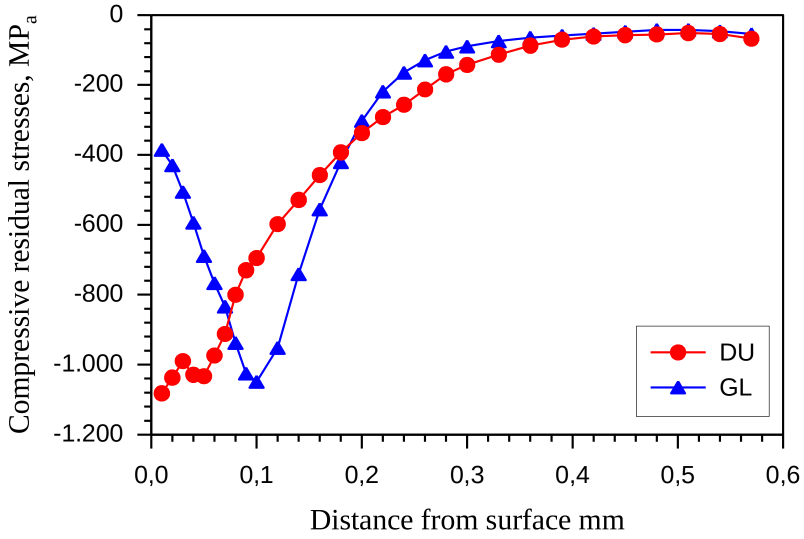

Figure 5.3, compressive residual stress-depth distribution of GL and DU samples after SP using 850 µm

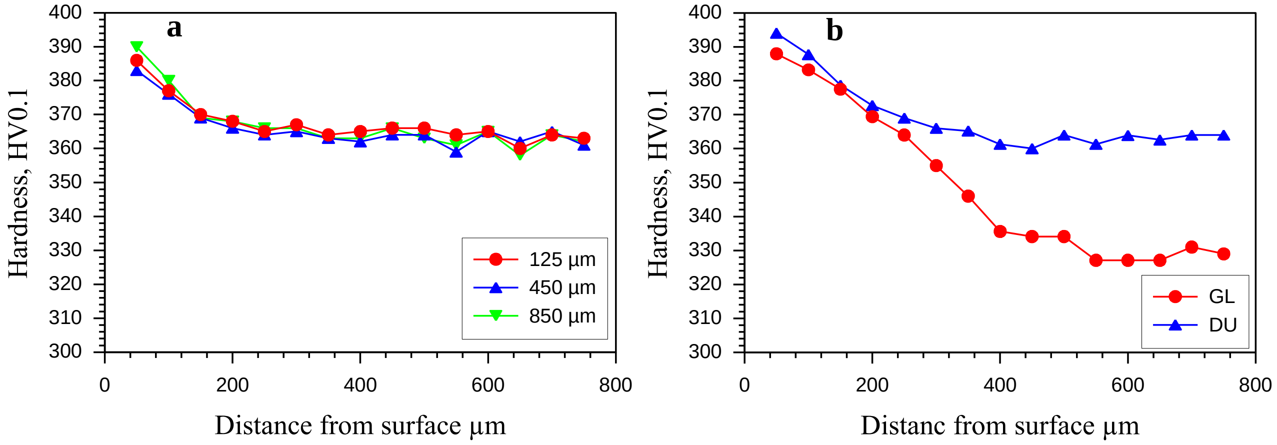

Figure 5.4, microhardness-depth distributions, a) effect of shots size on DU condition and b) effect of SP on DU and GL conditions by using 850 µm shot

5.3 Surface topography and roughness

The surface topography of GL and DU materials after SP using three shot size (850, 450 and 125-250 µm) are presented in Figure 5.5. It can be seen that decreasing the shot size will decrease the size of the peening dimple. That means an increased number of dimples per unit area. Therefore, uniformity and homogeneity of the surface increased as shot size increased. The fact that homogeneity of the surface increases after SP by using big shots is verified by Surface roughness measurement results. As clear from the Table 5.2, the surface roughness parameters (Ra, Rmax and Rz) decreasing gradually with increasing the diameter of shot size. The SEM in figure 5.5, show that SP using largest shot 850 didn't remove the grinding marks on the surfaces while these marks disappeared after SP when have used the small shots 450 and 125 µm. Similar findings were found in the Reference [230]. Table 5.2, show that the roughness values of GL is slightly higher than DU materials. The differences in the measured roughness values due to the higher hardness and mechanical strength of DU samples limit the ability of the material to suffer further plastic deformation by the particles. The SEM Figure showed the presence of ceramic particles fragment especially at the samples that have been treated using small shots. The presence of particles embedded in the surface of shot peened samples is a consequence of the high kinetic energy levels imparted to the particles during treatment. Since the shot size depends on the peening intensity [231], therefore, whenever shot size decreased should increase its velocity to achieve the same Almen intensity. This argument could explain the presence of the fragments of ceramic shots significantly in the shot peened samples using smaller shots.

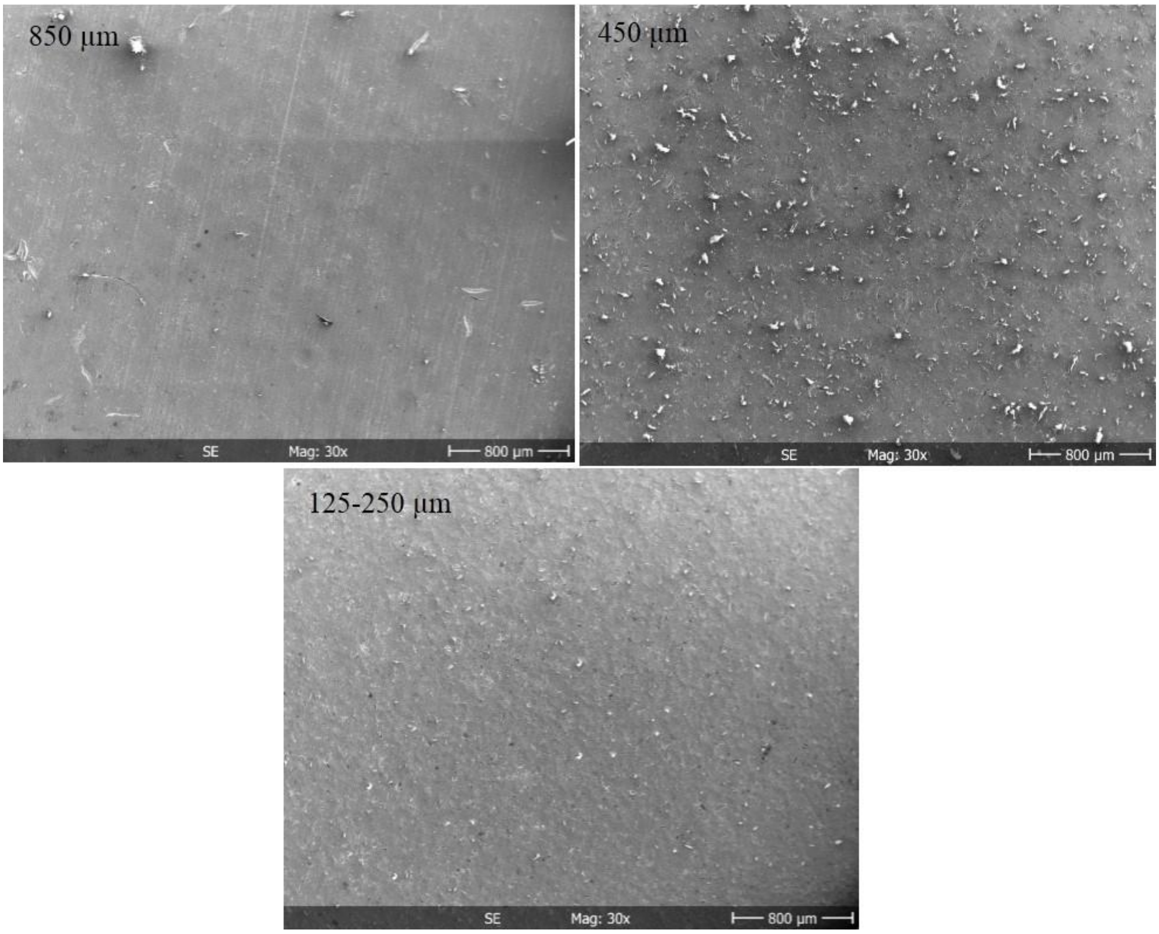
850 µm
SE
Mag: 30x
800 µm
450 µm
SE
Mag: 30x
800 µm
125-250 µm
SE
Mag: 30x
800 µm

a

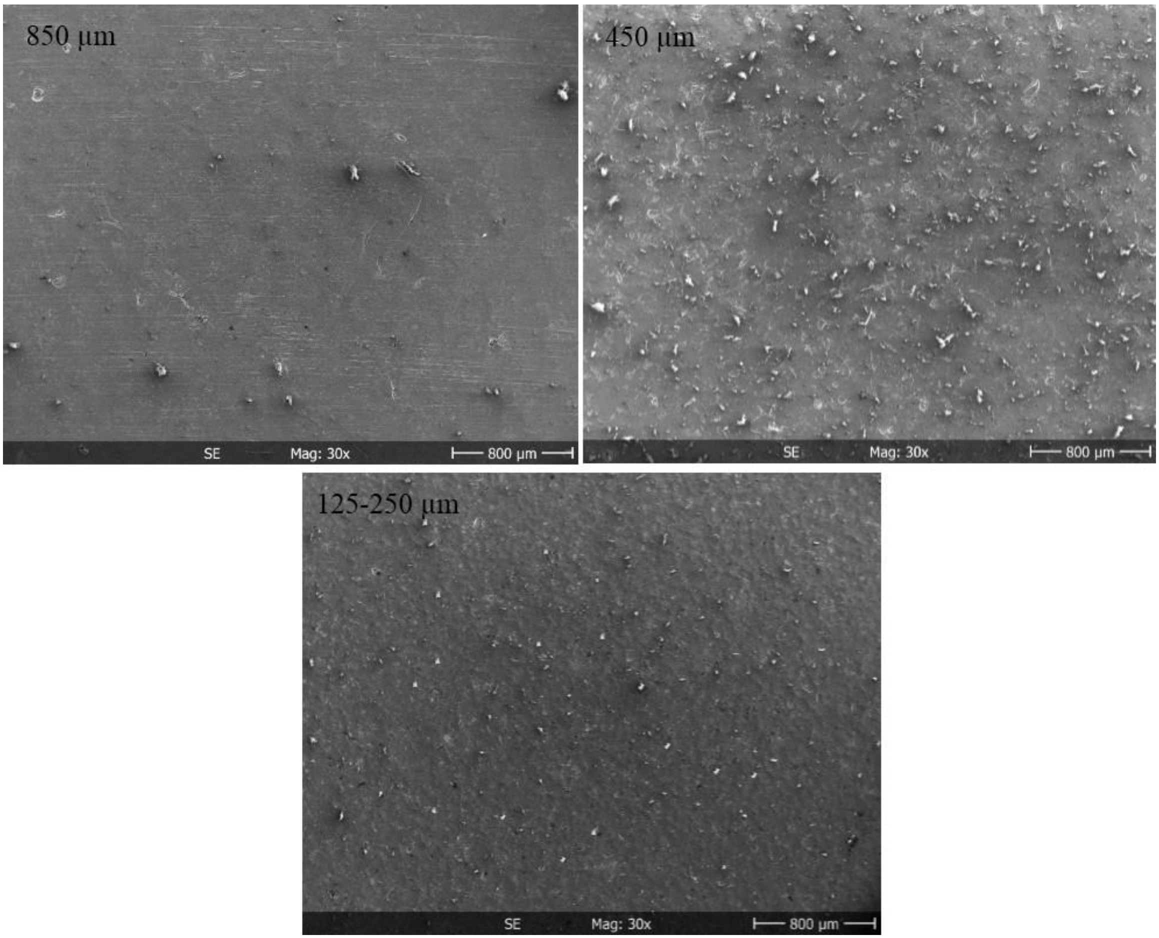

b

Figure 5.5, Effect of SP at three shot size on the surface topography of a) DU and b) GL conditions

Table 5.2: Roughness parameters values

Materials	surface conditions	Rmax/ µm	Ra/µm	Rz/ µm
DU	Before SP	0.255	0.025	0.20
	125-250 µm	4.71	0.67	3.23
	450 µm	5.12	0.74	4.71
	850 µm	3.32	0.43	2.21
GL	Before SP	0.28	0.025	0.22
	125-250 µm	5.24	0.85	4.4
	450 µm	5.80	0.78	4.69
	850 µm	3.34	0.46	2.25

5.4 Corrosion behavior

The results obtained from potentiodynamic polarization study for RS, GL and DU samples are given in Table 5.3 and Figure 5.6. The polarization curves indicate that there was little difference in corrosion rate for the RS and DU samples, while the GL samples showed the higher corrosion rate. Tafel analysis was performed on the polarization curves and the average corrosion current densities were found to be: 466, 450 and 857 nA/cm^2 for RS, DU, and GL microstructures, respectively. The potential corrosion of DU sample drift upward suggesting improved passivity with time. The increase in the corrosion rate of GL compared with the DU samples, is the result of distribution rearrangement of the alloy elements that occur with increasing the heat treatment temperature. Among the primary alloying elements of Ti-6Al-4V alloy, Al is the α stabilizing element, although it also has significant solubility in the β phase. In contrast, V is a β stabilizing element and has limited solubility in the α phase [232] Consequently, during elevated temperature heat treatment, Al tends to segregate to the α phase while V partitions to the β phase. Furthermore, the extent of Al partitioning increases with decreasing α phase volume fraction, i.e., with increasing the solution treatment temperature [88]. According to Levy and Sklover [233], a potential difference between α and β phases causes galvanic interaction between the α and β phases in Ti-6Al-6V-2Sn two-phase alloys. The magnitude of the interaction, certainly, depends on the composition of each phase, which, in turn, depends on the heat treatment history of the alloy. Relatively, RS materials showed low current density and corrosion rate. It is reported that the high density of grain boundaries in metals with nano-size grains enhances the formation of passive film at the sample surface [208]. This consequently improves corrosion resistance through restriction of interaction between metal ions and surrounding corrosive environment. Natural oxide on the metal surface functions as a protective layer against the electrochemical reactions in the corrosive environment. In the case that the natural oxide layers, on the metal surface, are thicker, it will be much more resistant in corrosive environment [234]. Natural oxide on the metals surface possesses the high density due to high grain boundaries density [235]. Consequently, the denser passive layer of nanostructured RS materials led to improves the corrosion resistance.

The potentiodynamic polarization curves of DU and GL materials after SP are presented in Fig 5.7, and the results are shown in Table 5.3. It’s noted that no significant effect of SP using the large shot 850 µm on the corrosion behavior of DU materials while the effect was clear on the corrosion resistance of GL materials using the same shot. The surface roughness of the GL material was slightly higher than the DU, Table 5.2, making it one of the reasons to decrease the corrosion resistance of the GL material after SP.

The decrease in shot size of peening led to increasing the corrosion current density and corrosion rate in the two conditions (DU and GL). The corrosion rate of shot peened samples reduced from 1.68 to 0.22 mpy for the DU and from 1.62 to 0.78 mpy for the GL materials after treatment with shots size 125- 250µm and 850µm respectively. Therefore, it can be concluded that the shot size of peening treatment regards important parameters effect on the corrosion resistance. The irregularities observed by SEM, Fig 5.5, for the Shot peened samples using small shot promote greater surface roughness, as clear from Table 5.2. This greater roughness is due to plastic deformation generated by the impact of spheres on the metal surface during the shot peening process. The higher surface roughness and heterogeneity are preferred locations for the destruction of the passive film region of the sample surface which subsequently results in increasing the corrosion rate.

More investigation of the corrosion behavior is possible by using electrochemical impedance spectroscopy (EIS). Figures 5.8 and 5.9 show Nyquist plots obtained in Ringer solution at different conditions. Nyquist plots are often used in the electrochemical literature because they allow for an easy prediction of the circuit elements [216]. The Nyquist plot is a plot of real ($Z^{/}$) versus imaginary impedance ($Z^{//}$). The bigger the radii of arc are, the stronger the electrochemical impedance will be. Figure 5.8 show impedance spectra for RS, DU and GL samples. As expected, the impedance values of RS and DU materials are very close, were reached about 53 and 54 kΩ for RS and DU samples respectively. GL material registered the lowest impedance value, 23kΩ, among the untreated samples. This result corresponds to what we found in the potentiodynamic polarization experiment. Figure 5.9 represent the comparison among the shot peened samples using three shot size. It's clear from Figure 5.9 a, there is slightly drop in the impedance value of DU material from 54 to 51 kΩ after SP using large shot 850 µm. Figure 5.9 b indicates that the impedance of GL sample decreased from 23 to 18 kΩ after treated with the same shot, noting a further deterioration in corrosion resistance. However, SP using larger shots led to a notable improvement in the corrosion resistance of the two conditions compared to the samples that have been treated with small shot. It’s noted that the oxide film impedance dropped from 51 to 18 kΩ and 23 to 9 kΩ for DU and GL materials after SP at 850 and 125-250 µm shot respectively. The unfinished semicircle-arc was attributed to charge transfer process occurring at the metal/electrolyte interface or related to the surface passive film property [217]. The results obtained from the polarization technique were good agreement with those obtained from the electrochemical impedance spectroscopy (EIS) with a small variation.

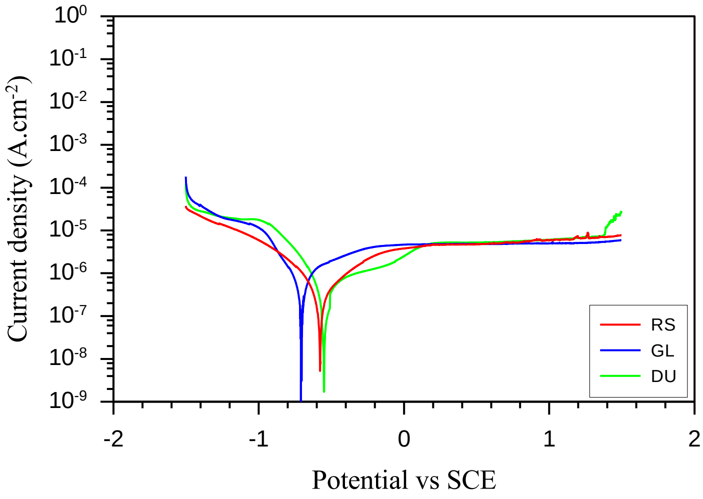

Figure 5.6, potentiodynamic corrosion behavior of RS, GL and DU conditions

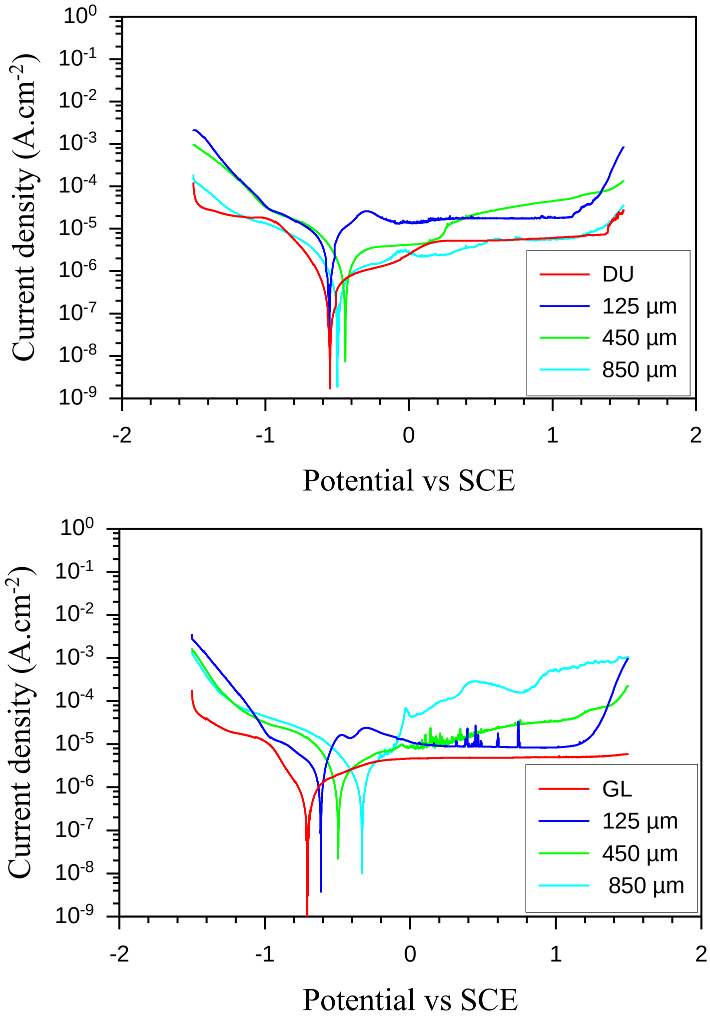

Figure 5.7, potentiodynamic corrosion behavior of DU and GL conditions before and after SP at three shot size

Table 5.3: Results of electrochemical corrosion at different surface conditions

Conditions	**current density, i_{corr}/ nA/cm^{-2}**	**potential E_{corr}/ mV**	**Corrosion rate/ mpy**
RS	466	- 577	0.223
DU	450	- 549	0.210
GL	857	- 706	0.411
DU-SP125-250 µm	3611	- 555	1.680
DU-SP 450 µm	2107	- 443	0.999
DU-SP 850 µm	461	−495	0.222
GL-SP 125-250 µm	3580	-615	1.623
GL-SP 450 µm	3531	-496	1.674
GL-SP 850 µm	1640	-332	0.786

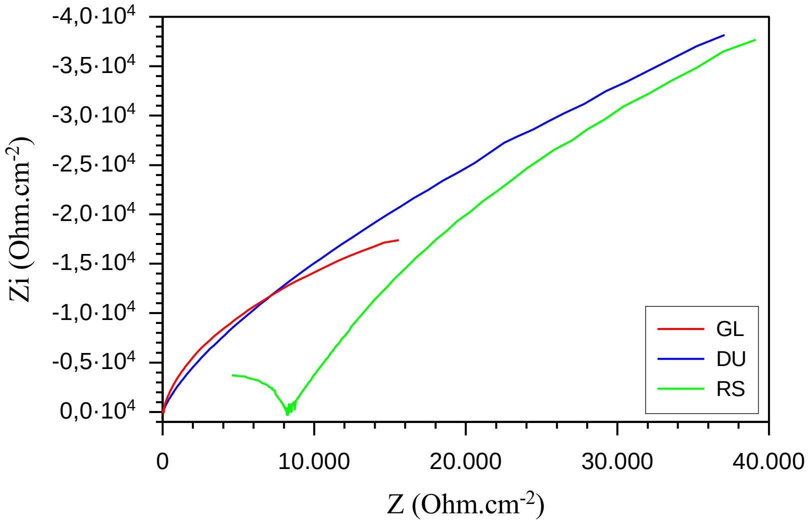

Figure 5.8, Nyquist plots of RS, GL and DU conditions

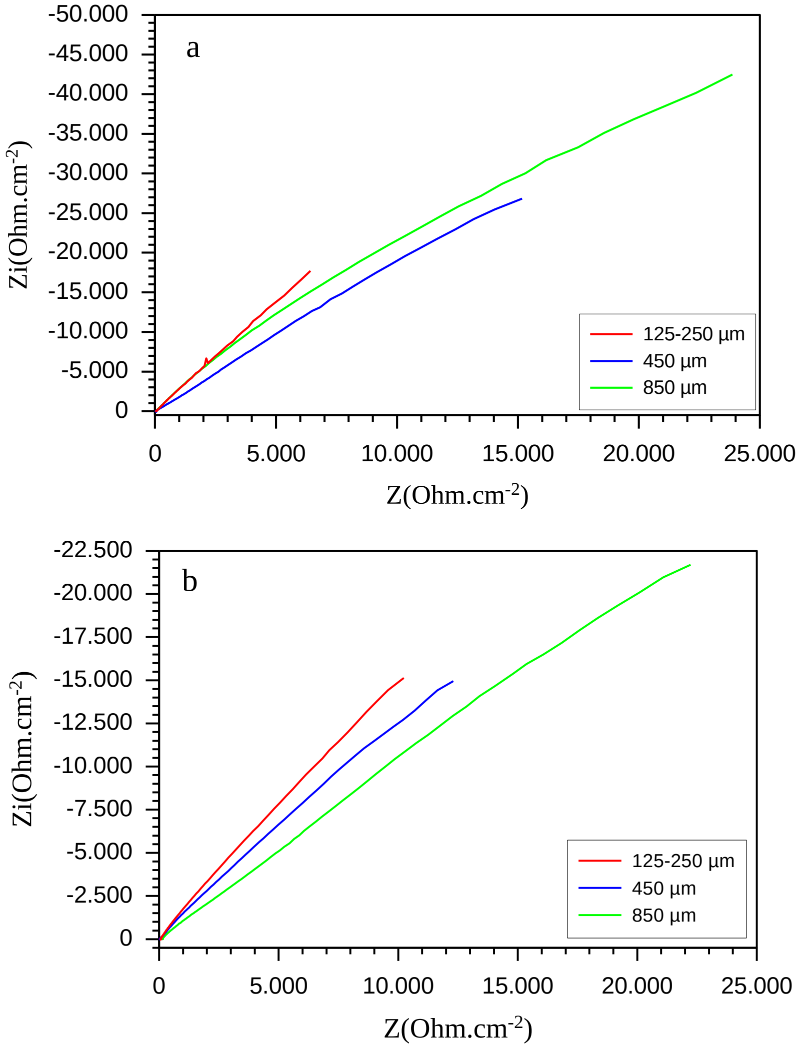

Fig. 5.9, Nyquist plots of a) DU and b) GL after SP at three shot size

Chapter 6

Conclusions

6.1 Stainless steel 316Ti

The plastic deformation, through cold rolling, and HA coating were evaluated for their ability to improve the mechanical properties and corrosion resistance of 316Ti SS. The following conclusions can be drawn from this research.

- Increasing the deformation degree by cold rolling led to a marked increase of the hardness from about 125 to 460 HV10. The observed strengthening may be caused by strain-induced transformation of the austenite to martensite.
- Compared to the non-deformed material, increasing the deformation degree led to a clear shift in the corrosion potential (E_{corr}) to the negative direction and an increase in the anodic current density (I_{corr}).
- Pits initiation frequency increased with the deformation degree.
- The formed HA coating was homogeneous and dense, and completely covered the underlying substrate material. The formed coating had an average Ca/P ratio of 1.63.
- The HA-coated surface revealed markedly higher roughness values compared to the grinded surface. HA coating resulted in a significant reduction of the corrosion current density. The corrosion current density (I_{corr}) and corrosion rate of the deformed material (φ= 2.25) dropped from 9980 nA.cm-2 and 3.09 mpy to 328 nA.cm-2 and 0.167 mpy, respectively.

6.2 Stainless steel 316L

6.2.1 Rotary swaging and shot peening

Bulk and surface plastic deformations, through RS, and several SP treatments combining different shot sizes, peening coverage percentage and peening intensities were applied to AISI 316L stainless steel. The effect of these treatments on the corrosion behavior, wettability and some mechanical properties were studied. Moreover, the corrosion resistance by using impedance spectroscopy test and the wettability were also investigated after coated of AISI 316L by hydroxyapatite. The following points could be drawn out:

- RS increases the bulk microhardness, tensile and yield strength of the AISI 316L stainless steel.
- SP resulted in near-surface maximum hardness values comparable to those observed after RS. This indicates that microstructural changes in the near-surface due to SP were similar to those in RS deformation.

- The increase in the peening coverage and the Almen intensity markedly improved the microhardness and compressive residual stresses in the surface layer, while the peening intensity depends on the shot size.
- RS improved the corrosion resistance; however, the higher surface roughness after SP led to a marked decrease of the corrosion resistance.
- The increase in the shot size, play an important role to decrease the corrosion rate; However, SP generally reduces the corrosion resistance compared with the RE material.
- SP improved the wettability by reducing the contact angle due to the high surface roughness which induced by SP.
- Shot peened HA coated samples have the lower contact angle due to the porosity and the chemical composition of this coating.
- HA coating provided the material with high corrosion resistance, where registered the highest impedance value compared with the uncoated materials.
- There is a good agreement between results of potentiodynamic polarization and electro impedance tests.
- The findings of this research are in line with the published experimental results, especially concerning the influence of SP on the wetting properties and the corrosion behavior.
- There is a significant decrease in the fatigue strength under corrosive environment (Ringer solution) compared to the fatigue strength in air.
- The fatigue strength under corrosive environment had been markedly enhanced by 40% and 35% after RS and SP respectively.
- HA coating after RS and SP led to a further increase of the fatigue strength of the AR material by about 44 and 39% respectively.

6.2.2 Sintering of HA- coating

HA coating was successfully deposited on stainless steel 316 L substrates by the simple chemical method. The as HA-coated samples were subjected to sintering at 500, 600 and 700°C. SEM, EDX analysis and the coating/substrate adhesive strength characterized the resulting HA-coated surfaces. Furthermore, the corrosion behavior of the various surfaces was tested in Ringer’s solution at 37±1°C. The main conclusions were as following:

- The as HA-coated surfaces exhibited a needle-like morphology with a thickness of 12 µm and a visible coating/substrate interface.
- Sintering fused the HA particles that resulted in a well-dispersed structure and good adherence coating.
- EDX analysis of the as HA-coated surface detected the presence of the substrate alloying elements in the coating layer because of the existence of some micro-pores. In contrary, the intensities of the substrate alloying elements were barely appeared after sintering.
- After sintering, HA coating tended to aggregate within agglomerated HA-particles that resulted in a slightly higher surface roughness.
- Sintering modified the coating microstructure and improved the coating/substrate adhesion due to incorporation and diffusion of coating elements in the substrate, which increased the interlocking between coating and substrate.
- The HA-coated material exhibited clear improvement in the corrosion resistance compared to the un-coated material.
- Sintering of HA- coated samples possessed higher corrosion resistance due to the thinner and fully coated surfaces after sintering that diminishes the surface micro-pores.

6.3 Ti-6Al-4V

Evolution of ultra-fine grain Ti-6Al-4V Followed by heat treatment was done to get the DU and GL microstructure. The surface modification through SP using three shot size was applied on these microstructures. The relationship between different microstructures and corrosion behavior were investigated. Moreover, the effect of SP on the corrosion resistance and mechanical properties were also studied. The main conclusions that can be drawn from this study are:

- The DU materials showed the highest values of strength and hardness compared to GL due to the extra hard condition obtained when it is quenched from high temperature solutioning.
- SP resulted in the maximum hardness and residual stresses in the near surface of the two microstructures. However, the influenced zone of GL was more depth than DU materials due to microstructure variation.

- SP generated a rough surface in the two microstructures. However, the surface roughness of GL induced by SP was slightly higher than DU.
- Potentiodynamic polarization curves and impedance spectroscopy experiments revealed that the corrosion resistance of GL was lower than DU and UTF grain microstructure.
- No significant effect of SP using large shot on the corrosion behavior of DU while the SP led to increasing the corrosion rate of GL materials markedly.
- The decreasing of shot size peening led to reducing the corrosion resistance of two microstructures significantly.
- There is a good agreement between results of potentiodynamic polarization and electro impedance tests.

References

1. D F Williams, Electrochemical aspects of corrosion in the physiological environment. In Fundamental aspects of biocompatibility, 1(1981)11–20.
2. AF Tencer. Osteocompatibility. In: von Recum AF (ed). Handbook of biomaterials evaluation: scientific, technical, and clinical testing of implant materials. 2nd edition, Taylor and Francis, Philadelphia, PA, 1999.
3. G. D. Manivasagam, Dhinasekaran, A. Rajamanickam, Biomedical Implants: Corrosion and its Prevention – A Review, Recent patents on Corrs. Sci. 2 (2010) 40-54.
4. S. Kurtz, K. Ong, E. Lau, F. Mowat, M. Halpern, Projections of primary and revision hip and knee arthroplasty in the United States from 2005 to 2030, J Bone and Joint Surgery Am, 89 (2007) 780-785.
5. A. J. Smith, P. Dieppe, K. Vernon, M. Porter, A. W Blom; on behalf of the National Joint Registry of England and Wales, The Lancet, 379(2012) 1199-1204.
6. Rack H. J., Qazi J. I., Titanium alloys for biomedical applications, Materials Science and Engineering C 26 (2006) 1269-1277.
7. M. Spector, Biomaterial failure, Orthopedic Clinics of North America, 23(1992) 211-217.
8. M. Navarro, A. Michiardi, O. Castaňo, J.A. Panell, Review: Biomaterials in orthopaedics, J. The Royal Soc. Interface 5 (2008) 1137-1158
9. J. Stráský, J. Havlíková, L. Bačáková, P. Harcuba, M. Mhaede, M. Janeček, Characterization of electric discharge machining, subsequent etching and shot-peening as a surface treatment for orthopaedic implants, Applied Surface Science, 281 (2013)73 - 78.
10. S. Virtanen, I. Milošov, E. Gomez-barrenas R. Trebše, J. Salo, Y. T. Konttinen, Special modes of corrosion under physiological and simulated physiological conditions, Acta Biomaterialia, 4(2008)468-476.
11. K. Meinert, C. Uerpmann, J. Matschullat, G. K. Wolf, Corrosion and leaching of silver doped ceramic IBAD coatings on SS 316L under simulated physiological conditions, Surface Coatings and Technology, 103-104(1998)58-65.
12. C. Garcia, S. Cere, A. Duran, Bioactive coatings prepared by sol–gel on stainless steel 316L, J Non-Crystalline Solids 348 (2004) 218-224.

13. S. Nagarajan, N. Rajendran, Surface characterisation and electrochemical behaviour of porous titanium dioxide coated 316L stainless steel for orthopaedic applications, Applied Surface Science, 255(2009)3927-3932.
14. G. Wang, H. Zreiqat, Functional coatings or films for hard-tissue applications, Materials, 3 (2010) 3994-4050.
15. B. Ravi Kumar, Sailaja Sharma, B. Mahato, Formation of ultrafine grained microstructure in the austenitic stainless steel and its impact on tensile properties,Materials Science and Engineering A, 528(2011)2209–2216.
16. R. Huiskes, H. Weinans, B.V. Rietbergen, The relationship between stress shielding and bone resorption around total hip stems and the effects of flexible materials, Clin Orthop. Relat. Res. 274(1992)124-34
17. J. Walczak, F. Shahgaldi, F. Heatley, In vivo corrosion of 316L stainless-steel hip implants: morphology and elemental compositions of corrosion products, Biomaterials. 19 (1998) 229-37.
18. K. K. Chew, S. H. S. Zein, A. L. Ahmad, The corrosion scenario in human body: Stainless steel 316L orthopaedic implants, Natural Science 4(2012)184-188.
19. M. Semlitsch, Titanium alloys for hip joint replacements, Clinical Materials 2 (1987)1-13.
20. C. Leyens, M. Peters, Titanium and Titanium Alloys - Fundamentals and Applications. Wiley - VCH Verlag GmbH & Co. KgaA: Weinheim, Germany 1 - 42 (2003)454-455.
21. H. Yang, K. Yang, B. Zhang, Pitting corrosion resistance of La added 316L stainless steel in simulated body fluids, Mater. Lett. 61 (2007) 1154.
22. U. Kamachimudali, T.M. Sridhar, B. Raj, Corrosion of bio implants, Sadhana 28 (2003) 601.
23. S. Griza, G. Zanon, E.P. Silva, F. Bertoni, A. Reguly, T.R. Strohaecker, Design aspects involved in a cemented THA stem failure case, Eng. Failure Anal. 16 (2009)512.
24. J. Allain, D. Goutallier, M.C. Voisin, S. Lemouel, Failure of a stainless-steel femoral head of a revision total hip arthroplasty performed after a fracture of a ceramic femoral head, Bone Joint Surg. Ser. A. 80(1998)1355.

25. HS. Hedia, DC. Barton, J. Fisher, Material optimization of the femoral component of a hip prosthesis based on the fatigue notch fatigue approach, Biomed. Mater. Eng. 7(1997)14 83-98.
26. S.H. Teoh, Fatigue of biomaterials: a review, Int. J. Fatigue 22 (2000) 825–837.
27. M. Baleani, M. Viceconti, A. Toni, The effect of sandblasting treatment on endurance properties of titanium alloy hip prostheses, Artif. Organs 24(2000) 296.
28. M. Jasty, W.J. Maloney, C.R. Bragdon, D.O. O'Connor, T. Haire, W.H. Harris, The initiation of failure in cemented femoral components of hip arthroplasties, Bone Joint Surg. Ser. B. 73(1991) 551.
29. S. Xu, X.Q. Wu, E.H. Han, W. Ke, Y. Katada, Crack initiation mechanisms for low cycle fatigue of type 316Ti stainless steel in High temperature water, Mat. Sci. and Eng. A. 490 (2008) 16-25.
30. R. Ebara, Y. Yamada and A. Goto, Corrosion fatigue behaviour of 13Cr stainless steel and Ti-6Al-4V ultrasonic frequency, Fatigue ultrasonore TMS (1980).
31. T. Palin-Luc, R. Pérez-Mora, C. Bathias, G. Domínguez, P. C. Paris, J. Luis Aran, Fatigue crack initiation and growth on a steel in the very high cycle regime with sea water corrosion, Engng. Fract. Mech. 77(2010)1953-1962.
32. Y. Iwahashi, Z. Horita, M. Nemoto, T.G. Langdon, The process of grain refinement in equal-channel angular pressing, Acta Mater. 46 (1998) 3317–3331.
33. M. Shahzad, Influence of Extrusion Parameters on Microstructure Development and Mechanical Properties in Wrought Magnesium Alloys AZ80 and ZK60, Dr.-Ing. Thesis, TU Clausthal, 2007.
34. T. Wang, J. Yu, J., Dong, B, Surface nanocrystallization induced by shot peening and its effect on corrosion resistance of 1Cr18Ni9Ti stainless steel, Surf. Coat. Technol. 200(2006)4777.
35. A. Onizawa, M.A. Islam, Y. Tomota, Fatigue properties of smooth and as-shot peened N bearing austenitic stainless steel under tension-tension condition, ARPN J. Eng. Appl. Sci. 1(2006)12.
36. J. Lincks, BD. Boyan, CR. Blanchard, CH. Lohmann, Y. Liu, DL. Cochran, DD. Dean, Z. Schwartz, Response of MG63 osteoblast-like cells to titanium and titanium alloy is dependent on surface roughness and composition, Biomaterials 19(1998) 2219–32.

37. J. Havlikova, J. Strasky, M. Vandrovcova, P. Harcuba, M. Mhaede, M. Janecek, L. Bacakova, Innovative surface modification of Ti-6Al-4V alloy with a positive effect on osteoblast proliferation and fatigue performance, Mat. Sci. Eng. C. 39 (2014) 371-379.
38. M. Mhaede, F. Pastorek, B. Hadzima, Influence of shot peening on corrosion properties of biocompatible magnesium alloy AZ31 coated by dicalcium phosphate dehydrate (DCPD), Mat. Sci. Eng. C. 39 (2014) 330-335.
39. C. N. Elias, Y. Oshida, J.H.C. Lima, and C.A. Muller, Relationship between surface properties (roughness, wettability and morphology) of titanium and dental implant removal torque, J. Mech. Behav. Biomed. Mater. 1(2008)234.
40. D. D. Deligianni, N. Katsala, S. Ladas, D. Sotiropoulou, J. Amedee, and Y.F. Missirlis, Effect of surface roughness of the titanium alloy Ti-6Al-4V on human bone marrow cell response and on protein adsorption, Biomaterials 22 (2001) 1241.
41. M. Abdulstaar, M. Mhaede, L. Wagner, Pre-corrosion and surface treatments effects on the fatigue life of AA6082 T6, Advance Eng. Mat. 15(2013)1002-1006.
42. H. Luong, MR. Hill, The effects of laser peening and shot peening on high cycle fatigue in 7050–T7451 aluminium alloy, Mat. Sci. Eng. 527 (2010) 699–707.
43. A. A. Ahmed, M: Mhaede, M: Wollmann, L: Wagner, Effect of surface and bulk plastic deformations on the corrosion resistance and corrosion fatigue performance of AISI 316L. Surface & Coatings Technology 259 (2014) 448-455.
44. H. Lee, D. Kim, J. Jung, Y. Pyoun, K. Shin, Influence of peening on the corrosion properties of AISI 304 stainless steel, Corrosion Science 51: 12 (2009) 2826-2830.
45. Y. Hao, B.Deng, C. Zhong, Y. Jiang, J. Li, Effect of Surface Mechanical AttritionTreatment on Corrosion Behavior of 316 Stainless Steel, Journal of Iron and Steel Research, International 16:2 (2009) 68-72.
46. D. F. Williams, Corrosion of implant materials, Annual Review of Materials Science 6 (1976) 237.
47. J. W. Schultze, M.M. Lohrengel, Stability, reactivity and breakdown of passive films. Problems of recent and future research. Electrochimica Acta 45:15-16 (2000) 2499-2513.
48. P. Schmuki, From Bacon to barriers: A review on the passivity of metals and alloys, Journal of solid State electrochemistry 6 (2002) 145-164.

49. I. Milošev, M. Metikoš-Huković, HH. Strehblow, Passive film on orthopedic TiAlV alloy formed in physiological solution investigated by X-ray photoelectron spectroscopy, Biomaterials 21 (2000) 2103-2113.
50. I. Milošev, HH. Strehblow, The behavior of stainless steels in physiological solution containing complexing agent studied by X-ray photoelectron spectroscopy, Journal of Biomedical Materials Research 52 (2000) 404- 412.
51. I. Milošev, HH. Strehblow, The composition of the surface passive film formed on CoCrMo alloy in simulated physiological solution, Electrochimica Acta 48 (2003) 2767-2774.
52. Z. S. Smialowska, Pitting Corrosion of Metals, NACE, Houston (1986) TX 120-145.
53. R. M. Pidaparti, S. Jayanti, C. A. Sowers, and M. J. Palakal, Classification, Distribution and fatigue life of pitting corrosion for aircraft materials, Journal of Aircraft 39 (2002) 486-492.
54. O.O. Badran, O.M. Abuzeid, H.A. Al-Shoubaki, T. Al-Hadid and M. Al-Rimawi, Effect of shot peening on chloride stress corrosion cracking resistance of 304 stainless steel. Proceeding of the 1st International Industrial Engineering Conference IIEC (2001) 23-27.
55. T. Dorr, M. Hilpert, P. Beckmerhagan, A. Kiefer and L. Wagner, Influence of shot peening on fatigue performance of high-strength aluminum-and magnesium alloys, Proceedings of the ICSP-7 conference, Warsaw, Poland, 1999.
56. M. Obata and A. Sudo, Effect of shot peening on residual stress and stress corrosion cracking for cold worked austenitic stainless steel, Proceedings of the ICSP-5 conference, Oxford, UK, 1993.
57. J. Champaigne, Controlled shot peening, 2nd ed., The Shot Peener, Mishawaka, USA, 1989.
58. M.C. Sharma and A. Mubeen, Effect of shot size on peening intensity for local peening, Journal of Mechanical Working Technology 8 (1983) 155-160.
59. Suyitno, M. Mahardika, P. Dewo, B. Arifvianto, Study on surface properties and corrosion resistance of 316L stainless steel processed with steel slag ball blasting treatment, 9th International Conference on Fracture & Strength of Solids, 2013, Jeju, Korea.

60. Y. Oshida, R. Sachdeva, S. Miyazaki, J. Daly, Effects of shot-peening on surface contact angles of biomaterials, Journal of materials science: materials in medicine 4 (1993) 443-447.
61. B. Arifvianto, Suyitno, M. Mahardika, P. Dewo, P.T. Iswanto, U.A. Salim, Effect of surface mechanical attrition treatment (SMAT) on microhardness, surface roughness and wettability of AISI 316L, Materials Chemistry and Physics 125 (2011) 418–426.
62. B. Arifvianto, G.A. Pohan, Suyitno, M. Mahardika, Effect of slag ball blasting treatment on surface structure, roughness and wettability of 316LVM stainless steel, Procedia Engineering 50 (2012) 142–151.
63. E. G. Sharfrin, W. A. Zisman, Constitutive relations in the wetting of low energy surfaces and the theory of the retraction method of preparing monolayers, The Journal of Physical Chemistry 64:5 (1960) 519–524.
64. R. E. Baier, Surface behavior of biomaterials: the theta surface for biocompatibility, Journal of material science: Materials in medicine 17(2006) 1057.
65. S. N. Gorodzha, M. A. Surmeneva, R. A. Surmenev, M. V. Gribennikov, V. F. Pichugin, A. A. Sharonova, A. A. Pustovalova, O. Prymack, M. Epple, A. Wittmar, M. Ulbricht, K. V. Gogolinskii, and K. S. Kravchuk, Wettability of thin silicate-containing hydroxyapatite films formed by rf-magnetron sputtering, Russian Physics Journal, 56:10 (2014) 1163-1169.
66. F. Rupp, R.A. Gittens, L. Scheideler, A. Marmur, B.D. Boyan, Z. Schwartz, J. G. Gerstorfer, A review on the wettability of dental implant surfaces I: theoretical and experimental aspects, Acta Biomaterialia 10:7 (2014) 2894–2906.
67. A.T. Rad, M. S. Hashjin, N.A.A. Osman, S. Faghihi, Improved bio-physical performance of hydroxyapatite coatings obtained by electrophoretic deposition at dynamic voltage, Ceramics International 40:8 (2014) 12681–12691.
68. J. Dumbleton, M.T. Manley, Hydroxyapatite-coated prostheses in total hip and knee arthroplasty. J Bone Joint Surg A. 86 (2004) 2526.
69. M. F. Chen, X. J. Yang, R. X. Hu, Z. D. Cui, H. C. Man, Bioactive NiTi shape memory alloy used as bone bonding implants, Mat. Sci. Eng. C 24 (2004) 497.
70. H. Maleki-Ghaleh, J. Khalil-Allafi, V. Khalili, M. S. Shakeri, M. Javidi, Effect of hydroxyapatite coating fabricated by electrophoretic deposition method on corrosion behavior and nickel release of NiTi shape memory alloy, Mat. Corr. 64 (2013) 9999.

71. J. D. Bronzino, The Biomedical Engineering Handbook Boca Raton, USA: Boca Raton, FL: CRC Press, 2000.
72. Disabled-World Website, DePuy ASR Hip Replacement Recall: 12,000 Patients Will Need Revision Surgery, 2011 [online] Accessed (29/08/2011), Available: http://www.disabled-world.com/medical/recalls/asr-recall.php
73. S. Hierholzer, G. Hierholzer and K. H. Saucer, Increased Corrosion of Stainless Steel Implants in Infected Plated Fractures, Archives of Orthopaedic and Traumatic Surgery, 102:3(1984)198.
74. E. Chikarakara, Laser surface modification of biomedical alloys, Thesis submitted to the Faculty of Engineering and Computing, Dublin City University 2012.
75. D. Arpan, S. Sivaprasad, M. Ghosh, P.C. Chakrabortib and S. Tarafdera, Morphologies and characteristics of deformation induced martensite during tensile deformation of 304 LN stainless steel Mater. Sci. Eng. A 486(2008)283.
76. K. Nohara, Y. Ono and N. Ohashi, Composition and grain size dependencies of strain-induced martensitic transformation in metastable austenitic stainless steels, J. Iron Steel Inst. Jpn. 63 (1977) 212-222.
77. M. Kimura and Y. Miyata, Corrosion Resistance of High-Strength Modified 13% Cr Steel, Corrosion 55(1999)756.
78. N. J. E. Dowling, Y.-H. Kim, S.-K. Ahn and Y.-D. Lee, Effect of Alloying Elements and Residuals on Corrosion Resistance of Type 444 Stainless Steel, Corrosion, 55(1999)187.
79. H.S. Shatak and B. Raj, Corrosion of Austenitic Stainless Steel, Narosa Publishing Hose, London, 2002, 41.
80. M. P. Ryan, D. E. Williams, R. J. Chater, B. M. Hutton & D. S. McPhail, Why stainless steel corrodes, Nature 415(2002)770-774.
81. J. E. G. González and J. C. Mirza-Rosca, Study of the Corrosion Behaviour of Titanium and some of its Alloys for Biomedical and Dental Implant Applications, Journal of Electroanalytical Chemistry, 471:2(1999) 109-115.
82. B. Grosgogeat, L. Reclaru, M. Lissac and F. Dalard, Measurement and Evaluation of Galvanic Corrosion between titanium/Ti6Al4V Implants and Dental Alloys by Electrochemical Techniques and Auger Spectrometry, Biomaterials, 20:10(1999) 933-941.

83. B. F. Lowenberg, S. Lugowski, M. Chipman and J. E. Davies, ASTM-F86 Passivation Increases Trace Element Release from Ti6Al4V into Culture Medium, Journal of Materials Science: Materials in Medicine, 5:6-7(1994)467-472.
84. B. D. Ratner and B. D. Ratner, Biomaterials Science: An Introduction to Materials in Medicine, 2004. Available: http://isbndb.com/d/book/biomaterials_science.
85. E. Eisenbarth, D. Velten, M. Müller, R. Thull and J. Breme, Biocompatibility of β-Stabilizing Elements of Titanium Alloys, Biomaterials, 25:26(2004) 5705-5713,7-176.
86. Calphad website, Titanium-Aluminium Phase Diagram, 2012. Available: http://www.calphad.com/titanium-aluminum.html
87. B. Kasemo, Biocompatibility of Titanium Implants: Surface Science Aspects, The Journal of Prosthetic Dentistry, 49:6 (1983) 832-837.
88. G. Lutjering, J.C. Williams, Titanium, 2nd ed. (New York, NY: Springer, 2007).
89. M. Benedetti, J. Heidemann, J.O. Peters, G. Lutjering, Influence of sharp microstructural gradients on the fatigue crack growth resistance of α+β and near-α titanium alloys, Fatigue Fract. Eng. Mater. Struct. 28 (2005)909-922.
90. J. M. Donachie, Titanium—A Technical Guide, 2nd ed. (Materials Park, OH: ASM International, 2000).
91. S.-H. Lee, E. Takahashi, N. Nomura, and A. Chiba, Effect of Carbon Addition on Microstructure and Mechanical Properties of a Wrought Co–Cr–Mo Implant Alloy, Materials Transactions, 47(2006) 287-290.
92. G. Welsch, R. Boyer, Technical Note 1: Metallography and Microstructure, in Materials Properties Handbook: Titanium Alloys, eds. R. Boyer, G. Welsch, E.W. Collings (Materials Park, OH: ASM International, 1994) 1051-1060.
93. D. Julka, R. Vasishta and K. Gill, Distribution of Aluminum in Different Brain Regions and Body Organs of Rat, Biological Trace Element Research, 52:2(1996) 181-192.
94. J. G. Joshi, Aluminum, a Neurotoxin which Affects Diverse Metabolic Reactions, Biofactors 2:3(1990)163-9.
95. J. Scales, Black Staining Around Titanium Alloy Prostheses--an Orthopaedic Enigma, Journal of Bone and Joint Surgery, British Version, 73-B: 4(1991)534-536.
96. C. R. F. Azevedo, Failure Analysis of a Commercially Pure Titanium Plate for Osteosynthesis, Engineering Failure Analysis, 10:2(2003)153-164.

97. R.M Urban, J.J Jacobs, J.L Gilbert, J.O Galante, Migration of corrosion products from modular hip prostheses. Particle microanalysis and histopathological findings, J. Bone Joint Surg., 76A (1994)1345.
98. J. Been, J.S. Grauman, Titanium and Titanium Alloys, Uhlig's Corrosion Handbook, 2nd ed., ed. R.W. Revie (New York, NY: John Wiley & Sons, Inc., (2000)864.
99. S.Y. Yu, J.R. Scully, C.M. Vitus, Influence of niobium and zirconium alloying addition on the anodic dissolution behavior of activated titanium in HCl solutions, J. Electrochem. Soc. 148(2001) B68-78.
100. T. Fukuzuka, K. Shermogori, H. Satoh, F. Kamikubo, in: H. Kumura, O. Izumim (Eds.), Titanium '80 Science and Technology, 4th International conference on Titanium, Japan, Metallurgical Society of AMIE, (1981) 2685–2693.
101. L Dull, L Raymomd J. Electrochem. Soc., 116 (1969), p. 332.
102. V.S Raja, R.D Angal, M Suresh, Effect of Widmanstatten structure on protection potential of Ti-6Al-2Sn-4Zr-2Mo (0.1Si) alloy in 1 M NaBr solution, Corrosion, 49 (1993) 2.
103. K. Wan, L. Gustavson, J. Dumbleton, in: Beta Titanium in 1990's, The Minerals and Materials Society, Warrandale, USA (1993) 49–69.
104. S.Y Yu, J.R Scully, Corrosion and Passivity of Ti-13% Nb-13% Zr in Comparison to Other Biomedical Implant Alloys, Corrosion 53 (1997) 965.
105. S.Y Yu, C.W Brodrick, M.P Ryan, J.R Scully, Effects of Nb and Zr Alloying Additions on the Activation Behavior of Ti in Hydrochloric Acid, J. Electrochem. Soc. 146 (1999)4429.
106. R. Gadow, A. Killinger, N. Stiegler, Hydroxyapatite coatings for biomedical applications deposited by different thermal spray techniques, Surface Coatings and Technology 205 (2010) 1157-1164.
107. A, Drechsler, J. Kiese, L Wagner, Effects of shot peening and roller-burnishing on fatigue performance various titanium alloys, In: Proc. of 7th International Conference on Shot Peening(ICSP7), A. Nakonieczny (Ed.), Warsaw (1999) 145- 152.
108. R. K. Nalla, I. Altenberger, U. Noster, G. Y. Liu, B. Scholtes, R. o. Ritchie, On the influence of mechanical surface treatments- deep rolling and laser chock peening- on the fatigue behavior of Ti-6Al-4V at ambient and elevated temperatures. Mater. Sci. Eng. A 355(2003) 216-230.

109. P. Hutmann, The application of mechanical surface treatments in the passenger car industry. Shot peening, L. Wagner (Ed.), Willey-VCH- Verlag, Weinheim, (2003)4-12.
110. B. Kiefer, Shot peening, special application and procedure, in ICSP-3 (Garmisch-Partenkirchen, Germany) (1987)157–162.
111. S. Biker, Shot peening: a dynamic application and its future, MFN-Metal Finishing News 2006.
112. D. Kirk, shot peening. Aircraft Engineering and Aerospace Technology, 71 (1999) 349-361.
113. N. R. Babu, S.Manwatkar, K. P. Rao, T. S. Kumar, Bioactive coatings on 316L stainless steel implants, Trends in Biomaterials and Artificial Organs 17(2004) 43-47.
114. D. Liu, K. Savino, M. Z. Yates, Coating of hydroxyapatite films on metal substrates by seeded hydrothermal deposition, Surface & Coatings Technology, 205 (2011) 3975-3986.
115. C. Kwok, P.Wong, F.Cheng, H. Man, Characterization and corrosion behavior of hydroxyapatite coatings on Ti6-Al-4V fabricated by electrophoretic deposition, Applied Surface Science 255 (2009) 6736-6744.
116. E. S. Bogya, Z. Károly, R. Barabás, Atmospheric plasma sprayed silica–hydroxyapatite coatings on magnesium alloy substrates, Ceramics International, 41:4 (2015) 6005–6012.
117. M. P. Masouleh, H. Asgharzadeh, Optimization of sol-gel technique for coating of metallic substrates by hydroxyapatite using the Taguchi method, Materials Science-Poland, 31:3 (2013) 424-433.
118. S. Erakovića, A. Jankovića, C. Ristoscub, L. Dutab, N. Serbanb, A. Visanb, I.N. Mihailescub, G.E. Stanc, M. Socolc, O. Iordached, I. Dumitrescud, C.R. Luculescub, D. Janaćkovića, V. M.Stankovića, Antifungal activity of Ag:hydroxyapatite thin films synthesized by pulsed laser deposition on Ti and Ti modified by TiO2 nanotubes substrates, Applied Surface Science 293 (2014) 37–45.
119. J. Ma, H. Wong, L. Kong, K. Peng, Biomimetic processing of nanocrystallite bioactive apatite coating on titanium, Nanotechnology 14 (2003) 1239-1324.
120. B. Hadzima, M. Mhaede, F. Pastorek, Electrochemical characteristics of calcium-phosphatized AZ31 magnesium alloy in 0.9 % NaCl solution, Journal of Materials Science: Materials in Medicine, 25 (2014) 1227-1237.

121. M. Mhaede, F. Pastorek, B. Hadzima, Influence of shot peening on corrosion properties of biocompatible magnesium alloy AZ31 coated by dicalcium phosphate dihydrate (DCPD), Materials Science and Engineering: C 39 (2014) 330-335.

122. A. V. Zavgorodniy, O. Borrero-López, M. Hoffman, R. Z. LeGeros, R. Rohanizadeh, Characterization of the chemically deposited hydroxyapatite coating on a titanium substrate, Journal of Materials Science: Materials in Medicine 22 (2010) 1-9.

123. J. Weng, X. Liu, X. Zhang and Z. Ma, Amorphous phase and morphological structure of hydroxyapatite plasma coatings, Biomaterials 14 (1993) 225-228.

124. C. W. Yang, T. M. Lee, T. S. Lui and E. Chang, A Comparison of the microstructural feature and bonding strength of plasma-sprayed hydroxyapatite coatings with hydrothermal and vacuum post-heat treatment, Materials transactions 46 (2005) 709-715.

125. A. V. Zavgorodniy, O. Borrero-López, M. Hoffman, R. Z. LeGeros, R. Rohanizadeh, Mechanical stability of two-step chemically deposited hydroxyapatite coating on Ti substrate: effects of various surface pretreatments, Journal of Biomedical Materials Research B 99 (2011) 58-69.

126. R. Schnettler, PD. Knöß, C. Heiss, JP. Stahl, C. Meyer, O. Kilian, S. Wenisch, V. Alt, Enhancement of bone formation in hydroxyapatite implants by rhBMP-2 coating, Journal of Biomedical Materials Research 90B (2009) 75-81.

127. D. Sj, C. Ju, L. Jh, Immersion behavior of RF magnetron-assisted sputtered hydroxyapatite/titanium coatings in simulated body fluid, Journal of Biomedical Materials Research 47 (1999) 551-563.

128. Y. C. Tsui, C. Doyle, T. W. Clyne, Plasma-sprayed hydroxyapatite coatings on titanium substrates. Part 1. Mechanical properties and residual stress levels, Biomaterials 19 (1998) 2015-2029.

129. S. Wang, W. R. Lacefield, J. E. Lemons, Interfacial shear strength and histology of plasma sprayed and sintered hydroxyapatite implants in vivo, Biomaterials 17 (1996) 1965-1970.

130. C. T. Kwok, P. K. Wong, F. T. Cheng, H. C. Man, Characterization and corrosion behavior of hydroxyapatite coatings on Ti6Al4V fabricated by electrophoretic deposition, Applied Surface Science 255 (2009) 6736-6744.

131. M. We, A. J. Ruys, M. V. Swain, B. K. Milthorpe, C. C. Sorrell, Hydroxyapatite-coated metals: Interfacial reactions during sintering, Journal of Materials Science: Materials in Medicine 16 (2005) 101-106.
132. C. C. Chen, S. J. Ding, Effect of heat treatment on characteristics of plasma sprayed hydroxyapatite coatings, Materials Transactions 47 (2006) 935-940.
133. C. W. Yang, T. S. Lui, Effect of hydrothermal self-healing and intermediate strengthening layers on adhesion reinforcement of plasma-sprayed hydroxyapatite coatings, Advanced plasma spray applications, InTech, 2012.
134. M. Wei, A. J. Ruys, B. K. Milthorpe, C. C. Sorrell, Precipitation of hydroxyapatite nano-particle: Effects of precipitation method on electrophoretic deposition, Journal of Materials Science: Materials in Medicine 16 (2005) 319-324.
135. K. Anselme, M. Bigerelle, Statistical Demonstration of the Relative Effect of Surface Chemistry and Roughness on Human Osteoblast Short-term Adhesion. J. Mater. Sci. Mater. Med. 17 (2006) 471−479.
136. B. C. Ward, T. J. Webster, The Effect of Nanotopography on Calcium and Phosphorus Deposition on Metallic Materials In Vitro. Biomaterials 27 (2006) 3064−3074.
137. K. Cai, J. Bossert, Jandt, K. D. Jandt, Does the Nanometre Scale Topography of Titanium Influence Protein Adsorption and Cell Proliferation? Colloids Surf., B 49 (2006) 136−144.
138. T. J. Webster, C. Ergun, R. H. Doremus, R. W. Siegel, R. Bizios, Specific Proteins Mediate Enhanced Osteoblast Adhesion on Nanophase Ceramics. J. Biomed. Mater. Res. 51 (2000) 475−483.
139. H. Gleiter, Materials with ultrafine microstructures: Retrospectives and perspectives, Nanostructured Materials 1 (1992) 1-19.
140. U. Erb, Electrodeposited nanocrystals: Synthesis, properties and industrial applications, Nanostructured Materials, 6 (1995) 533-538.
141. W. Chang, G. Skandan, S.C. Danforth, M. Rose, A.G. Balogh, H. Hahn, B. Kear, Nanostructured ceramics synthesized by chemical vapor condensation, Nanostructured Materials, 6 (1995) 321-324.
142. C.C. Koch, Y.S. Cho, Nanocrystals by high energy ball milling, Nanostructured Materials, 1 (1992) 207-212.

143. A. A. Ahmed, M. Mhaede, M. Wollmann, L. WagnerInstitute, Effect of micro shot peening on the mechanical properties and corrosion behavior of two microstructure Ti–6Al–4V alloy, Applied Surface Science, 363 (2016) 50–58.

144. S. Giribaskar, P. R. Gouthama, Ultra-Fine Grained Al-SiC Metal Matrix Composite by Rotary Swaging Process, Materials Science Forum, 702-703 (2012) 320-323.

145. S. J. Oh, S.B. Kang, Analysis of the billet deformation during equal channel angular pressing, Materials Science and Engineering: A 343 (2003) 107-115.

146. M. Kawasaki, T. G. Langdon, The significance of strain reversals during processing by high-pressure torsion, Materials Science and Engineering: A 498 (2008) 341-348.

147. Y. J. Kwon, I. Shigematsu, N. Saito, Mechanical properties of fine-grained aluminum alloy produced by friction stir process, Scripta Materialia, 49 (2003) 785-789.

148. M. Mhaede, A. A. Ahmed, M. Wollmann , L. Wagner, Evaluating the effects of hydroxyapatite coating on the corrosion behavior of severely deformed 316Ti SS for surgical implants, Materials Science and Engineering C 50 (2015) 24–30.

149. M. K. Chung, Y. S. Choi, J. G. Kim, Y.M. Kim, J. C. Lee, Effect of the number of ECAP pass time on the electrochemical properties of 1050 Al alloys, Materials Science and Engineering: A 366 (2004) 282-291.

150. WM. Al-Omari, CA. Mitchell, JL. Cunningham, Surface roughness and wettability of enamel and dentine surfaces prepared with different dental burs. J Oral Rehabil 28 (2001)645-650.

151. Image Taken from Torrington-Machinery Website./www.torrington-machinery.com /images/pic_rotary_swaging1.gifS (accessed 26.9.2012).

152. M. Lawerenz, Shot Peening Ductile Iron, Modern Casting. (1990) 51-53.

153. W. D. Callister, Materials Science and Engineering: An Introduction 2000, Available: http://isbndb.com/d/book/materials_science_and_engineering.

154. ASTM G5-94, Standard reference test method for making potentiostatic and potentiodynamic anodic polarization measurements, ASTM, 2004, Philadelphia.

155. T. -H. Lee, E. Shin, C. -S. Oh, H. -Y. Ha, S. -J. Kim, Correlation between stacking fault energy and deformation microstructure in high-interstitial-alloyed austenitic steels, Acta Materialia, 58 (2010) 3173-3186.

156. J. Talonen, H. Hänninen, Formation of shear bands and strain-induced martensite during plastic deformation of metastable austenitic stainless steels, Acta Materialia, 55 (2007) 6108-6118.
157. D. Kirk and N.J. Payne, Transformations Induced in Austenitic Stainless Steels by Shot 16 Peening, The 7th International conference on shot peening, 1999.
158. W. Pitschkea, H. Hermanna, N. Matterna, The influence of surface roughness on diffracted X-ray intensities in Bragg–Brentano geometry and its effect on the structure determination by means of Rietveld analysis, Mat. Characterization (1993) 74-83.
159. F. J. Humphreys, M. Hatherly, Recrystallization and Related Annealing Phenomena, 24 Elsevier Science Ltd (1995) 17.
160. R. K. Pandey M. N. Deshmukh, Shot peening and its impact on fatigue life of engineering components, International conference on shot peening and blast cleaning (2001) 1-20.
161. S. M. H. Gangaraj, A. Moridi, M. Guagliano, From conventional to severe shot peening to generate nanostructured surface layer: A numerical study, Materials Science and 30 Engineering 63 (2014) 012038.
162. P. Peyre, X. Scherpereel, L. Berthe, C. Carboni, R. Fabbro, G. Be´ranger, C. Lemaitre, Surface modifications induced in 316L steel by laser peening and shot peening, Materials Science and Engineering A280 (2000) 294–302.
163. B. N. Mordyuk, G. I. Prokopenko, Ultrasonic impact peening for the surface properties management, Journal of Sound and Vibration, 308 (2007) 855.
164. T. Roland, D. Retraint, K. Lu, J. Lu, Fatigue life improvement through surface nanostructuring of stainless steel by means of surface mechanical attrition treatment, Scripta Materialia 54 (2006) 1949.
165. G. Ratti, U. Mariani, M. Giglio, M. Guagliano, Effect of Residual Stresses from Shot Peening On Fatigue Strength And Threshold To Crack Propagation Of Al 7475 Alloy Components,12th ICAF (2009) 859-870.
166. M.A.S Torres, H.J.C Voorwald, An evaluation of shot peening, residual stress and stress relaxation on the fatigue life of AISI 4340 steel, International Journal of Fatigue, 24:8 (2002) 877–886.
167. R. D., Skinner, Formability Topics—Metallic Materials ASTM STP 647, American society for testing and materials, Stress –peen straightening of complex machined aircraft parts, (1978) 100-121.

168. H.Y. Miao, S. Larose, C. Perron, M. Lévesque, An analytical approach to relate shot peening parameters to Almen intensity, Surface and Coatings Technology 205:7 (2010) 20 2055-2066.

169. L. Wagner, M. Mhaede, M. Wollmann, I. Altenberger, Surface layer properties and fatigue behavior in Al 7075-T73 and Ti-6Al-4V Comparing results after laser peening; shot peening and ball-burnishing, International Journal of Structural integrity 2: 2(2011) 24 185-199.

170. H. Barzoukas, and J. Jauffret, Peening with Ceramic Shot, ICSP-4 (1990) 47-56.

171. M. J. Filiaggi, R. M. Pilliar, N. A. Coombs, Post-plasma-spraying heat treatment of the HA coating/Ti-6A1-4V implant system, Journal of Biomedical Materials Research 27 (1993) 191-8.

172. C. Kaya, Electrophoretic deposition of carbon nano tube-reinforced hydroxyapatite bioactive layers on Ti–6Al–4V alloys for biomedical applications, Ceramics International 34 (2008) 1843-1847.

173. J. Ma, C. H. Liang, L. B. Kong, C. Wang, Colloidal characterization and electrophoretic deposition of hydroxyapatite on titanium substrate, Journal of Materials Science: Materials in Medicine 14 (2003) 797-801.

174. M. Wei, A. J. Ruys, B. K. Milthorpe, C. C. Sorrell, Precipitation of hydroxyapatite nano-particle: Effects of precipitation method on electrophoretic deposition, Journal of Materials Science: Materials in Medicine 16 (2005) 319-324.

175. P. Sarkar, P. S. Nicholson, Electrophoretic Deposition (EPD): Mechanisms, Kinetics, and Application to Ceramics, American Ceramic Society 79 (1996) 1987-2002.

176. Y. P. Lu, Y. M. Chen, S. T. Li, J. H. Wang, Surface Nanocrystallization of Hydroxyapatite Coating, Acta Biomaterialia, 4 (2008) 1865-1872.

177. T. Kunzler, T. Drobek, M. Schuler, N. D. Spencer, Systematic Study of osteoblast and fibroblast response to roughness by means of surface morphology gradients, Biomaterials 28 (2007) 2175-82.

178. G. Zhao, A. L. Raines, M. Wieland, Z. Schwartz, B. D Boyan, Requirement for both micron- and submicron scale structure for synergistic responses of osteoblasts to substrate surface energy and topography, Biomaterials 28 (2007) 2821-9.

179. D. O. Costa, P. D. H. Prowse, T. Chrones, S. M. Sims, D. W. Hamilton, A. S. Rizkalla, S. J. Dixon, The differential regulation of osteoblast and osteoclast activity by surface topography of hydroxyapatite coatings, Biomaterials 34 (2013) 7215 -7226.

180. H. Ji, P. M. Marquis, Effect of heat treatment on the microstructure of plasma-sprayed hydroxyapatite coating, Biomaterials 14 (1993) 64-8.
181. I. Oh, N. Nomura, A. Chiba, Y. Murayama, N. Masahashi, B. Lee, S. Hanada, Microstructures and bond strengths of plasma-sprayed hydroxyapatite coatings on porous titanium substrates, Journal of Materials Sciences: Materials in Medicine, 16 (2005) 635-640.
182. F. Chen, L. W. Lin, C. J. Lin, W. W. Lu, Electrophoretic deposition of hydroxyapatite nano coating on etched titanium surface, Key Engineering Materials 288-289 (2005) 183-186.
183. M. Goudarzi, F. Batmanghelich, A. Afshar, A. Dolati, G. Mortazavi, Development of electrophoretically deposited hydroxyapatite coatings on anodized nanotubular TiO2 structures: Corrosion and sintering temperature, Applied Surface Science 301 (2014) 250–257.
184. L. Yan, Y. Leng, L. Weng, Characterization of chemical inhomogeneity in plasma-sprayed hydroxyapatite coatings, Biomaterials 24 (2003) 2585–92.
185. Y. C. Yang, B. Y. Chou, Bonding strength investigation of plasma-sprayed HA coatings on alumina substrate with porcelain intermediate layer, Materials Chemistry and Physics 104 (2007) 312-319.
186. Z. Zhang, M. F. Dunn, T. D. Xiao, A. P. Tomsia, E. Saiz, Nanostructured hydroxyapatite coatings for improved adhesion and corrosion resistance for medical implants, Nanotech & Biotech Convergence – 2002, Stamford 2002; 291-296.
187. B. Aksakal, M. Gavgali, B. Dikici, The Effect of coating thickness on corrosion resistance of hydroxyapatite coated Ti6Al4V and 316L SS implants, Journal of Materials Engineering and Performance 19 (2010) 894-899.
188. M. S. Ali, S. Song and P. Xiao, Evaluation of degradation of thermal barrier coatings using impedance spectroscopy, European Ceramic Society 22 (2002) 101-107.
189. C. N. Elias, Y. Oshida, J. H. Lima, C. A. Muller, Relationship between surface properties (roughness, wettability and morphology) of titanium and dental implant removal torque, Journal of the Mechanical Behavior of Biomedical Materials 1:3 (2008) 234–242.
190. Z. Piao1, J. Qiu, Y. Wu, S. Park, W. He, A. Timur, S. Ryu, H. Kim, and Y. Hwang, Effects of the Nano-Tubular Anodic TiO2 Buffer Layer on Bioactive Hydroxyapatite Coating, Journal of Nanoscience and Nanotechnology 11(2011) 286–290.

191. N. Eustathopoulos, N. Sobczak, A. Passerone, K. Nogi, Measurements of contact angle and work of adhesion at high temperature, Journal of Materials Science 40 (2005) 2271– 2280.

192. R.E. Baier, E.G. Shafrin, W.A. Zisman, Adhesion: mechanisms that assist or impede it, Science. 162 (1968) 1360–1368.

193. C. J. Wilson, R. E. Clegg, D. I. Leavensley, M.J. Pearcy, Mediation of biomaterial-cell interactions by adsorbed proteins: a review, Tissue Eng. 11 (2005) 1.

194. S. Bagherifard, R. Ghelichi, A. Khademhosseini, M. Guagliano, Cell Response to Nanocrystallized Metallic Substrates Obtained through Severe Plastic Deformation, Applied Materials & Interfaces 6:11 (2014) 7963–7985.

195. Y. Wang, L. Lu, Y. Zheng, X. Chen, Improvement in hydrophilicity of PHBV films by plasma treatment, Journal of Biomedical Materials Research A 76:3 (2006) 589–595.

196. Y. Arima, H. Iwata, Effect of wettability and surface functional groups on protein adsorption and cell adhesion using well-defined mixed self-assembled monolayers, Biomaterials 28 (2007) 3074-3082.

197. L. Peguet, B. Malki, B. Baroux, Influence of cold working on the pitting corrosion resistance of stainless steels, Corrosion Science 49 (2007) 1933-1948.

198. A. Barbucci, G. Cerisola, P. L. Cabotb, Effect of Cold-Working in the Passive Behavior of 304 Stainless Steel in Sulfate Media, J Electrochemical Society 149 (2002) B534- B542.

199. E. Symniotis, Galvanic effects on the active dissolution of duplex stainless steels, Corrosion 46 (1990) 2-11.

200. R. Ke, R. Alkire, Initiation of corrosion pits at inclusions on 304 stainless steel, J Electrochemical Society 142 (1995) 4056-4062.

201. S. Sonmez, B. Aksakal, B. Dikici, Influence of hydroxyapatite coating thickness and powder particle size on corrosion performance of MA8M magnesium alloy, J Alloys and Compounds, 596 (2014) 125–131.

202. C. P. A. T. Klein, J. G. C. Wolke, J. M. A. de Blieck-Hogervorst, K. de Groot, Features of calcium phosphate plasma-sprayed coatings: An in vitro study, J Biomedical Materials Research A, 28 (1994) 961-967.

203. L. Chou, B. Marek, W. R. Wagner, Effects of hydroxylapatite coating crystallinity on biosolubility, cell attachment efficiency and proliferation in vitro, Biomaterials 20 (1999) 977-985.
204. G. L. Darimont, R. Cloots, E. Heinen, L. Seidel, R. Legrand, In vivo behavior of hydroxyapatite coatings on titanium implants: a quantitative study in the rabbit, Biomaterials, 23 (2002) 2569-2575.
205. W. Xue, S. Tao, X. Liu, X. Zheng, C. Ding, In vivo evaluation of plasma sprayed hydroxyapatite coatings having different crystallinity, Biomaterials 25 (2004) 415-421.
206. W. Xue, X. Liu, X. Zheng,C. Ding, Effect of hydroxyapatite coating crystallinity on dissolution and osseointegration in vivo, J Biomedical Materials Research A, 74 (2005) 553-561.
207. D. Gopi J. Indira L. Kavitha J. M. F. Ferreira, Hydroxyapatite coating on selectively passivated and sensitively polymer-protected surgical grade stainless steel, J Applied Electrochemistry 43 (2013) 331-345.
208. XY. Wang, DY. Li, Mechanical and electrochemical behavior of nanocrystalline surface of 304 stainless steel, Electrochimica Acta 47 (2002) 3939-3947.
209. A. Berzins, R. T. Lowson and K. J. Mirams, Aluminium corrosion studies. III. Chloride adsorption isotherms on corroding aluminium, Journal of Chemistry 30 (1977) 1891- 1903.
210. G. C. Wood, J. A. Richardson, M. F. Abd Rabbo, L. M. Mapa, W. H. Sutton, Passivity of metals, The Electrochemical Society Pennington NJ (1978) 973.
211. J. Moran, Metals handbook, Metals Park, OH, ASM International 13A (2003) 275.
212. Z. S. Smialowska, Pitting corrosion of aluminum, Corrosion Science 41 (1999) 1743–1767.
213. J. Congleton, W. Zheng, and H. Hua, Stress Corrosion Cracking of Annealed Type 316 Stainless Steel in High-Temperature Water, Corrosion, 46 (1990) 621-627.
214. R. Ke, R. Alkire, Initiation of Corrosion Pits at Inclusions on 304 Stainless Steel, Journal of the Electrochemical Society 142 (1995) 4056.
215. C. Aparicio, F.J. Gil, C. Fonseca, M. Barbosa, and J.A. Planell, Corrosion behavior of commercially pure titanium shot blasted with different materials and sizes of shot particles for dental implant applications, Biomaterials, 24(2003) 263.

216. B. Wei, J.C. Tokash, F. Zhang, Y. Kim, B.E. Logan, Electrochemical analysis of separators used in single-chamber, air–cathode microbial fuel cells. Electrochim Acta. 89 (2013) 45–51.
217. S. Ningshen, U. K. Mudali, G. Amarendra, B. Raj, Corrosion assessment of nitric acid grade austenitic stainless steels, Corrosion Science 51 (2009) 322.
218. S.B. Mahagaonkar, P.K. Brahmankar, C.Y. Seemikeri, Effect on fatigue performance of shot peened components: An analysis using DOE technique, Int. J. Fatigue 31 (2009) 693.
219. MA. Abdulstaar, EA. El-Danaf, NS. Waluyo, L. Wagner, Severe plastic deformation of commercial purity aluminum by rotary swaging: Microstructure evolution and mechanical properties, Mat. Sci. Eng. A 565 (2013) 351.
220. A.K. Shukla, R. Balasubramaniam, S. Bhargava, Properties of passive film formed on CP titanium, Ti–6Al–4V and Ti–13.4Al–29Nb alloys in simulated human body conditions, Intermetallics 13 (2005) 631-637.
221. G. Liu, J. Lu, K. Lu, Surface Nanocrystallization of 316L Stainless Steel Induced by Ultrasonic Shot Peening, Materials Science and Engineering: A 286 (2000) 91–95.
222. T. V. Rajan, C. P. Sharma, A. Sharma, Heat Treatment: Principles and Techniques, second edition, (1994) 305-306.
223. R. Reda, A. A. Nofal, A. A. Hussein, Effect of Quenching Temperature on the Mechanical Properties of Cast Ti-6Al-4V Alloy, Journal of Metallurgical Engineering (ME) 2:1 (2013) 49-54.
224. G. Lütjering, Influence of processing on microstructure and mechanical properties of (α+β) titanium alloys, Materials Science and Engineering: A, 243 (1998) 32–45.
225. R. Filip, K. Kubiak, W. Ziaja, J. Sieniawski, The effect of microstructure on the mechanical properties of two-phase titanium alloys, Journal of Materials Processing Technology 133 (2003)84–89.
226. K. Iida and, K. Tosha, Fatigue strength of work softening layer produced by shot peening, in ICSP-3 (Garmisch-Partenkirchen, Germany) (1987) 611–618.
227. F. Burgahn, O. Vohringer and E. Macherauch, Microstructural investigations of the shot peened steel 42 CrMo4 in different heat treatment conditions by the aid of a X-ray profile analysis, in ICSP-4 (Tokyo, Japan) (1990) 199–208.
228. M. Xinling, W. Wei and Y. Wei, Simulation for surface self-nanocrystallization under shot peening, Acta Mechanica Sinica 19 (2003) 172–180.

229. V. Schulze and A. N. Lari, Proceedings of international conference on shot peening-9, (Marne la Valle, France), 2005.
230. O. Higounenc, Correlation of shot peening parameters to surface characteristic, ICSP-9, Paris, France, 28-35, 2005.
231. M. Lundberg, R. L. Peng, M. Ahmad, T. Vuoristo, D. Bäckström, S. Johansson, Influence of Shot Peening Parameters on Residual Stresses in Flake and Vermicular Cast Irons, Materials science forum 768-769 (2014) 534-541.
232. J. M. Donachie, Titanium—A Technical Guide, 2nd ed. (Materials Park, OH: ASM International, 2000).
233. M. Levy, G.N. Sklover, Anodic Polarization of Titanium and Titanium Alloys in Hydrochloric Acid, Journal of the Electrochemical Society 116 (1969) 323- 328.
234. A. Balakrishnan, B.C. Lee, T.N. Kim, and B.B. Panigrahi, Corrosion Behavior of Ultra Fine Grained Titanium in Simulated Body Fluid for Implant Application, Trends Biomater. Artif. Organs 22:1 (2008) 194–208.
235. Z.J. Zheng, Y. Gao, Y. Gui, and M. Zhu, Corrosion Behaviour of Nanocrystalline 304 Stainless Steel Prepared by Equal Channel Angular Pressing, Corrosion Science 54 (2012) 60–67.

Curriculum Vitae

Personal Data:

Name: Aymen A. Ahmed

Date of Birth: 02.01.1976 in Mosul/ Iraq

Sex: Male

Nationality: Iraqi

Marital Status: Married

Adresse: Berliner Str. 59, 38678 Clausthal-Zellerfeld, Germany

E Mail: ayman.jabar@yahoo.com
aymen.ahmed@tu-clausthal.de

Tel: 0049/ 17655490036

Academic Qualifications:

1994- 1998 B.Sc. in Physics / College of science / University of Mosul.

2001- 2004 M.Sc. in Materials Science / College of science / University of Mosul.

Research areas:

- Protect coating systems.
- Behavior of medical implant materials under quasi physiological ambient conditions.
- Effects of corrosive environments.
- Fatigue behavior in multistage or multiaxial loading.

Research experiences:

- **2005- 2012:** Researcher in the department of Physics, College of Science, Mosul University, Mosul/Iraq.
- **Since 2013:** Research fellowship sponsored by Iraq scholarship counsel at institute of materials science and engineering, Clausthal University of Technology, Clausthal-Zellerfeld, Germany.

Reviewer in the following Journals:

- Journal of Applied Surface Science.
- Journal of Surface and Coating Technology.

- Journal of Alloys and Compounds.
- Journal of Crystals

<u>Publications:</u>

2015

- **Aymen A. Ahmed**, Mansour Mhaede, Manfred Wollmann, Lothar Wagner, Effect of micro shot peening on the mechanical properties and corrosion behavior of two microstructureTi-6Al-4 V alloy, Applied Surface Science, 2015 pp. 50-58.
- **Aymen A. Ahmed**, Mansour Mhaede, M Basha, Manfred Wollmann, LotharWagner, The effect of shot peening parameters and hydroxyapatite coating on surface properties and corrosion behavior of medical grade AISI 316Lstainless steel, Surface & Coatings Technology V. 280, 2015, pp 347–358.
- **Aymen A. Ahmed**, M. Mhaede, M. Wollmann, L. Wagner, Characteristics of sintered HA coating deposited by chemical method on AISI 316L substrate, Materials and Design, V. 76, 2015, P. 9–17.
- Mansour Mhaede, **Aymen A. Ahmed**, Manfred Wollmann, Lothar Wagner, Evaluating the effects of hydroxyapatite coating on the corrosion behavior of severely deformed 316Ti SS for surgical implants, Materials Science and Engineering C, V. 50, 2015 P. 24–30.
- Mahmoud Basha, Urlich Raab, **Aymen A. Ahmed**, Mansour Mhaede, Manfred Wollmann, Lothar Wagner, Effect of Shot Peening and Roller-burnishing on the Fatigue Performance of cp-Ti Friction-welded Joints, Ti-2015: The 13th World Conference on Titanium.

2014

- **Aymen A.Ahmed**, M. Mhaede, M. Wollmann, L. Wagner, Effect of surface and bulk plastic deformations on the corrosion resistance and corrosion fatigue performance of AISI 316L, Surface and Coatings Technology, V. 259, Part C, 2014, P. 448–455.
- **Aymen A. Ahmed**, M. Mhaede, M. Wollmann, L. Wagner, Shot peening effects on corrosion behavior of Hydroxyapatite coated AISI 316L Stainless steel alloy for medical implant application, Shot Peening and Other Mechanical Surface Treatments - Science and Applications, Eigenverlag (L. Wagner, ed.) 2014.

Aymen A. Ahmed

10.05.2017